



The University of
Nottingham

UNITED KINGDOM • CHINA • MALAYSIA

Investigation on thermal and kinetic dynamics of droplets

Li Wang, BEng.

Thesis submitted to the University of Nottingham for the degree of Doctor of Philosophy

March 2023

Abstract

In recent years, there has been a surge of interest in studying the dynamics of droplets due to their broad range of applications. However, despite their prevalence in nature, accurately predicting and controlling the various behaviours of droplets, such as evaporation and impingement, remains challenging due to the intricate underlying mechanisms involved. This thesis aims to address these challenges by consolidating existing literature and conducting a comprehensive investigation into the thermal and kinetic dynamics of droplets.

Both numerical and experimental approaches were employed in this research. The numerical work utilised a multi-component multiphase pseudopotential Lattice Boltzmann model to simulate droplet dynamics. The focus was on studying the Marangoni effect by simulating droplet evaporation under localised heating. By introducing a non-uniform temperature distribution within the droplet, the temperature-induced Marangoni flow was generated, and its impact on the flow field and temperature distribution was analysed. Additionally, under certain conditions, the emergence of an asymmetrical droplet shape was observed, resulting in the droplet sliding on smooth surfaces. Another numerical simulation was conducted to investigate droplet impingement on a conical structure. To achieve an equilibrium wetting state on the inclined surface, a modified boundary condition scheme was proposed. The influence of gravity, surface wettability, and surface temperature on the impingement process was studied, and various outcomes were observed. Furthermore, the individual contributions of each factor were analysed.

To complement the numerical investigations, an experimental study was conducted to further analyse droplet impingement on conical obstacles. High-speed cameras were employed to capture the impingement process, allowing for exploring factors not covered in the numerical research, such as cone angles and surface roughness. This study significantly

enhanced the understanding of the thermal and kinetic dynamics of droplets and expanded the potential applications of droplets by leveraging their unique characteristics.

List of publications during PhD study

- Wang, L., Liu, Z., Wang, X. et al. Investigation on the droplet evaporation process on local heated substrates with different wettability. *Heat Mass Transfer* (2020). <https://doi.org/10.1007/s00231-020-03005-6>
- Wang, X., Liu, Z., Wang, L. et al. Investigation of Droplet Evaporation on Copper Substrate with Different Roughness. *J Bionic Eng* 17, 835–842 (2020). <https://doi.org/10.1007/s42235-020-0069-5>
- Li Wang, Xin Wang, Yuying Yan, An investigation of droplet impingement on a conical obstacle, *Thermal Science and Engineering Progress*, Volume 37, 2023, 101586, ISSN 2451-9049, <https://doi.org/10.1016/j.tsep.2022.101586>
- Shuai Zhang, Daili Feng, Lei Shi, Li Wang, Yingai Jin, Limei Tian, Ziyuan Li, Guoyong Wang, Lei Zhao, Yuying Yan, A review of phase change heat transfer in shape-stabilized phase change materials (ss-PCMs) based on porous supports for thermal energy storage, *Renewable and Sustainable Energy Reviews*, Volume 135, 2021, 110127, ISSN 1364-0321, <https://doi.org/10.1016/j.rser.2020.110127>

Acknowledgement

First and foremost, I would like to extend my utmost appreciation to my supervisor, Prof. Yuying Yan, for his unwavering support and patient guidance throughout my entire PhD study. From the inception of my research to the completion of my work, his invaluable assistance has been instrumental in my achievements.

Secondly, I am deeply grateful to my colleagues from the School of Architect and Built Environment, who have provided immense assistance during the course of my study. Dr. Wei Gong offered numerous constructive suggestions in establishing my numerical model, while Dr. Xin Wang provided invaluable collaboration in the experimental research. I would like to express my thanks to Mr. Tony Gospel, Mr. Andrew Matthews, and Mr. James Hazeldine for their exceptional expertise and professional support in the laboratory work.

I would also like to acknowledge the generous financial support provided by the China Scholarship Council, which has significantly contributed to the successful completion of my PhD study. Furthermore, I am grateful for the academic exchanges facilitated by the ThermaSMART project, as it has offered me valuable opportunities to engage with fellow researchers and broaden my academic perspective.

Lastly, I extend my heartfelt gratitude to my parents for their unwavering support and unconditional love. Their encouragement has guided me through challenging times and inspired me to pursue my goals.

To all those mentioned above, I sincerely thank you for your unwavering support. The journey of obtaining my PhD has been an invaluable treasure in my life, and I will cherish these memories indefinitely, regardless of time and distance.

Table of Contents

Investigation on thermal and kinetic dynamics of droplets

Abstract.....	I
List of publications during PhD study	III
Acknowledgement	IV
Table of Contents.....	V
List of Figures.....	VII
List of Tables	X
Nomenclature.....	XI
Chapter 1. Introduction	1
1.1 Background	1
1.2 Research Objectives	4
1.3 Organization of the Thesis	5
Chapter 2. Literature review	7
2.1 Surface wettability and contact angle.....	7
2.2 Droplet evaporation.....	10
2.3 Leidenfrost effect	16
2.4 Droplet impingement.....	18
Chapter 3. Lattice Boltzmann Method Theory	22
3.1 Introduction	22
3.2 The Lattice Boltzmann Equation.....	26
3.3 Boundary Conditions.....	30
3.4 The multi-component multiphase models	32
3.5 Numerical model used in this thesis.....	41
Chapter 4. Investigation on the droplet evaporation process on localised heated substrates with different wettability	47
4.1 Introduction	48
4.2 Results and Discussion.....	51
4.3 Conclusion.....	69
Chapter 5. Droplet impingement on a conical obstacle: A lattice Boltzmann study	71

5.1 Introduction	72
5.2 Numerical Methodology	76
5.3 Results and Discussion.....	84
5.4 Conclusion and Propection	94
Chapter 6. Investigation on droplets impacting a conical structure.....	95
6.1 Introduction	96
6.2 Experiment set-up	99
6.3 Results and Discussion.....	102
6.4 Impact Dynamic	111
6.5 Summary	120
Chapter 7. Conclusion and outlook.....	121
7.1 Conclusion of the current work.....	121
7.2 Outlook for future work	123
References	125
Appendix: C++ code.....	139

List of Figures

Fig. 1-1 Subject area distribution of topic “droplet evaporation and impingement” in Scopus database (1972-2022).....	1
Fig. 2-1 Force balance at the three-phase contact line[5].....	7
Fig. 2-2 Schematic of droplet wetting on micro-structured surfaces (a) Wenzel model (b) Cassie-Baxter model[15]	9
Fig. 2-3 Schematic of the different evaporation modes[44].....	11
Fig. 2-4 Different outcomes of droplets impinging on a dry surface[85].....	18
Fig. 3-1 Basic flowchart of the Lattice Boltzmann method	24
Fig. 3-2 Schematic of (a) standard bounce-back scheme and (b) half-way bounce-back scheme.....	30
Fig. 4-1 Schematic of a droplet placed on a superhydrophobic surface. (CA = 150°).....	51
Fig. 4-2 Model verification results. (a) Comparison of the volume change throughout the evaporation process. (b) Comparison of the contact angle change throughout the evaporation process.....	52
Fig. 4-3 Schematic of the simulation of the standard evaporation process	53
Fig. 4-4 Evolution of isotherms at the initial state of evaporation. (a) Time step = 1000. (b) Time step = 5000. (c) Time step = 10000. (d) Time step = 20000.	54
Fig. 4-5 Morphology of the droplet in the evaporation process under different superheat temperatures. (Contact angle = 90°, substrate heating) (a) the volume evolution to time. (b) the contact angle evolution to time.	55
Fig. 4-6 Schematic of simulation of droplet evaporation under localised heating. (A and C: $T = T_h$; B: $T = T_h$).....	57
Fig. 4-7 Streamlines inside the droplet on substrates with different wettability under localised heating conditions. (a-d: contact angle = 30°, $L_c = 0, 0.5, 1, 1.5$; e-h: contact angle = 60°, $L_c = 0, 0.5, 1, 1.5$; i-l: contact angle = 90°, $L_c = 0, 0.5, 1, 1.5$; m-o: contact angle = 120°, $L_c = 0, 0.5, 1$)	60
Fig. 4-8 Temperature distribution in the flow field of droplets with different contact angles under localised heating conditions. (a-d: contact angle = 30°, $L_c = 0, 0.5, 1, 1.5$; e-h: contact angle = 60°, $L_c = 0, 0.5, 1, 1.5$; i-l: contact angle = 90°, $L_c = 0, 0.5, 1, 1.5$; m-o: contact angle = 120°, $L_c = 0, 0.5, 1$).....	62
Fig. 4-9 Interface temperature profile for a droplet with contact angle = 90°	63
Fig. 4-10 Evolution of droplet volume under localised heating conditions. (a) contact angle = 30°; (b) contact angle = 60°; (c) contact angle = 90°	64

Fig. 4-11 Evolution of the contact angle for droplets on substrates with different surface wettability under different localised heating conditions. (a), (b), (c): evolution of contact angles of the droplet with basic contact angles at 30°, 60° and 90°	66
Fig. 4-12 Droplet position evolution under asymmetric localised heating conditions when placed on a smooth substrate. (a) Contact angle = 30°; (b) Contact angle = 60°; (c) Contact angle = 90°	68
Fig. 5-1 Schematic of the simulation domain.....	77
Fig. 5-2 Illustration of the hypotenuse boundary treatment using Filippova and Hänel's scheme.....	77
Fig. 5-3 The relationship between the pressure drops at the droplet interface and droplet radius for different temperatures. (σ : surface tension).....	80
Fig. 5-4 Normalised square of droplet diameter versus the evaporating time.....	81
Fig. 5-5 Different wetting conditions of the droplet on the cone hypotenuse achieved by adjusting coefficient G_s	83
Fig. 5-6 Droplet impingement on the cone vertex under different gravity magnitudes ...	87
Fig. 5-7 Snapshot of the droplet impinging on surfaces of different wettability (a: contact angle = 69.9°; b: contact angle = 88.5°; c: contact angle = 104.5°; d: contact angle = 120.4°. Green line: $t^* = 2.31$; red line: $t^* = 3.46$; blue line $t^* = 4.91$; black line: $t^* = 8.08$)	88
Fig. 5-8 Evolution of droplet position upon impingement on surfaces of different wettability. (Position unit: l.u.)	89
Fig. 5-9 Snapshot of the droplet impinging on surfaces of different temperatures. (a: $dT = 0.05$; b: $dT = 0.1$; c: $dT = 0.2$; d: $dT = 0.3$. Green line: $t^* = 2.31$; red line: $t^* = 3.46$; blue line $t^* = 4.91$; black line: $t^* = 8.08$).....	90
Fig. 5-10 Temperature profiles of the flow field at $t^* = 3.46$ for different surface temperatures. (a: $dT = 0.05$; b: $dT = 0.1$; c: $dT = 0.2$; d: $dT = 0.3$)	91
Fig. 5-11 Mean temperature of the droplet during the impingement process.	92
Fig. 6-1 Schematics of experimental apparatus.....	99
Fig. 6-2 Surface contact angle of water droplets on aluminium substrates (a) roughness = 0.2 μm (b) roughness = 21.8 μm (c) roughness = 125 μm	101
Fig. 6-3 Images of a water droplet impacting a relatively smooth aluminium conical structure with a 60° cone angle at different Weber numbers.....	103
Fig. 6-4 Images of a water droplet impacting a relatively smooth aluminium conical structure with a 90° cone angle at different Weber numbers.....	105
Fig. 6-5 Images of a water droplet impacting a relatively smooth aluminium conical structure with a 120° cone angle at different Weber numbers.....	107

Fig. 6-6 Images of a water droplet impacting a rough aluminium conical structure with a 60° cone angle at different Weber numbers. (Roughness = 21.8µm).....	108
Fig. 6-7 Images of a water droplet impacting a rough aluminium conical structure with a 60° cone angle at different Weber numbers. (Roughness = 125µm).....	109
Fig. 6-8 Images of a water droplet impacting the conical aluminium structure with different surface roughness for We = 16 and cone angle = 120°.....	110
Fig. 6-9 The variation of droplet spreading factor of droplet impacts on a relatively smooth conical structure (R _a = 0.2µm) as a function of time for different conical structures with various cone angles; (a) cone angle = 60°, (b) cone angle = 90°, (c) cone angle = 120°	112
Fig. 6-10 The variation of droplet spreading factor of droplet impact on a relatively smooth conical structure (R _a = 0.2µm) with different Weber numbers as a function of time; (a) We = 16, (b) We = 258, (c) We = 501	114
Fig. 6-11 The variation of droplet spreading factor of droplet impacts on a conical structure (cone angle = 60°) with different roughness and as a function of time; (a) We = 16, (b) We = 258, (c) We = 501	116
Fig. 6-12 The variation of the critical Weber number for splashing to the surface roughness for various cone structure with different cone angles.....	117
Fig. 6-13 Snapshot of the formation process of secondary droplets	118

List of Tables

Table 180
Table 286

Nomenclature

Symbols

A_p	pore area	m^2
A_s	surface area	m^2
Bo	Bond number	-
c	reference lattice velocity	-
c_p	heat capacity at constant pressure	$\text{J}\cdot\text{kg}\cdot\text{K}^{-1}$
c_s	lattice sound speed	-
c_v	heat capacity at constant volume	$\text{J}\cdot\text{m}^{-3}\cdot\text{K}^{-1}$
C	concentration	-
d	diameter	m
D	diffusion coefficient	$\text{m}^2\cdot\text{s}^{-1}$
e	lattice velocity vector	-
f	distribution function	-
F	force	N
g	gravity acceleration	$\text{m}\cdot\text{s}^{-2}$
G	interaction parameter	-
g	thermal distribution function	-
h	height	m
h_{lv}	liquid/vapour latent heat	kJ/kg
Ja	Jakob number	-
l	length	m
L	droplet contact line radius	m

L_c	heat source location	-
La	Laplace number	-
m	MRT vector parameter	-
M	Orthogonal transformation matrix	-
m	mass	kg
M	molecular mass	u
Ma	Marangoni number	-
Oh	Ohnesorge number	-
p	pressure	Pa
P_s^v	vapour pressure at the droplet surface	Pa
q	relative distance of fluid nodes used in Filippova and Hänel's scheme	lattice unit
R	gas constant	$J \cdot K^{-1} \cdot mol^{-1}$
R_a	surface roughness parameter	μm
R_{pk}	average height of protruding peaks above roughness core profile	m
R_s	radius of droplet	m
R_{sm}	mean width of a profile element	m
Ra	Rayleigh number	-
Re	Reynold number	-
t	time	s
T	temperature	K
T_s	saturated temperature	K
u	velocity vector	$m \cdot s^{-1}$
U	Overall velocity	$m \cdot s^{-1}$
W	width of the droplet interface	lattice unit

We	Weber number	-
x	position	m

Greek symbols

α	thermal diffusivity	$\text{m}^2 \cdot \text{s}^{-1}$
β	spreading factor	-
ε	thermal expansion coefficient	K^{-1}
η	dynamic viscosity	$\text{Pa} \cdot \text{s}$
θ	contact angle	-
λ	thermal conductivity	$\text{W} \cdot \text{m}^{-1} \cdot \text{K}^{-1}$
Λ	diagonal matrix of relaxation times	-
ν	kinematic viscosity	$\text{m}^2 \cdot \text{s}^{-1}$
ρ	density	$\text{kg} \cdot \text{m}^{-3}$
σ	surface tension	$\text{N} \cdot \text{m}^{-1}$
τ	relaxation time	-
φ	phase change term	-
ψ	pseudopotential	$\text{kg} \cdot \text{m}^{-3}$
ω	weight factor	-
Ω	collision operator	$\text{kg} \cdot \text{m}^{-3} \cdot \text{s}^{-1}$

Sub/super-scripts

avg	average
b	boundary

<i>c</i>	critical
CB	Cassie-Baxter
<i>eq</i>	equilibrium state
<i>f</i>	fluid
<i>g</i>	gravity
<i>h</i>	heated
<i>i, j</i>	direction
l	liquid
max	maximum
s	solid
v	vapour
<i>w</i>	wall
W	Wenzel
<i>x</i>	horizontal coordinate
<i>y</i>	vertical coordinate
Y	Young's equation
σ	detonating a type of component
0	initial

Abbreviations

BGK	Bhatnagar-Gross-Krook
CCA	Constant contact angle
CCR	Constant contact radius
CFD	Computational fluid dynamics

CS	Carnahan-Starling
DDF	Double distribution function
DNS	Direct Numerical Simulation
DSMC	Direct Simulation Monte Carlo
EOS	Equation of state
IR	infrared
LB(M)	Lattice Boltzmann (method)
LES	Large Eddy Simulation
LGA	Lattice gas automata
l.u.	Lattice unit
MCMP	Multi-component multiphase
MD	Molecular dynamics
MRT	Multi-relaxation time
PIV	Particle Image Velocimetry
PR	Peng-Robinson
RANS	Reynolds-averaged Navier-Stokes
RK	Redlich-Kwong
RKS	Redlich-Kwong-Soave
SCMP	Single-component multiphase
SRT	Single relaxation time
vdW	van de Waals
VOF	Volume of fluid
ZSC	Zheng-Shu-Chew

Chapter 1. Introduction

1.1 Background

The intriguing behaviour of droplets, which represents one of the most pervasive phenomena in the natural world, has garnered significant research interest in recent decades. From the interaction of raindrops with lotus leaves to their diverse applications in various industries, such as inkjet printing, spray cooling, DNA microarrays, and nanotechnology, droplets have become ubiquitous in the modern world. Consequently, it is imperative to acquire a comprehensive understanding of their characteristics and behaviours.

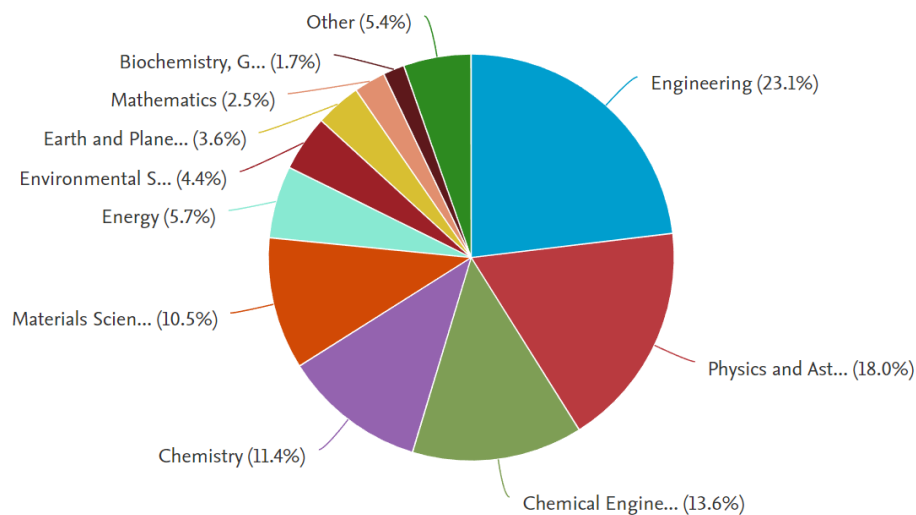


Fig. 1-1 Subject area distribution of topic "droplet evaporation and impingement" in Scopus database (1972-2022)

Despite the extensive research conducted thus far, the understanding of droplets remains somewhat limited, and there are numerous unexplored aspects due to the complex mechanisms governing their thermodynamic behaviours. The study of droplets, particularly in relation to evaporation and impingement, has been the subject of intense investigation over the past few decades, as evidenced by the publication of more than 18,000 papers in the Scopus database. This research spans a broad spectrum of disciplines, encompassing fields

such as general engineering, physics and astronomy, chemical engineering, and materials science.

Advancements in technology have significantly propelled droplet research to new heights, thanks to the introduction of devices such as high-speed cameras, IR cameras, and Particle Image Velocimetry (PIV). These cutting-edge technologies have enabled the observation of phenomena that were previously unattainable, including detailed insights into the flow field and temperature distribution of droplets. Consequently, this has opened doors for further in-depth investigations. In recent years, researchers have shifted their focus towards studying the fundamental mechanisms underlying droplet behaviour. This encompasses phenomena such as surface tension, wetting, phase change behaviours (evaporation and condensation), and droplet motion, including collision, impingement, and applications utilising physical phenomena like the Marangoni effect and Leidenfrost effect. However, experimental studies still encounter challenges due to limitations in observation and measurement technologies, primarily due to the small-scale and transient nature of droplet behaviour. Consequently, Computational Fluid Dynamics (CFD) has emerged as an indispensable tool for studying droplets.

In recent decades, computational technologies have undergone rapid development, leading to the proposal of more efficient and accurate numerical models. Since the introduction of the Reynolds-averaged Navier-Stokes equations (RANS) as a foundational concept for CFD in the 1970s, novel numerical models for heat and mass transfer computations have made significant advancements. On the macroscale, models based on the continuum assumption, such as Large Eddy Simulation (LES) and Direct Numerical Simulation (DNS), have demonstrated remarkable success. On the microscale, particle tracking models have enriched the fundamental understanding of fluid dynamics, exemplified by Molecular Dynamics (MD) and Direct Simulation Monte Carlo (DSMC) methods.

Introduced in the 1990s, the Lattice Boltzmann Method (LBM) operates at the mesoscopic scale, bridging the gap between macroscopic and microscopic approaches. By virtue of its mesoscopic nature, LBM allows for the investigation of fluid dynamic mechanics from a fundamental level while maintaining computational efficiency. Consequently, LBM has emerged as a powerful tool for simulating droplet behaviours and is gaining popularity due to its various advantages.

1.2 Research Objectives

The primary objective of this thesis is to advance the understanding of the kinetic and thermal dynamics of droplets, encompassing their interactions with surfaces of varying wettability and roughness, impingement behaviour, and evaporation characteristics. The investigation will delve into the Marangoni effect and the Leidenfrost effect. Another objective is to explore the broader application of the Lattice Boltzmann method in droplet research while analysing its advantages and limitations in this particular field. To accomplish these objectives, numerical study is conducted to simulate the droplets' evaporation and impingement, while the experimental investigation of droplet impingement further examines the influence of surface roughness and substrate geometry. The specific objectives can be summarised as follows:

- Investigate droplet evaporation under localised heating conditions, analyse the flow field and temperature distribution throughout the evaporation process.
- Assess the impact of temperature gradient on Marangoni flow and examine factors such as temperature, heat source locations, and surface wettability.
- Utilise numerical simulations to study the process of droplet impingement on conical structures, investigating the effects of temperature, impact velocity, and surface wettability.
- Investigate the behaviour of droplet impingement in the Leidenfrost regime.
- Conduct experimental studies on droplet impingement on conical obstacles, considering factors such as impact velocity, cone angle, and surface roughness.

By pursuing these research objectives, I aim to contribute to the current knowledge and understanding of droplet dynamics while also exploring the potential of the Lattice Boltzmann method as a valuable tool in droplet research.

1.3 Organization of the Thesis

The thesis comprises a total of seven chapters, each focusing on distinct aspects to comprehensively address the aforementioned objectives.

Chapter 2 provides an extensive literature review that encompasses various research directions concerning droplets. Existing knowledge is summarised, serving as the foundation for the ongoing investigation. Topics covered include surface wettability, droplet evaporation, impingement, and the Leidenfrost effect.

Chapter 3 offers a comprehensive introduction to the lattice Boltzmann method, tracing its historical development and delving into specific aspects such as the LB equation and boundary conditions. Furthermore, an evaluation of multi-component multiphase models is provided, as one of these models is subsequently applied in the thesis.

Chapter 4 focuses on the investigation of Marangoni flow within droplets, presenting a numerical study involving localised heating of droplets. By applying controlled heating conditions, the analysis examines the Marangoni flow induced by temperature gradients and explores the effects of different heating parameters. The chapter includes a review of relevant studies and investigations into factors such as heat source temperature, heat source location, and surface wettability.

In Chapter 5, another numerical study explores droplet impingement on a heated conical surface. An improved treatment of boundary conditions is introduced to simulate the interaction between the droplet and inclined surface using LBM. The chapter investigates the behaviour of the droplet upon impingement on the conical obstacle, considering factors such as gravity, surface wettability, and temperature.

Corresponding to Chapter 5, Chapter 6 presents an experimental study, providing a more comprehensive analysis of droplet impingement on conical obstacles. The chapter

includes a literature review of relevant experimental studies, details of the experimental setup, and an illustration of the droplets' interaction with obstacles with varying surface roughness. The investigation examines the effect of surface roughness on impingement behaviour, explores the impact of cone angle and droplet velocity, and analyses the dynamics of the impingement theoretically.

The final chapter presents the conclusion of the research work, summarises the key findings, and provides an outlook for future research endeavours.

Chapter 2. Literature review

2.1 Surface wettability and contact angle

In 1612, Italian polymath Galilei[1] first recognised the phenomenon of wetting. He observed that when a thin film of liquid floats on a solid substrate, the free surface of the water is slightly higher than the solid substrate. Later in 1805, Young[2] systematically studied the wetting phenomenon, which laid the basis for the introduction of the famous Young's equation[3]:

$$\sigma_{sv} = \sigma_{sl} + \sigma_{lv} \cos \theta_Y \quad (2.1)$$

As the equation shows, three different surface tensions need to be considered to determine the contact angle θ_Y , as the wetting phenomenon involves different phases. The subscripts in the above equation s, l, v stand for solid phase, liquid phase, and vapour phase respectively. Therefore, the equation can be interpreted as the balance of forces at the triple-phase contact line, resulting in the contact line reaching a mechanical equilibrium. The adjustment of contact angles can be achieved by manipulating the surface tension ratios, as evident from Young's equation. Surface processing serves as a direct and effective means to

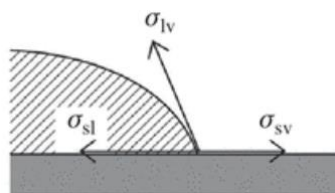


Fig. 2-1 Force balance at the three-phase contact line[4]

accomplish this. Based on the contact angle exhibited by a sessile droplet, the surface characteristics can be categorised into five types. These include the superhydrophilic surface (contact angle $< 30^\circ$), the hydrophilic surface (contact angle ranging from 30° to 90°), the

neutral surface (contact angle around 90°), the hydrophobic surface (contact angle ranging from 90° to 150°), and the superhydrophobic surface (contact angle greater than 150°)[5].

Surface tension ratios can be effectively adjusted through chemical processing of the surface, such as the application of sprays or autocatalytic plating. This alters the interaction force between the substrate and the fluid, leading to changes in the contact angles. Another approach involves the utilisation of surface texturing technology, which allows for the creation of microstructures on the surface. These microstructures modify the contact area between the liquid and the surface, consequently influencing the contact angles. Two commonly used models for droplet-wetting on microstructured surfaces are the Wenzel model and the Cassie-Baxter model. The Wenzel model describes situations where the surface exhibits sufficient adhesion, allowing the liquid to penetrate the roughness and fill the gaps between the protrusions. Meanwhile, when calculating the equilibrium contact angle, the volume of liquid stored in these gaps is not taken into consideration[6]. The apparent contact angle for the Wenzel model can be incorporated as[7]

$$\cos \theta_w = \gamma \cos \theta_y \quad (2.2)$$

where θ_w is the apparent contact angle, γ is the ratio between the actual surface area to the projected surface area, and θ_y stands for the contact angle of the droplet when placed on a smooth surface that can be acquired by Young's equation. The Cassie-Baxter model illustrates another situation where air pockets are trapped between the protrusion gaps. The apparent contact angle for the Cassie-Baxter model is defined as[8]

$$\cos \theta_{CB} = \eta \cos \theta_y - (1 - \eta) \quad (2.3)$$

where θ_{CB} is the apparent contact angle, and $\eta = \frac{\sum A_p}{\sum A_p + \sum A_s}$. A_p and A_s stand for the

pore and surface areas, respectively. Due to its ability to help researchers precisely control the wettability, considerable research is done to further reveal the mechanisms of droplet wetting on those models, including the transition between those two models[9, 10], evaporation[11], boiling[12], condensation[13] and motion[14].

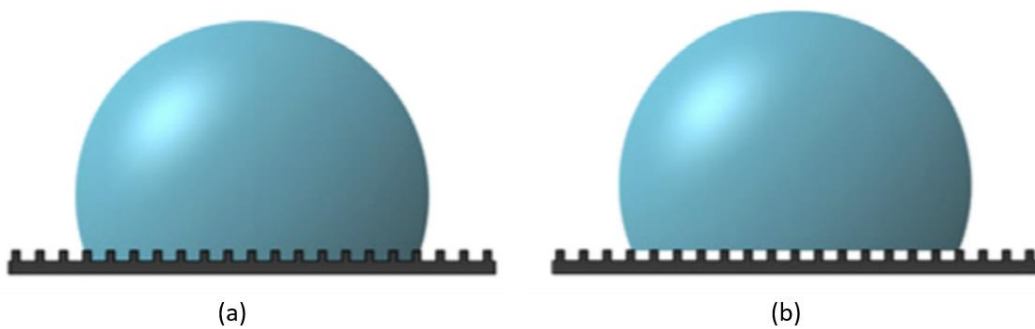


Fig. 2-2 Schematic of droplet wetting on micro-structured surfaces (a) Wenzel model (b) Cassie-Baxter model[15]

2.2 Droplet evaporation

The evaporation of droplets is omnipresent in people's everyday life as well as industrial applications, ranging from ink-jet printing[16, 17], spray cooling[18-20], material processing[21], particle synthesis[22, 23], fuel preparation[24, 25], fire extinguishing[26] to air humidifiers and heat exchangers[27]. In recent years, more medical applications have been developed for droplet evaporation, like DNA/RNA arrangement[28, 29] and new diagnosis technology[30, 31]. However, despite being commonly seen and widely used, the mechanism behind this phenomenon remains complicated, given that the mass transfer between liquid and vapour is coupled with the heat transfer involving three phases[32]. In this section, the two most prominent topics, evaporation dynamics and evaporation-driven flow motion, will be addressed.

As the heat transfer in the process of a droplet's evaporation contains heat conduction, convection and radiation, and it's too complicated to consider their effect simultaneously, researchers have taken a simplified approach when quantifying the evaporation flux by introducing an assumption of quasi-stationary droplets, where the rate of the evaporation process at any given moment equals to the rate of the stationary process with the boundary conditions obtained at that moment[33]. For spherical droplets, the evaporation flux equation has evolved from the one proposed by Maxwell[34], which considers only the diffusion caused by concentration difference, to the famous Langmuir equation[35], which takes into account the effect of temperature on the surrounding vapour, given as

$$-\frac{dm}{dt} = \frac{4\pi MDP_s^v}{RT} R_s \quad (2.4)$$

where P_s^v is the water vapour pressure at the droplet's surface, R is the gas constant, M is the molecular weight, D is the diffusion coefficient, and R_s is the radius of the spherical droplet.

For sessile droplets, Picknett and Bexon[36] pointed out that the presence of the solid substrate hinders the evaporation rate. Based on the assumption that the mass transfer is controlled by diffusion under isothermal conditions, the theoretical model for sessile droplet evaporation is given as[37]:

$$-\frac{dm}{dt} = 2\pi DL\Delta C f(\theta) \quad (2.5)$$

where L is the contact line radius, ΔC is the vapour concentration difference between the droplet surface and the ambient air, and $f(\theta)$ is a function of the contact angle. Also, it's found that the triple-phase contact line packs the most intensive evaporation rate in the case of contact angles $\theta < 90^\circ$. The reason, however, was explained utilising different principles by different researchers[38-43].

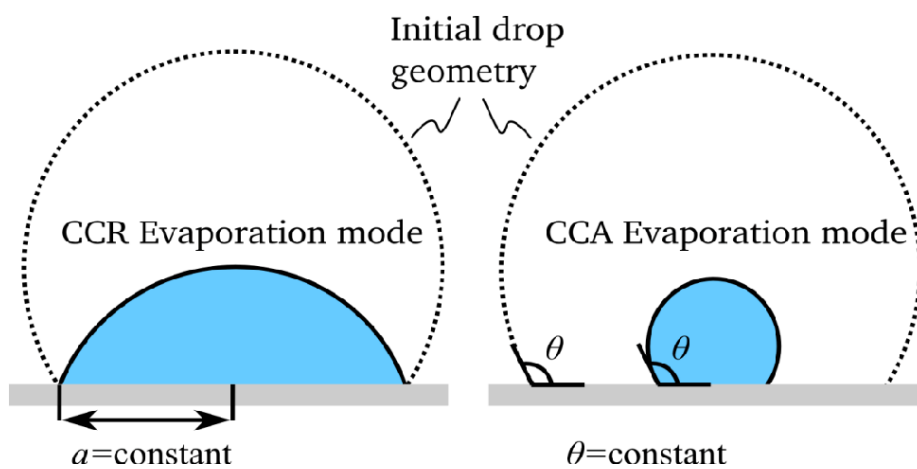


Fig. 2-3 Schematic of the different evaporation modes[44]

Regarding the wetting phenomenon between the droplet and the substrate, various wetting modes can be observed during evaporation. These modes are primarily determined by the behaviour of the triple-phase contact line. Two prominent evaporation modes can be identified based on this criterion: the Constant Contact Radius (CCR) mode and the Constant Contact Angle (CCA) mode. In the CCR mode, the droplet maintains a fixed contact line with the substrate while the contact angle steadily decreases. On the other hand, the CCA mode corresponds to a fixed contact angle, accompanied by the shrinking of the contact line. It is worth noting that more complex evaporation modes can arise through the alternation or combination of these two primary modes. In the work of Doganci et al.[45], they observed three different stages of evaporation of a sessile droplet placed on a hydrophobic surface: CCR to CCA and finally mixed in chronological order. Much effort has been put into figuring out the factor of the evaporating modes, and it's found that the surface wettability[44, 46, 47], surface roughness[48] and temperature[49, 50] can affect the evaporation modes.

The droplet's evaporation could induce the flow inside a droplet in various ways. To the best of the author's knowledge, there are at least four different types of evaporation-driven flows:

- Capillary flow arising from surface tension. Surface tension inherently seeks to minimise the surface area of a droplet. When evaporation causes a change in the droplet's shape, the resulted mass loss from the droplet's surface triggers the generation of capillary flow. This phenomenon becomes particularly evident when the local evaporation rate on the droplet's surface deviates from the constraints imposed by the droplet's spherical cap shape or contact-line motion, in other words, when a non-uniform evaporation rate distribution on the droplet's surface occurs. The alteration of the equilibrium droplet surface leads to the development of Laplace

pressure, which propels the capillary flow. The magnitude of the Laplace pressure can be quantified by the Laplace number, which is written as:

$$La = \frac{\rho l \sigma_{lv}}{\eta^2} \quad (2.6)$$

where σ stands for the surface tension, l is the characteristic length of the fluid system, usually the thickness of the liquid film, while for droplets, it usually takes its radius. η is the viscosity of the liquid.

- The internal flow brought by the morphology of the dropwise, for example, a moving contact line. In CCR mode, the outward flow is enhanced than that in CCA mode, as a more significant mismatch between the evaporation rate and the constrained motion of the liquid-air interface promotes the capillary flow[51], while the shrinking droplet height pushes the liquid outwards as well.
- Marangoni flow refers to a flow pattern that arises due to the presence of a surface tension gradient. This flow directs the fluid motion from regions with lower surface tension to regions with higher surface tension. The magnitude of the Marangoni flow can be quantified using the Marangoni number, which represents the ratio between the flow induced by the Marangoni effect and the diffusive flow responsible for generating the surface tension gradient. The surface tension gradient itself can be caused by non-uniform temperature distribution or concentration distribution (in the case of mixtures with more than one component) within the droplet. The Marangoni number Ma can be given in the two forms as below[52]:

$$Ma_T = -\frac{d\sigma_{lv}}{dT} \frac{l\Delta T}{\eta\alpha} \quad (2.7)$$

$$Ma_c = \frac{d\sigma_{lv}}{dC} \frac{l\Delta C}{\eta D} \quad (2.8)$$

From the equations, one can see that the Marangoni number indicates the ratio of the surface tension gradient to the adhesive force. Equation (2.7) gives the Marangoni number in thermal induced Marangoni flows. α is the thermal diffusivity of the liquid. In Equation (2.8), C is the concentration of the solute and D is the diffusion coefficient. As the surface tension increases with the decrease in temperature, the surface tension gradient will direct the Marangoni flow from the hotter area to the colder area[53]. The strength of the Marangoni flow is intricately influenced by two factors: the magnitude of the surface tension gradient and the size of the droplet. In the case of concentration-induced Marangoni flow, the underlying mechanism bears a close resemblance, with the exception that the temperature gradient is replaced by a concentration gradient. Consequently, this type of Marangoni flow exclusively manifests in multi-component systems, such as solvent solutions. As the concentration of solutes rises, leading to an increase in surface tension, the Marangoni flow prompts fluid motion from areas with higher concentrations towards those with lower concentrations.

- The internal flow driven by natural convection, like buoyance and thermophoresis. Those flows are driven by the density difference caused by the temperature difference, and it can be expressed by the Rayleigh number:

$$Ra = \frac{\varepsilon \rho g \Delta T l^3}{\eta \alpha} \quad (2.9)$$

where ε is the thermal expansion coefficient of the liquid, g is the gravitational acceleration. When the Rayleigh number is high enough, convection can replace heat conduction and becomes the dominant factor. According to research, the ratio between the Marangoni number and Rayleigh number is in the order of 10^4 - 10^5 , which means that compared to the Marangoni flow, the gravity-driven flow is much weaker and neglectable. However, in experimental conditions, due to the presence of monolayers of surfactants,

which forms a monolayer on the droplet surface[54], the surface tension of the droplet is always weakened, and thus Marangoni flow can be suppressed[55]. That could allow the gravity-driven flow to prevail in real-life conditions.

2.3 Leidenfrost effect

When placed on a superheated substrate, the evaporation rate of the droplet can be so fast that a vapour film is formed between the droplet and the substrate. The pressure of the vapour is sufficient to balance the weight of the droplet itself, so the droplet can maintain levitated for most of its lifetime. This phenomenon was first observed by the German physician Leidenfrost[56], after whom it's named. Due to the existence of the vapour film, the behaviour of the droplet can be changed dramatically: First, the vapour layer functions as an insulation layer due to the low thermal conductivity of the vapour, resulting in a reduced evaporating rate of the droplet. Second, due to the erased friction force between the droplet and the substrate, the droplet can move freely above the substrate at a much higher velocity than otherwise. When correctly taken advantage of, the motion of the droplet can be easily manipulated, widening the range of its potential application[57, 58].

One of the interests of the researchers is to determine the critical temperature for the Leidenfrost effect to happen. This is crucial in applications like the cooling of thermal-intensive units, as a higher critical temperature can delay the appearance of the vapour layer. However, the critical temperature concerns lots of factors, including the thermophysical properties of the liquid as well as the thermal conductivity and geometry of the substrate. Bernardin and Mudawar[59] concluded that the higher the thermal diffusivity of the substrate, as well as the lower the roughness of the substrate, the lower the critical temperature will be. However, Cerro et al.[60] studied the effect of micropatterned surface on the Leidenfrost effect and found that the micropatterned surface can lower the critical temperature by 70%. This is further applied in the recent research of Jiang et al.[12], the microstructured substrate in their study prevented the Leidenfrost effect from kicking in at a temperature above 1000°C.

Besides, lots of research has been carried out to study other prospects of the Leidenfrost effect. Ok et al.[61] and Cousins et al.[62] studied the controlled motion of Leidenfrost droplets on ratchet surfaces and found that a properly treated surface can not only control the direction of the droplet, but also accelerate the droplet to an unprecedented velocity. Quéré[63] reviewed the shape and stability of the Leidenfrost droplets and concluded that Leidenfrost droplet is a complex flow system with the coexistence of viscous flow and inertial flow, and with the progression of evaporation, both the shape of the droplet and the vapour film changes dramatically. Other researchers[64, 65] focused on the evaporation rate of those levitating droplets and pointed out that the evaporation rate densifies near the vapour film for large droplets, while for smaller droplets, the evaporation rate shows a more averaged distribution around the droplet surface.

2.4 Droplet impingement

Droplet impingement is one ubiquitous phenomenon that widely exists in nature and has been studied for more than 140 years since the works of Worthington in 1876[66]. The impingement of droplets is one of the most important directions of research towards droplets due to its vast applications, including injection combustion engines[67, 68], metal quenching[69], spray coating[70-72] and spray cooling[73-77], oil recovery[78] and ink-jet printing[79-83]. Despite that the topic has been researched for more than 140 years, it was until the invention of high-speed video technology that the dynamic process of impact was revealed[84] due to its small scale both in size and time. There are two major types of droplet impingement, one is impingement on wet surfaces, the other is on dry surfaces. Compared to impinging on wet surfaces the phenomenon of which shows mainly splashing, the latter shows a variety of scenarios for the more complex interaction involving different phases[85].

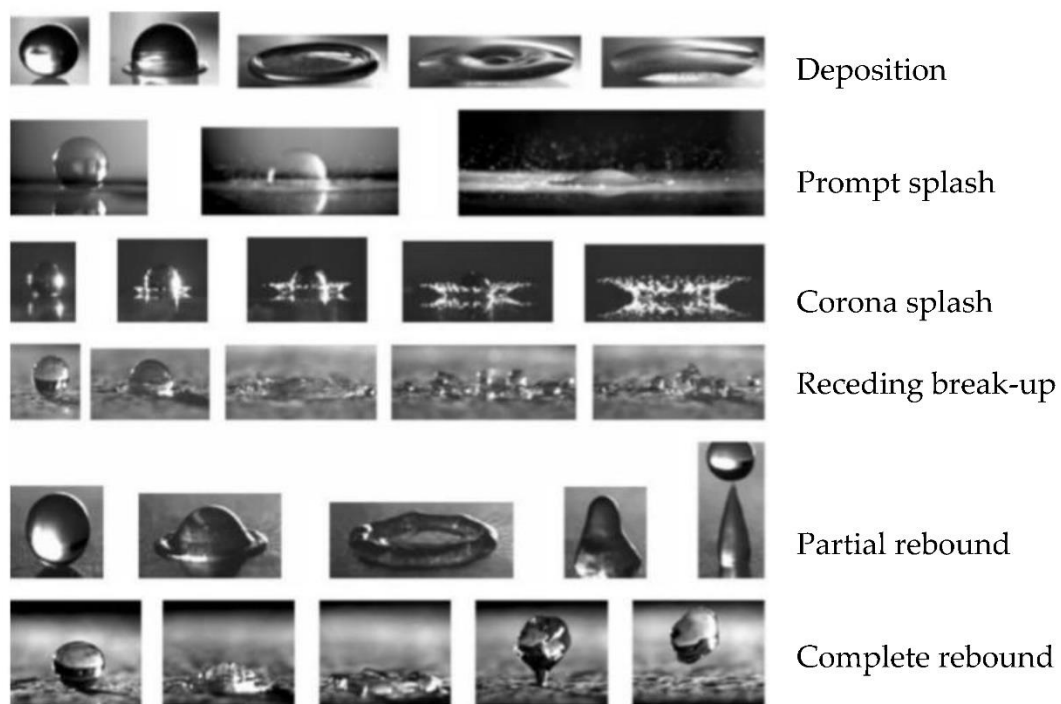


Fig. 2-4 Different outcomes of droplets impinging on a dry surface[85]

Six potential scenarios have been identified following the impact of a droplet on a dry surface, namely deposition, prompt splash, corona splash, receding breakup, partial rebound, and complete rebound. To gain insight into the factors influencing these scenarios, it is crucial to comprehend the distinct phases involved in the impingement process. The initial phase is characterised as the spreading phase, which typically occurs under conditions of low Weber number and surface temperature. During this phase, the droplet's kinetic energy undergoes conversion into surface energy or dissipated heat[86]. The magnitude of the spreading phase is measured by the maximum spreading factor, given as $\beta_{\max} = \frac{d_{\max}}{d_0}$, where

d_{\max} is the max droplet diameter during the spreading phase, and d_0 is its initial diameter.

The maximum spreading factor of a droplet is influenced by both the impact velocity and the surface properties, which will be elaborated upon in Chapter 6. Following the spreading phase, the droplet typically transits into the receding phase due to the effects of surface tension. The behaviour of the receding phase can be influenced by factors such as droplet shape and its intrinsic properties, which govern the surface tension. Subsequently, the droplet may exhibit either rebounding or splashing phenomena, contingent upon the surface wettability, temperature, and the remaining kinetic energy within the droplet.

The above-mentioned scenarios in Fig. 2-4 can be affected by many factors, including the initial velocity of the droplet, droplet size and shape, viscosity, and surface properties such as roughness, wettability, and temperature[85, 87]. The initial velocity directly affects the kinetic energy of the droplet, making the droplet unlikely to deposit on the surface and instead increasing the chance of droplet splashing and rebounding[88]. Furthermore, upon impact, the vertical kinetic energy of the droplet undergoes a horizontal redirection. A higher initial kinetic energy results in a larger maximum spreading factor and an expanded contact area between the droplet and the surface, thereby amplifying the influence of surface

temperature. Chen et al.[89] found that a higher surface temperature is needed to trigger the Leidenfrost effect when the impacting velocity is high, as a flatter droplet is more likely to be pierced by vapour bubbles and thus breaks the Leidenfrost state. The stability of a droplet is influenced by its size, wherein larger droplets exhibit lower surface tension as their shape undergoes changes. Additionally, larger droplets possess higher kinetic energy and lower surface tension at the same impacting velocity, thereby increasing the likelihood of splashing. Moreover, larger droplets often exhibit asymmetry in shape, which diminishes the tendency for rebounding.[90]. Viscosity plays a crucial role in moderating the internal flow dynamics of a droplet, as it introduces a greater frictional force that decelerates both the spreading and receding stages, causing the dissipation of kinetic energy at an accelerated rate. As a result, a droplet with higher viscosity exhibits reduced tendencies for splashing or rebounding, while displaying a heightened propensity for deposition.

Regarding the surface, the most discussed factors are temperature and wettability. On supercooled surfaces, the receding phase can be inhibited as the droplet solidifies rapidly when the maximum spreading factor is reached. Also, a cool surface increases the surface tension of the droplet, reducing the chance of splashing. Five stages are observed in the process of the droplet freezing on supercooled surfaces[91], and typically, the droplet shows a pointy shape when completely solidified[92]. On surfaces subjected to superheating, various phenomena can be observed, contingent upon the temperature conditions. Elevated temperatures contribute to a reduction in surface tension, thereby increasing the occurrence of splashing on heated surfaces. When the temperature reaches the boiling point of the droplet, a phenomenon known as nuclear boiling becomes apparent, characterised by the generation of vapour bubbles between the droplet and the surface. This induces instability within the droplet and facilitates the formation of secondary droplets[93]. As the temperature keeps increasing, the Leidenfrost regime is entered, allowing the droplet to rebound more easily.

Surface wettability is another key factor and affects the impingement process in multiple ways. The maximum spreading factor is lower on surfaces with lower wettability[92], also, as hydrophobic surfaces present the impingement with a smaller kinetic energy loss, the chance of droplet rebounding increases. The surface wettability also affects the way surface temperature works on the impingement, as hydrophobic surfaces slow down the effect of temperature due to a reduced contact area. For the Leidenfrost regime, it's found that a more hydrophilic surface leads to a higher critical temperature of Leidenfrost [94], and it's further validated in Chapter 5.

Relatively, the effect of surface roughness is less studied compared to temperature and wettability, thus, the mechanism behind it remains unclear. In addition to its influence on the dynamic contact angle of the droplet, surface roughness plays a significant role in the microscale dynamics of droplets. The intricate geometry of a rough surface affects the behaviour of droplets in a more nuanced manner. Previous studies on surface roughness have revealed that increased roughness facilitates the generation of secondary droplets[95, 96] as the rough surface increases the instability of the droplet surface, the spreading phase will be hindered and the droplet is propelled towards the Wenzel wetting mode[97]. Quetzeri-Santiago et al.[98] and Roisman et al.[99] carried out more detailed research to find out the influence of surface roughness on the splashing threshold, and pointed out that the roughness slope, instead of amplitude average roughness, is the factor that determines the splashing threshold, and empirical correlations were proposed. Wang et al.[100] recorded the droplet impacting a surface with the help of digital inline holographic imaging. The surface roughness affects the morphology, velocity, and mass-loss rate of splashing droplets.

Chapter 3. Lattice Boltzmann Method Theory

3.1 Introduction

From a physical standpoint, a fluid can be regarded as a discrete system comprised of an immense number of particles, wherein each particle engages in random thermal motion, exchanging momentum and energy. Depending on the scale considered, the characteristics of a fluid vary from uniformity, determinism, and continuity on a macroscale to inhomogeneity, discreteness, and randomness on a microscale. Consequently, the numerical models employed to describe fluid motion differ accordingly. Broadly speaking, fluid systems can be categorised into three models: macroscale, mesoscale, and microscale. Macroscale models perceive the fluid as a continuous medium filling the domain, employing sets of partial differential equations such as the Navier-Stokes equation to elucidate fluid motion. On the other hand, microscale models focus on individual fluid molecules, tracking their motion and statistically calculating the overall fluid behaviour. Molecular Dynamics Method represents a quintessential example of a microscale approach.

Nevertheless, both macroscale and microscale models possess certain limitations. Macroscale methods, relying on the assumption of fluid continuity, may not be applicable in scenarios involving thin fluids, such as simulating gas flow at extremely high altitudes. Conversely, microscale models that track individual particles necessitate extensive computational resources, particularly when dealing with flow systems comprising billions of particles. Furthermore, these models face constraints regarding spatial and temporal scales. In contrast, mesoscale models do not rely on the continuity hypothesis and offer a more balanced approach. They operate at moderate spatial and temporal scales, enabling efficient resolution of the fluid field while overcoming the computational demands associated with microscale models.

As one of the mesoscale models, Lattice Boltzmann Method has received growing attention in recent decades for its various advantages. Dating back to 1988, some researchers proposed the basic framework of LBM based on Lattice Gas Automata (LGA). LGA is a CFD model that assumes fluid as a large number of particles residing on grids. They collide with and stream to their neighbouring nodes following specific rules, exchanging momentum and energy, and the macroscale values are obtained by statistical averaging[101, 102]. Due to some disadvantages of the LGA model such as statistical noise, complexity and the relevance between pressure and velocity, LBM was developed. In LBM, the particle distribution function is used to replace the particle itself in LGA for evolution. Also, the Fermi-Dirac distribution used in LGA is replaced by the Boltzmann distribution to satisfy Galilean invariance.

In order to erase the statistical noise, McNamara and Zanetti et al. proposed that the evolution can be performed using the particle distribution function generated from the statistical mean of Boltzmann variables in LGA[103] instead of the particle itself. This was the earliest LBE model, although the collision step in this model remained unchanged from LGA and thus was still complicated. In 1989, Higuera et al.[104, 105] worked on the equilibrium distribution function and collision operator, making them independent from the LGA model, and the complexity of the model has been reduced greatly since. In 1991 and 1992, a simpler model was brought forward by some researchers, namely Single Relaxation Time (SRT) model or Bhatnagar-Gross-Krook (BGK) model[106-108]. The collision process was replaced by an equilibrium relaxation process, and the collision matrix is determined by the relaxation time. This model reduced the computational resource greatly and the Navier-Stokes equation can be derived from this model under some conditions, bringing research in the LBE to a new level. Shortly afterwards, d'Humeriers[109] proposed another model which uses multiple relaxation times in the collision operator, which improved the performance of

the model greatly regarding stability and accuracy. The model was thus referred to as the Multi-Relaxation Time (MRT) model. Nathen[110] compared the MRT scheme against the BGK scheme, and proved that under the same grid density, the MRT scheme is capable of maintaining stability and delivering more accurate results, while in some cases the MRT scheme could fail to converge due to its high order moments.

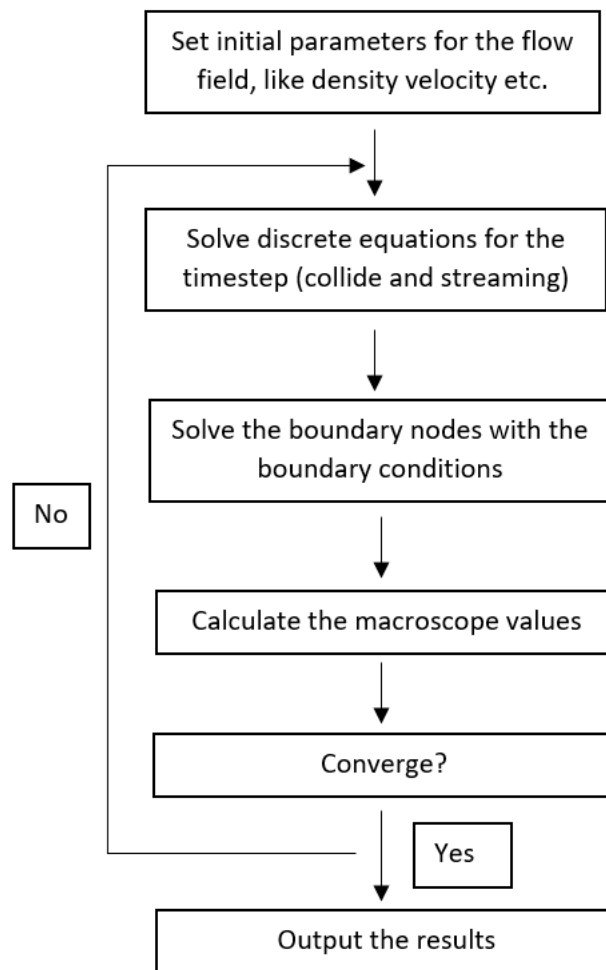


Fig. 3-1 Basic flowchart of the Lattice Boltzmann method

Compared to the conventional CFD methods, LBM has more than the following advantages: clear physical meaning, flexible boundary conditions, convenient programme, good parallel performance and robustness[111]. With LBM being applied to a growing range

of fields, more advanced models are being put forward to strengthen its capability to solve more complex and specified problems. To study the heat transfer in flows, double distribution function (DDF) models[112, 113] are introduced, which contain a second distribution function for the temperature field; To study multiphase and multi-component flow systems, the colour-gradient model, pseudopotential model, free energy model and the phase field model were developed, and they will be introduced in detail later in this chapter. For systems involving fluid and solid particles, LBE models based on the microscale collision between fluid and solid particles were proposed, which take the properties and motion of the particles into consideration[114-116]. Models involving chemical reactions are also developed, including combustion[117] and many other kinds of reactions[118, 119].

3.2 The Lattice Boltzmann Equation

Throughout the evolution of the Lattice Boltzmann method, the fundamental component that has remained central to the model is the LB equation. Overcoming its initial deficiencies in stability and accuracy, significant advancements have been made by employing novel equilibrium distribution functions and collision operators, resulting in enhanced simplicity. Within this section, a concise overview of the two prevalent equations: the BGK formulation and the MRT formulation, will be provided.

3.2.1 The BGK LBE

In its most essential form, the LB equation can be written as

$$\frac{\partial f}{\partial t} + v \cdot \nabla f = \Omega \quad (3.1)$$

where f is the particle distribution function, and $f = f(x, v, t)$. v is the velocity of the particle, and Ω is the collision operator. In the BGK model, the collision operator can be written as

$$\Omega = -(f - f^{eq}) / \tau \quad (3.2)$$

where f^{eq} is the equilibrium distribution function, and τ is the relaxation time. By discretising the particle velocity into a set of lattice velocities in different directions, the BGK formulation can be obtained as:

$$\frac{\partial f_i}{\partial t} + e_i \cdot \nabla f_i = -\frac{f_i - f_i^{eq}}{\tau} \quad (3.3)$$

where f_i and f_i^{eq} means the discrete density distribution function and its equilibrium distribution function, and e_i stands for the discrete lattice velocities. i tells the number of directions, for a D2Q9 model (two dimensions and nine velocities), i equals 9.

Further integrated over a time interval δt , the evolution of the lattice over a single time step can be obtained, written as

$$f_i(x + e_i \delta t, t + \delta t) - f_i(x, t) = -\frac{1}{\tau} (f_i(x, t) - f_i^{eq}(x, t)) \quad (3.4)$$

For a D2Q9 model, the equilibrium distribution function is given by

$$f_i^{eq} = \omega_i \rho \left[1 + 3 \cdot \frac{e_i \cdot u^{eq}}{c^2} + \frac{9}{2} \cdot \frac{(e_i \cdot u^{eq})^2}{c^4} - \frac{3}{2} \cdot \frac{(u^{eq})^2}{c^2} \right] \quad (3.5)$$

3.2.2 The MRT LBE

In contrast to the BGK model, the MRT model has garnered recognition for its ability to uphold stability and accuracy in challenging scenarios, including flow systems under high Reynolds numbers and high-density ratios. This accomplishment stems from the incorporation of a multi-relaxation time operator within the scheme, which allows for individual tuning of relaxation times to enhance stability. Nevertheless, the increased complexity introduced by the MRT scheme necessitates a higher computational resource allocation under equivalent conditions.

To integrate the MRT collision operator, the evolution of the density distribution function is written as:

$$f_i(x + e_i \delta t, t + \delta t) = f_i(x, t) - \overline{\Lambda_{ij}} \left[f_j(x, t) - f_j^{eq}(x, t) \right] \quad (3.6)$$

where $\bar{\Lambda} = M^{-1}\Lambda M$ is the collision matrix, with Λ being the diagonal matrix, M is an orthogonal transformation matrix and M^{-1} is its inverse matrix. For the D2Q9 model, the matrix M is:

$$M = \begin{bmatrix} 1 & 1 & 1 & 1 & 1 & 1 & 1 & 1 & 1 \\ -4 & -1 & -1 & -1 & -1 & 2 & 2 & 2 & 2 \\ 4 & -2 & -2 & -2 & -2 & 1 & 1 & 1 & 1 \\ 0 & 1 & 0 & -1 & 0 & 1 & -1 & -1 & 1 \\ 0 & -2 & 0 & 2 & 0 & 1 & -1 & -1 & 1 \\ 0 & 0 & 1 & 0 & -1 & 1 & 1 & -1 & -1 \\ 0 & 0 & -2 & 0 & 2 & 1 & 1 & -1 & -1 \\ 0 & 1 & -1 & 1 & -1 & 0 & 0 & 0 & 0 \\ 0 & 0 & 0 & 0 & 0 & 1 & -1 & 1 & -1 \end{bmatrix} \quad (3.7)$$

The density distribution function f_i and its equilibrium distribution function f_j^{eq} can be projected onto the moment space with the help of the transformation matrix. They can be obtained as:

$$m = Mf = (\rho, e, \zeta, j_x, q_x, j_y, q_y, p_{xx}, p_{xy})^T \quad (3.8)$$

$$m^{eq} = Mf^{eq} = (\rho, e^{eq}, \zeta^{eq}, j_x, q_x^{eq}, j_y, q_y^{eq}, p_{xx}^{eq}, p_{xy}^{eq})^T \quad (3.9)$$

For a detailed definition of the parameters listed above, one can refer to the reference[120, 121].

The multiple relaxation times are realised in the diagonal matrix Λ , which is given as:

$$\Lambda = \text{diag}(\tau_\rho^{-1}, \tau_e^{-1}, \tau_\zeta^{-1}, \tau_{j_x}^{-1}, \tau_{q_x}^{-1}, \tau_{j_y}^{-1}, \tau_{q_y}^{-1}, \tau_v^{-1}, \tau_v^{-1}) \quad (3.10)$$

And the collision process can be carried out in the moment space by multiplying through the transformation matrix:

$$m^* = m - \Lambda(m - m^{eq}) \quad (3.11)$$

while the streaming process is given as:

$$f_i(x + e_i \delta t, t + \delta t) = f_i^*(x, t) = M^{-1} m^* \quad (3.12)$$

3.3 Boundary Conditions

One notable advantage of the Lattice Boltzmann method is its straightforward treatment of boundary conditions. However, despite its simplicity, boundary conditions play a crucial role in accurately addressing heat and mass transfer problems. The precision of the boundary treatment directly impacts the overall accuracy and stability of the model. This section aims to introduce several commonly employed boundary conditions.

The first category of boundary conditions is the heuristic scheme, which is derived from the macroscopic characteristics of the boundary. These characteristics may include periodicity, symmetry, and flow conditions such as fully developed flow. One representative boundary condition in this category is the bounce-back boundary scheme, including the standard bounce-back scheme[122], the modified bounce-back scheme[123] and the halfway bounce-back scheme[124]. As illustrated in Fig. 3-2, the particles that collide with the boundary nodes undergo a bounce-back process, returning to their original positions while retaining the same level of momentum. This straightforward boundary treatment approach simplifies the overall process, requiring no additional steps once the solid boundaries have been identified. In comparison to the standard bounce-back scheme, which exhibits first-order accuracy, the halfway bounce-back scheme achieves second-order accuracy.



Fig. 3-2 Schematic of (a) standard bounce-back scheme and (b) half-way bounce-back scheme

The second category is the kinetic scheme, which directly solves the distribution function on boundary nodes based on the macroscale parameters on the boundaries. Some most representative schemes include the Nobel scheme[125], the non-equilibrium bounce-back scheme[126], the counter-slip velocity scheme[127] and the mass modified scheme[128]. Those models can strictly satisfy the boundary conditions, and good accuracy and stability can be achieved. However, their computation costly nature made it inconvenient for complex boundaries, thus their applications are limited.

The third category is the extrapolation scheme. The first extrapolation scheme was proposed by Chen et al.[129] in 1996. Later in 2002, Guo et al.[130] proposed another model based on the work of Chen et al., namely the non-equilibrium extrapolation scheme. The idea of this scheme comes from traditional CFD methods, such as the finite-difference method. Not only do those schemes have second-order accuracy, but they are also easy to use and have good stability.

The above-mentioned boundary condition treatment methods are mainly for flow systems with straight boundaries, while for those with complex boundaries, some schemes were also proposed[131-133]. An example was later provided in Chapter 5 of this thesis.

3.4 The multi-component multiphase models

Multi-component multiphase (MCMP) models encompass computational simulations designed to understand the dynamics of intricate fluid systems that involve multiple phases (such as liquid, gas, and solid) and multiple components (such as diverse chemical species) within a specific environment. These models employ mathematical equations to depict the behaviour of each phase and component, enabling real-time simulations of their interactions. The outcomes derived from these simulations offer valuable insights into fluid behaviour, transport phenomena, and thermodynamics within multiphase multi-component systems. Such models find extensive application in diverse industries, including oil and gas, chemical processing, power generation, and numerous others. Popular models, such as the volume of fluid (VOF)[134] method and level set[135] method are famous for their abilities in interface tracking, but they also require the interface reconstruction step or interface reinitialization step, which could be non-physical or very complex for programming[136]. Moreover, when dealing with cases that involve surface tension and complex boundaries, those methods could suffer from numerical instability[137]. Due to the microscopic nature and mesoscopic characteristics of the LB model, it shows great potential for solving the MCMP problems. Before the introduction of LB equation, people have carried out such attempts in the era of LGA[138]. Since then, exploration has always been attracting the attention of researchers, and many models have been established. The most representative models are the colour-gradient model, the pseudopotential model, the free-energy model and the phase-field model[139].

The first LBE model for a multinomial fluid system composed of different fluids is the colour gradient model proposed by Gunstensen et al.[140]. This model is based on the binary-phase model raised by Rothman and Keller, namely RK-LGA model[138]. In the colour gradient model of multi-component multiphase simulations, distinct fluids belonging

to different phases are visually represented using different colours. The interaction between these fluids is achieved by incorporating colour gradients, which inform the motion of fluid particles and simulate the mixing and separation processes. This model aligns with the Laplace law and has proven effective in investigating complex phenomena such as spinodal phase separation and multiphase flow in porous media. However, certain limitations exist within this model. The anisotropic nature of surface tension, influenced by interface orientations, poses challenges. Non-physical spurious currents may arise near interfaces. Additionally, incorporating thermodynamic effects can be challenging, and the process of recolouring introduces computational costs. These disadvantages impose notable restrictions on the further application of the colour gradient model.

The key idea of the colour gradient model is to reallocate the fluid particles according to the colour gradient, and the nature of force applied to the fluid particles at the interface is the difference between the average molecular forces on both sides of the interface. In 1993, Shan and Chen[141] proposed a model that uses pseudopotential to reflect such interaction, named the Pseudopotential model. The pseudopotential model offers a more direct representation of fluid-particle interactions. This model possesses several advantages, including simplicity, versatility, and the ability to automatically track phase separation without the need for specific interface capturing techniques. The pseudopotential model can be further categorised into two types: the single component multiphase (SCMP) model and the multi-component multiphase model. By carefully selecting an appropriate equation of state (EOS) and incorporating suitable force terms, the accuracy of the pseudopotential model can be enhanced. The details of these improvements will be extensively discussed in the subsequent sections of this chapter.

Different from the colour gradient model and pseudopotential model, which are based on the phenomenon observed from the interface between different phases, Swift et al.[142,

143] proposed an LBE model from the theory of free energy of the multi-component multiphase fluid system, which is in consistence with the theory of thermodynamics. The fundamental idea of this model is to construct the equilibrium distribution function according to the function of free energy and keep the total energy of the system consistent by the introduction of a thermodynamic pressure tensor for non-ideal fluid. However, this idea also exposed this model to the problem of Galilean invariance as the term introduced when modifying the equilibrium distribution function is non-Navier-Stokes[144]. Also, the velocity matrix in this term is second order, while from a mesoscale aspect, the term works on the momentum which is first order. Thus, this model requires further validation before being brought to vast application.

The phase field model is proposed by He et al.[145] in 1999. This model uses the Cahn-Hilliard equation[146] to capture the interface between different phases, which is based on the phase field theory. An LB equation is applied to solve the first-order parameters that obey the phase field theory, and the phases and the interface between them are represented by the order parameter integrated from the corresponding distribution function. Due to its interface orientated nature, this model can solve problems with large density ratios with ease, while costing extra computational resources.

This research adopts the pseudopotential model for the numerical simulation on droplets. As the research involves elements like phase change and surface tension, the pseudopotential model shows great simplicity here for its ability to track the interface automatically. Also, the model has been constantly developing over the decades, and many successful applications have proven the model mature.

However, the pseudopotential model still suffers from some limitations. The pseudopotential model doesn't strictly satisfy thermodynamics consistency[147], although

researchers have made some effort to make the coexistence density close to the thermodynamic results[148, 149]. The boundary refinement technique cannot be applied to this model as it doesn't require interface tracking, thus the efficiency of this model can hardly be improved when solving problems with complex boundaries[150]. Also, the density is non-discrete across tens of lattices, which makes the scheme not exclusively immiscible and cannot create sharp interfaces.[151, 152].

3.4.1 Equation of State

The pseudopotential model offers the advantage of accommodating different Equations of State (EOS) within the same framework. This flexibility allows for the representation of multiple phases coexisting at different densities under a single temperature. The EOS provides a mathematical relationship between pressure, temperature, and density for a given substance or mixture of substances. In scenarios where the details of the EOS are not crucial, such as immiscible two-phase flow, the colour gradient model and phase field model are commonly employed. Conversely, the pseudopotential model and free energy model are utilised to investigate problems where multiphase fluids are described by a single multiphase EOS, and phase separation and transition occur naturally based on the characteristics of the EOS[153]. Thus, understanding the effect of different EOSs is of great importance in those models regarding accuracy.

The most famous EOSs are:

The van de Waals (vdW) EOS, which is the earliest and simplest EOS in thermodynamics:

$$p = \frac{\rho RT}{1 - b\rho} - a\rho^2 \quad (3.13)$$

The Redlich-Kwong (RK) EOS:

$$p = \frac{\rho RT}{1-b\rho} - \frac{a\rho^2}{\sqrt{T}(1+b\rho)} \quad (3.14)$$

The Redlich-Kwong-Soave (RKS) EOS:

$$p = \frac{\rho RT}{1-b\rho} - \frac{a\alpha(T)\rho^2}{1+b\rho} \quad (3.15)$$

where $\alpha(T) = \left[1 + (0.48 + 1.574\omega - 0.176\omega^2) \left(1 - \sqrt{\frac{T}{T_c}} \right) \right]^2$.

The Peng-Robinson (PR) EOS:

$$p = \frac{\rho RT}{1-b\rho} - \frac{a\rho^2\alpha(T)}{1+2b\rho-b^2\rho^2} \quad (3.16)$$

where $\alpha(T) = \left[1 + (0.37464 + 1.54226\omega - 0.26992\omega^2) \left(1 - \sqrt{\frac{T}{T_c}} \right) \right]^2$.

And the Carnahan-Starling (CS) EOS:

$$p = \rho RT \frac{1+b\rho/4+(b\rho/4)^2-(b\rho/4)^3}{(1-b\rho/4)^3} - a\rho^2 \quad (3.17)$$

In the above stated EOSs, a, b are adjustable coefficients that affect the critical temperature and pressure of the substances, and ω is the acentric factor.

A lot of work has been done to study the relationship between the choice of EOS and the performance of simulations[153, 154]. Despite its historical significance, the van der Waals EOS has demonstrated limitations in accurately predicting results in multiphase multi-component flow simulations. However, alternative EOS formulations, such as the P-R EOS and the C-S EOS, have been developed based on the van der Waals EOS and offer improved

performance in these simulations. Particularly, the P-R EOS exhibits relatively higher accuracy for substances like water and ammonia, while the C-S EOS is capable of handling a broader temperature range. The P-R EOS is capable of simulating cases with the density ratios exceeding 2000, followed by the C-S EOS. It is important to note that an increased density ratio corresponds to a higher magnitude of spurious currents. In terms of temperature range coverage, the P-R EOS maintains its accuracy over the widest range, followed by the C-S EOS and the R-K EOS.

3.4.2 The force schemes

The incorporation of force terms holds significant importance in the MCMP models, given the presence of various forces arising from different components and external influences. In this model, it is crucial to consider the interaction forces within the fluid, which can be categorised as attractive and repulsive forces. Additionally, if the system involves solids, the interaction forces between the fluid and solid must also be taken into account, which will be discussed in detail in the subsequent section. Furthermore, external forces, such as gravity, need to be appropriately accounted for. The method of incorporating force terms has garnered considerable attention due to its pivotal role in enhancing the accuracy of the model. Generally, the methods of incorporating the force term can be divided into three categories: the velocity shifting method[141], the discrete force method[155, 156] and the exact difference method[157].

The velocity shifting method was proposed with the Shan-Chen (S-C) model. The force term was incorporated when calculating the equilibrium distribution function, by replacing the velocity in the equilibrium with

$$u^{eq} = u + \frac{\tau F}{\rho} \delta t \quad (3.18)$$

where F is the sum of the body forces. The overall fluid velocity is calculated by averaging the momentum before and after the collision step[158], given by

$$\rho U = \rho u + \frac{\delta t}{2} F \quad (3.19)$$

For the discrete force method and the exact difference method, the LB equation is written in a new form:

$$f_i(x + e_i \delta t, t + \delta t) - f_i(x, t) = -\frac{1}{\tau} (f_i(x, t) - f_i^{eq}(x, t)) + \Delta f_i(x, t) \quad (3.20)$$

where $\Delta f_i(x, t)$ is the body force term. In the discrete force method, the term stands for the discrete form of the force. Several different forms were proposed by researchers, for example that proposed by Guo et al.[159]:

$$\Delta f_i(x, t) = \left(1 - \frac{1}{2\tau}\right) \omega_i \left[\frac{e_i \cdot U}{c_s^2} + \frac{(e_i \cdot U)}{c_s^4} e_i \right] \cdot F \quad (3.21)$$

with U being the overall fluid velocity. In the discrete force method, the equilibrium force is the same as the overall fluid velocity, with equals to that in the velocity shift method.

The body force term in the exact difference method is given by

$$\Delta f_i(x, t) = f_i^{eq}(\rho(x, t), u + \Delta u) - f_i^{eq}(\rho(x, t), u) \quad (3.22)$$

In this method, Δu stands for the velocity change due to the body force and it equals to

$\frac{F \delta t}{\rho}$. The overall fluid velocity is the same as above. In the work of Gong and Cheng[160],

the different methods were compared. It was found that in both the discrete velocity method

and the exact difference method, the saturated densities of different phases are independent of the relaxation time, while the velocity shift model shows a different result, which is unphysical. Moreover, the exact difference method gives a more accurate result than the discrete velocity method.

3.4.3 The contact angle treatment

Wetting phenomena occur when there is an interaction between the liquid and solid phases, and in the case of droplets, the contact angle serves as an indicator of surface wettability, which influences the droplet's behaviour to a certain extent. In order to incorporate wetting phenomena into the LB model, numerous researchers have dedicated their efforts, leading to the development of various models. These models can be broadly categorised into density-based models and pseudopotential-based models. These different approaches aim to capture and simulate the complex dynamics of wetting within the LB framework.

The first model was proposed by Martys and Chen in 1996[161], which is a density-based model. Later in 2002, Kang et al.[162] extended this model and made it suit the D2Q9 model. The general form of the density-based model is written as:

$$F = -G_w \rho(x) \sum_i \omega_i s(x + e_i \delta t) e_i \quad (3.23)$$

The pseudopotential-based model was first proposed by Raiskinmäki et al.[163] in 2000. It replaced the pre-sum factor with the pseudopotential, and its general form can be written as

$$F = -G_w \psi(x) \sum_i \omega_i s(x + e_i \delta t) e_i \quad (3.24)$$

In the above formulas, G_w is the adsorption parameter for adjusting the value of the contact angle, and $s(x + e_i \delta t)$ functions as a probe which tells whether the adjusting node is fluid or solid. Most of the later models proposed were improvements and modifications on the pseudopotential-based model. In 2006, Benzi et al.[164] introduced a parameter $\psi(\rho_w)$ to take the pseudopotential of the solid wall into consideration, and the range of contact angles the model can simulate was enlarged compared to the previous. Later, other researchers[165, 166] also further improved the model on the aspect of the model's stability and the range of density ratios it can simulate effectively.

However, contact angle treatment models still face challenges. The interaction force on the triple-phase contact line affects the stability of the LB model and could result in false maximum and minimum densities deviating from the equilibrium densities[166]. Moreover, large spurious flows can occur around the contact line, and more effort is required to solve those problems.

As the multiphase multi-component LB models are constantly developing, they have been widely welcomed and applied to many industry fields. Some of the most representative applications lie in fuel cells and batteries[167-171], droplets[172-175], boiling[176, 177], evaporation[178-180], and energy storage with phase change materials[181-185]. However, there are still some limitations with the pseudopotential model, including thermodynamic inconsistency, spurious currents, surface tension accuracy, interface thickness, etc.[139] It's certain however, with the growing application of this model, more efforts will be devoted to refining the model, and its accuracy and stability can be further improved.

3.5 Numerical model used in this thesis

This research adopts the pseudopotential multi-component multiphase lattice Boltzmann method for its advantages such as simplicity, versatility, and clear physical meanings. Particularly, it can track the liquid-air interface automatically by incorporating intermolecular-level interactions[186]. Especially in cases where the liquid is not surrendered by just air but by a mixture of non-condensable gas and vapour, as the saturated liquid-saturated vapour interface does not have a sharp interface, but a finite thickness[187]. Furthermore, the contact angle doesn't need to be assumed constant, but adjustable by tuning the solid-liquid interaction force. LBM's intermolecular nature and mesoscopic scale make it more suitable to simulate multicomponent multiphase flows, and the ability of parallel computing and easy boundary treatment give it even more advantages. The numerical model adopted is based on the Gong-Cheng model[160] and the Shan-Chen model[141]. The model contains two components: water and non-condensable gas, with the phase of the water component changing between liquid and vapour. The BGK collision operator is adopted as its simpler form allows a more flexible boundary treatment.

3.5.1 The pseudopotential multi-component multiphase Lattice Boltzmann model

The lattice Boltzmann equation for momentum is listed below, which contains collision and streaming steps[188]:

$$f_{\sigma,i}(x + e_i \delta t, t + \delta t) - f_{\sigma,i}(x, t) = -\frac{1}{\tau_\sigma} (f_{\sigma,i}(x, t) - f_{\sigma,i}^{\text{eq}}(x, t)) \quad (3.25)$$

where τ_σ is the dimensionless collision relaxation time of the σ th component, and it's determined by the kinetic viscosity of the fluid:

$$v_\sigma = \frac{1}{3} c^2 (\tau_{\sigma,f} - \frac{1}{2}) \delta t \quad (3.26)$$

In this system, there are two components, respectively water (either in the vapour phase or liquid phase) and non-condensable gas. $f_{\sigma,i}(x,t)$ and $f_{\sigma,i}^{eq}(x,t)$ are the distribution and equilibrium distribution functions of the σ th component with the velocity e_i at lattice x and time t , respectively.

e_i is the lattice velocity vector and i stands for the lattice velocity direction. For the D2Q9 model, there are nine directions, so i ranges from 0 to 8. The discrete velocity for each direction is:

$$e_i = \begin{cases} (0,0) & i = 0 \\ c \left(\cos \frac{(i-1)\pi}{2}, \sin \frac{(i-1)\pi}{2} \right) & i = 1, \dots, 4 \\ \sqrt{2}c \left(\cos \frac{(2i-9)\pi}{4}, \sin \frac{(2i-9)\pi}{4} \right) & i = 5, \dots, 8 \end{cases} \quad (3.27)$$

where c is the reference lattice velocity.

Corresponding to the D2Q9 model, the momentum equilibrium distribution function is incorporated as[189]:

$$f_{\sigma,i}^{eq} = \omega_i \rho_\sigma \left[1 + 3 \frac{e_i \cdot u_\sigma}{c^2} + \frac{9}{2} \frac{(e_i \cdot u_\sigma)^2}{c^4} - \frac{3}{2} \frac{(u_\sigma)^2}{c^2} \right] \quad (3.28)$$

where ω_i is the weight coefficients, equalling to $4/9$ for $i = 0$, $1/9$ for $i = 1 \sim 4$, and $1/36$ for $i = 5 \sim 8$.

The density and velocity of each component can be calculated as:

$$\rho_\sigma(x,t) = \sum_i f_{\sigma,i}(x,t) \quad (3.29)$$

$$u_{\sigma}(x,t) = \frac{\sum_{\sigma} 1/\tau_{\sigma} \sum_i e_i f_{\sigma,i}(x,t)}{\sum_{\sigma} 1/\tau_{\sigma} \sum_i f_{\sigma,i}(x,t)} + \frac{F_{\sigma}(x,t)}{\sum_{\sigma} 1/\tau_{\sigma} \sum_i f_{\sigma,i}(x,t)} \quad (3.30)$$

where $F_{\sigma}(x,t)$ is the sum of forces applying to the σ th component at the location x and at time t . The real velocity can be acquired by averaging the velocity before and after δt , incorporated as[190]:

$$U_{\sigma}(x,t) = \frac{\sum_i e_i f_{\sigma,i}(x,t)}{\rho_{\sigma}(x,t)} + \frac{\delta t F_{\sigma}(x,t)}{2\rho_{\sigma}(x,t)} \quad (3.31)$$

And the total density and velocity are written as[141]:

$$\rho(x,t) = \sum_{\sigma} \rho_{\sigma}(x,t) \quad (3.32)$$

$$U(x,t) = \frac{1}{\rho(x,t)} \sum_{\sigma} \rho_{\sigma}(x,t) U_{\sigma}(x,t) \quad (3.33)$$

Within this simulation, the application of forces on a fluid node encompasses four distinct considerations: the attractive force between components of the same nature, the repulsive force between different components, the interaction force between fluid components and the solid substrate, and the gravitational force. Although the thermophoretic force was acknowledged, its magnitude was deemed negligible in comparison to other forces and thus disregarded in this particular scenario. The calculation of interaction forces between fluid components adheres to Gong and Cheng's established methodology[160]:

$$F_{\sigma,\sigma} = -\beta \psi_{\sigma}(x) \sum_{x'} G_{\sigma}(x,x') \psi_{\sigma}(x') + \frac{(1-\beta)}{2} \sum_{x'} G_{\sigma}(x,x') \psi_{\sigma}^2(x') \quad (3.34)$$

$$F_{\sigma,\sigma'} = -\psi'_{\sigma}(x) \sum_{x'} G_{\sigma'}(x,x') \psi'_{\sigma'}(x') \quad (3.35)$$

where σ' stands for the other component and x' stands for the neighbouring lattice. β is the tuneable weighting factor. And the solid-fluid interaction force is shown below:

$$F_{\sigma,s} = -(\psi_{\sigma}(x))^2 \sum_{x'} G_s(x, x') s(x') \quad (3.36)$$

for $s(x')$ the value varies from 0 to 1, depending on whether the lattice on x' represents fluid or solid. In Eq. (3.34), (3.35) and (3.36), the value of $G_{x,x',s}(x, x')$ is determined by the distance between the fluid nodes. The relationship between them is listed below[162]:

$$G_{\sigma,\sigma',s}(x') = \begin{cases} 2g_{\sigma,\sigma',s} & |x'-x|=1 \\ g_{\sigma,\sigma',s}/2 & |x'-x|=\sqrt{2} \\ 0 & otherwise \end{cases} \quad (3.37)$$

$\psi_{\sigma}(x)$ represents the effective mass of the σ_{th} component at node x . In the Shan-Chen model, the effective mass is given as[154]:

$$\psi_{\sigma}(x) = \sqrt{\frac{2(p_{\sigma} - c_s^2 \rho_{\sigma})}{c_0 g_{\sigma}}} \quad (3.38)$$

By comparing Eq. (3.38) with Eq. (3.34), it can be found that the force coefficient g_{σ} is cancelled out. Different from pseudo-potential $\psi_{\sigma}(x)$, $\psi'_{\sigma}(x)$ is chosen as $\psi'_{\sigma}(x) = \rho_{\sigma}(x)$ to enforce a proper component distribution.

Zhang et al.[191] compared different methods to calculate the gravity force. In this study, to ensure the conservation of the average mass velocity, the gravity force is given as:

$$F_{\sigma,g} = (\rho_{\sigma} - \rho_{avg})g \quad (3.39)$$

where ρ_{avg} is the average density of the computational domain.

3.5.2 The lattice Boltzmann model for thermal field with phase change term

The energy lattice Boltzmann equation used in this study is given as[192]:

$$g_{\sigma,i}(x + e_i \delta t, t + \delta t) - g_{\sigma,i}(x, t) = -\frac{1}{\tau_{\sigma,T}} (g_{\sigma,i}(x, t) - g_{\sigma,i}^{\text{eq}}(x, t)) + \delta t \omega_i \phi_\sigma \quad (3.40)$$

In Eq. (3.40), $\tau_{\sigma,T}$ is the temperature relaxation time, which is related to the thermal diffusivity:

$$\alpha_\sigma = \frac{1}{3} c^2 \left(\tau_{\sigma,T} - \frac{1}{2} \right) \delta t \quad (3.41)$$

$g_{\sigma,i}^{\text{eq}}(x, t)$ is the corresponding thermal equilibrium distribution function that can be obtained as:

$$g_{\sigma,i}^{\text{eq}}(x, t) = \omega_i T \left[1 + 3 \frac{e_i \cdot U}{c^2} + \frac{9}{2} \frac{(e_i \cdot U)^2}{c^4} - \frac{3}{2} \frac{(U)^2}{c^2} \right] \quad (3.42)$$

The phase change source term ϕ_σ is given below, as obtained by Zhang and Cheng[193]:

$$\phi_\sigma = T_\sigma \left[1 - \frac{1}{\rho_\sigma c_{v,\sigma}} \left(\frac{\partial p_\sigma}{\partial T_\sigma} \right)_{\rho_\sigma} \right] \nabla \cdot U_\sigma + \left[\frac{1}{\rho_\sigma c_{p,\sigma}} \nabla (\lambda_\sigma \nabla T_\sigma) - \nabla \cdot \left(\frac{\lambda_\sigma}{\rho_\sigma c_{p,\sigma}} \nabla T_\sigma \right) \right] \quad (3.43)$$

where λ is the thermal conductivity, c_v and c_p are the thermal specific heat at constant volume and pressure respectively. In this simulation, for the non-condensable gas component, the thermal specific heat is set to 1, so the first term in Eq. (3.43) equals to 0. For the macroscale temperature, the temperature for each component can be obtained as below:

$$T_\sigma(x, t) = \sum_i g_{\sigma,i}(x, t) \quad (3.44)$$

and the temperature for the mixture is

$$T(x,t) = \frac{1}{\rho(x,t)c_v} \sum_{\sigma} \rho_{\sigma}(x,t)c_{\sigma,v}T_{\sigma}(x,t) \quad (3.45)$$

3.4.3 The Equation of State

The P-R EOS is adopted in this simulation to couple the momentum with the thermal LB model. The equation is given as

$$p = \frac{\rho RT}{1-b\rho} - \frac{a\rho^2\varepsilon(T)}{1+2b\rho-b^2\rho^2} \quad (3.46)$$

where $a = \frac{0.457235R^2T_c^2}{p_c}$, $b = \frac{0.077796RT_c}{p_c}$ and

$\varepsilon(T) = \left[1 + (0.37464 + 1.54226\omega - 0.26992\omega^2) \left(1 - \sqrt{T/T_c} \right) \right]$, where the subscript c denotes critical state. ω is the acentric factor and is set to $\omega = 0.344$, and a, b, R are set to $3/49$, $2/21$ and 1 , respectively[160]. In this case, β in Eq. (3.34) equals to 1.16 for the water component. To improve the numerical stability at larger density ratios, Hu et al.[194] introduced a coefficient k to modify the EOS, so the model can maintain stability when simulating cases with larger density ratios. The EOS after the modification is written as

$$p = k \left(\frac{\rho RT}{1-b\rho} - \frac{a\rho^2\varepsilon(T)}{1+2b\rho-b^2\rho^2} \right) \quad (3.47)$$

where $0 < k < 1$.

For the non-condensable gas component, the ideal gas equation is used, as listed below:

$$p = \rho RT \quad (3.48)$$

Correspondingly, β in Eq. (3.34) equals 1 .

Chapter 4. Investigation on the droplet evaporation process on localised heated substrates with different wettability

The Marangoni effect, arising from the surface tension gradient within the droplet interface, plays a crucial role in the evaporation process of droplets. In this chapter, a comprehensive numerical investigation is launched to elaborate on the effect of Marangoni flow on droplet evaporation. Localised heating is employed to introduce a more complex temperature distribution across the droplet surface. The obtained results indicate that an asymmetrical positioning of the heat source can lead to an asymmetric morphology of the droplet, particularly noticeable on superhydrophilic surfaces. Both the heat source position and the droplet's contact angle have a notable impact on the evaporation rate. When the droplet is placed on a smooth substrate, horizontal slipping occurs due to asymmetrical heating conditions. The slipping behaviour is influenced by both the positioning of the heat source and the wettability of the surface.

4.1 Introduction

The evaporation process of droplets is influenced by various factors, and among them, Marangoni flow assumes a crucial role in shaping the internal flow pattern of droplets, thereby impacting heat transfer and evaporation behaviour [195]. In recent years, scholars have dedicated their efforts to studying the relationship between the Marangoni effect and the droplet evaporation process. Hu and Larson[196, 197] investigated the impact of Marangoni flow on the well-known phenomenon of the "coffee-ring" effect. Their findings revealed that one of the key prerequisites for the formation of the "coffee-ring" effect is the suppression of Marangoni flow, while the presence of surfactant contamination effectively inhibits the occurrence of the Marangoni effect. Ljung and Lundström[198] employed numerical methods to examine the influence of boundary conditions on flow patterns both within and outside the droplet. Their investigations unveiled that the presence of the Marangoni effect leads to a significant increase in velocity within the droplet, reaching up to three orders of magnitude higher values. Savino and Fico[199] explored the effect of Marangoni flow on the evaporation process by employing silicone oils with varying viscosities and hydrocarbons. Their research suggests that Marangoni flow can induce a larger and more uniform surface temperature, ultimately leading to an increased rate of evaporation.

From the formula of the Marangoni number $Ma_T = -\frac{d\sigma}{dT} \frac{l\Delta T}{\eta\alpha}$, it's evident that a

temperature gradient induces the occurrence of Marangoni flow at the fluid interface.

Consequently, when a localised heating condition is applied to a droplet, the more intricate surface temperature gradient engenders a correspondingly complex flow pattern within the droplet. This, in turn, alters the heat transfer dynamics and subsequently impacts the rate of evaporation. However, most existing research in this domain primarily focuses on heating conditions involving heat plates or ambient heating, leaving a significant gap in the

understanding of localised heating effects on droplets. Furthermore, the experimental investigation of this topic faces substantial limitations due to the minute size of droplets. As a result, the present thesis adopts a numerical approach to explore the influence of localised heating on the evaporation process of droplets.

The Lattice Boltzmann method has garnered significant attention from researchers investigating droplet phenomena due to its advantages in terms of parallelism, boundary condition processing, and program implementation. Yan and Zu[200] employed LBM to simulate the behavior of liquid droplets on partially wetting surfaces with large liquid-gas density ratios. By combining Inamuro's[201] and Briant's[202] models, they studied the droplet falling onto a hydrophilic surface with hydrophobic strips. The obtained results demonstrated that the current LBM approach provides a reliable means of investigating fluidic control on heterogeneous surfaces and other wetting-related subjects. Taghilou and Rahimian et al.[203] utilised a model based on the Cahn-Hilliard diffuse interface theory to capture the liquid-gas interface, while employing a passive scalar model to simulate thermal effects. They observed that increasing the Prandtl number ratio between the droplet and its surroundings results in delayed thermal diffusion within the droplet, leading to a reduction in the droplet's average temperature. Guo and Cheng et al.[204] examined the effects of ambient humidity of air and wall temperatures on the evaporation of sessile droplets using the MCMP LBM model. The evaporation behaviour near the Leidenfrost temperature was studied, including the flow pattern and the heat flux. Sohrabi and Liu[205] provided a concise review of advancements in breaking the limitations imposed by density ratio and achievable temperature over the past decades. The relationship between temperature, reference relaxation time, density ratios, a reduced parameter for the equation of state and the interface thickness was outlined to help lift the limitations when dealing with cases at a lower temperature than the Leidenfrost point.

On the other hand, surface wettability plays a significant role in influencing droplet behaviour, encompassing effects on inner droplet flow patterns and evaporation rates. Takata et al.[206] conducted experiments on the evaporation of water droplets on plasma-irradiated hydrophilic surfaces. They measured the contact angle and observed that as the contact angle decreased, the evaporation time decreased, while the wetting limit and Leidenfrost temperatures increased. Droplet morphology during the evaporation process on superhydrophobic surfaces has also been researched by many researchers[207-209], and their unique behaviour is compared to that on a conventional surface. Sobac and Brutin[210] tested the evaporation of droplets with a wide range of contact angles and found that when the contact angle is small, the evaporation rate is predominantly influenced by the contact radius.

Within this chapter, a pseudo-potential multi-component multi-phase lattice Boltzmann method model is employed to investigate the evaporation of droplets under various localised heating conditions. The influence of substrate wettability on the evaporation process is also taken into account by examining the effect of the contact angle. The flow patterns and temperature distribution within the droplet are analysed, as well as the morphology of the droplet and its evaporation rate. Furthermore, particular attention is given to the phenomenon of droplet slipping induced by an asymmetric heating source.

4.2 Results and Discussion

4.2.1 Model Validation

To validate the numerical model employed, a simulation is conducted to investigate the evaporation process of a droplet on a superhydrophobic surface. The droplet's contact angle is set to approximately 150° , while the heat source is uniformly distributed on the substrate, as depicted in Fig. 4-1. The reduction in droplet volume and contact angle is quantitatively measured and subsequently compared to findings reported by Gibbons et al.[211] and theoretical outcomes derived from the Young-Laplace solution.

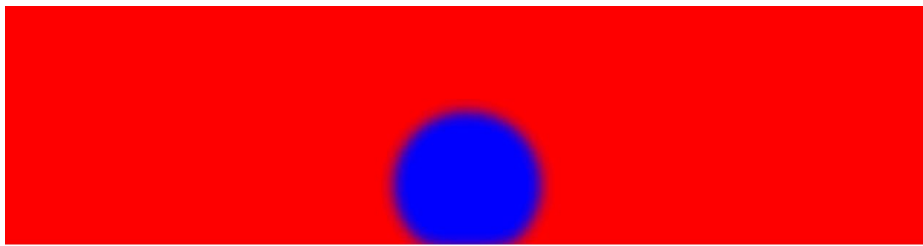


Fig. 4-1 Schematic of a droplet placed on a superhydrophobic surface. (CA = 150°)

Remarkably, the findings of this study exhibit a striking level of concurrence, with a maximum deviation of only 2.53% in droplet volume and 1.83% in contact angle when compared to Gibbons' experimental results. It is noteworthy that during the initial phase of evaporation, the droplet undergoes a shape transformation under the influence of heating. As temperature diffusion occurs within the droplet, intermolecular forces are modified, leading to a decrease in the contact angle. Throughout the major evaporation process, the deviation in the contact angle remains below 10%, suggesting a state of CCA in accordance with Dash and Garimella[212]. Furthermore, in the final stages of evaporation, a transition from the CCA model to the CCR model takes place. During this transition, the contact angle experiences a rapid reduction, while the volume curve exhibits a flattening trend. It is

important to emphasize that the droplet's morphology during these initial and final periods is characterized by instability and does not adequately represent the typical progression of the evaporation process. Therefore, these periods, which collectively account for approximately 15% of the entire evaporation process, have been excluded from the comparative analysis.

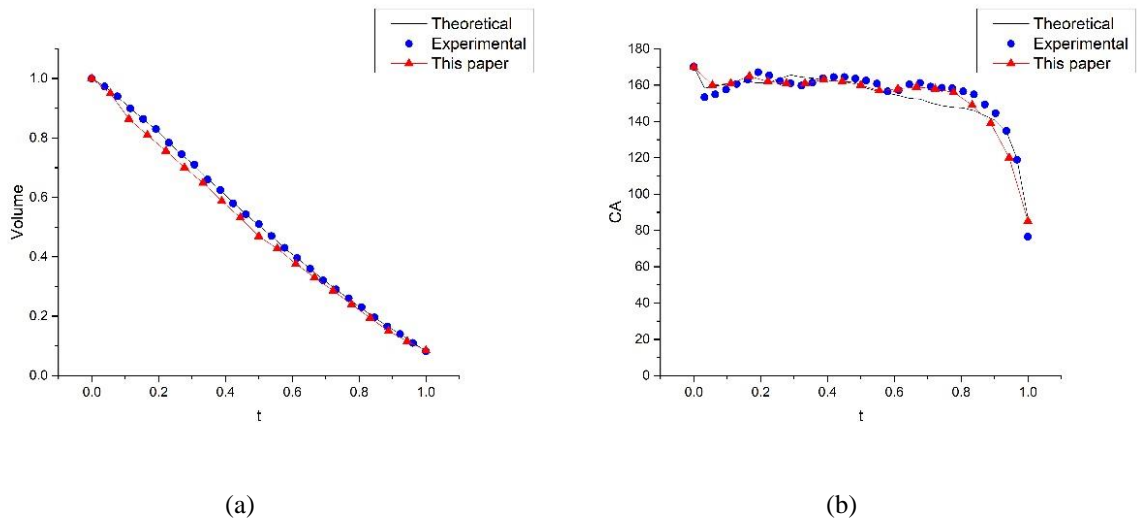


Fig. 4-2 Model verification results. (a) Comparison of the volume change throughout the evaporation process. (b) Comparison of the contact angle change throughout the evaporation process

4.2.2 Simulation of the standard droplet evaporation process

A simulation of the standard droplet evaporation process is also conducted to provide a reference for the localised heating study. In this simulation, a water droplet is positioned on substrates with varying contact angles: 30° , 60° and 90° . The heat source is uniformly distributed on the substrate at a constant higher temperature T_h . The initial ambient temperature is set as the saturated temperature T_{sat} , which is lower than the substrate temperature. The temperature settings are determined based on the work of Gong and Yan[177], with both T_h and T_{sat} calculated based on the critical temperature T_{cr} ; here, the saturated temperature is set at $T_{sat} = 0.86T_c$, and T_h is set at three different temperatures,

respectively $0.90T_c$, $0.91T_c$ and $0.92T_c$. The top and bottom boundaries are assigned as bounce-back boundaries, while the left and right boundaries are set as periodic boundaries.

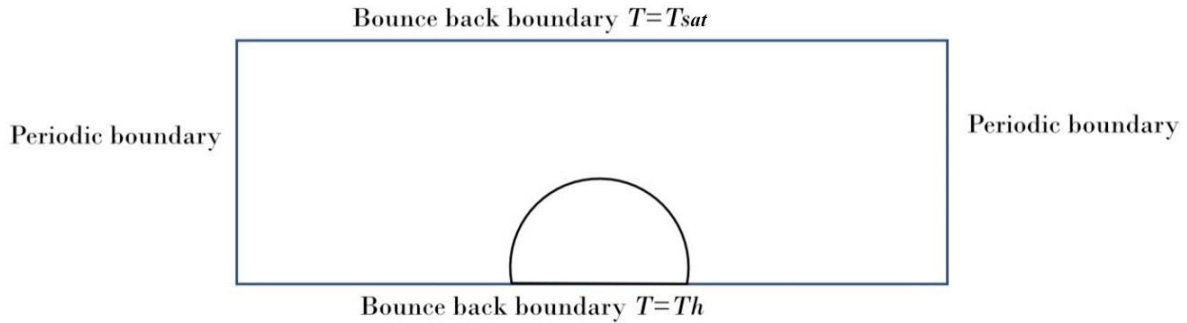


Fig. 4-3 Schematic of the simulation of the standard evaporation process

During the initial stage of evaporation, a noteworthy time delay is observed in the attainment of equilibrium temperature within the droplet. This delay arises from the disparity in heat capacity and density between the liquid and gas phases. Fig. 4-4 depicts the evolution of isotherms during this initial stage of the evaporation process. To ensure convergence and minimise errors, gravity is introduced after 40×10^3 timesteps, followed by the addition of the heat source after 80×10^3 timesteps. Data collection for this study commences from 80×10^3 timesteps onward.

The isotherms, both within the droplet and its surrounding region, exhibit a nearly horizontal distribution with a distinct hierarchical arrangement at the interface, as illustrated in Fig. 4-4. As the evaporation proceeds, both the interior and exterior isotherms gradually rise from the substrate, indicating the conduction of heat from the substrate towards the droplet. The difference in height between adjacent isotherms diminishes as the evaporation progresses.

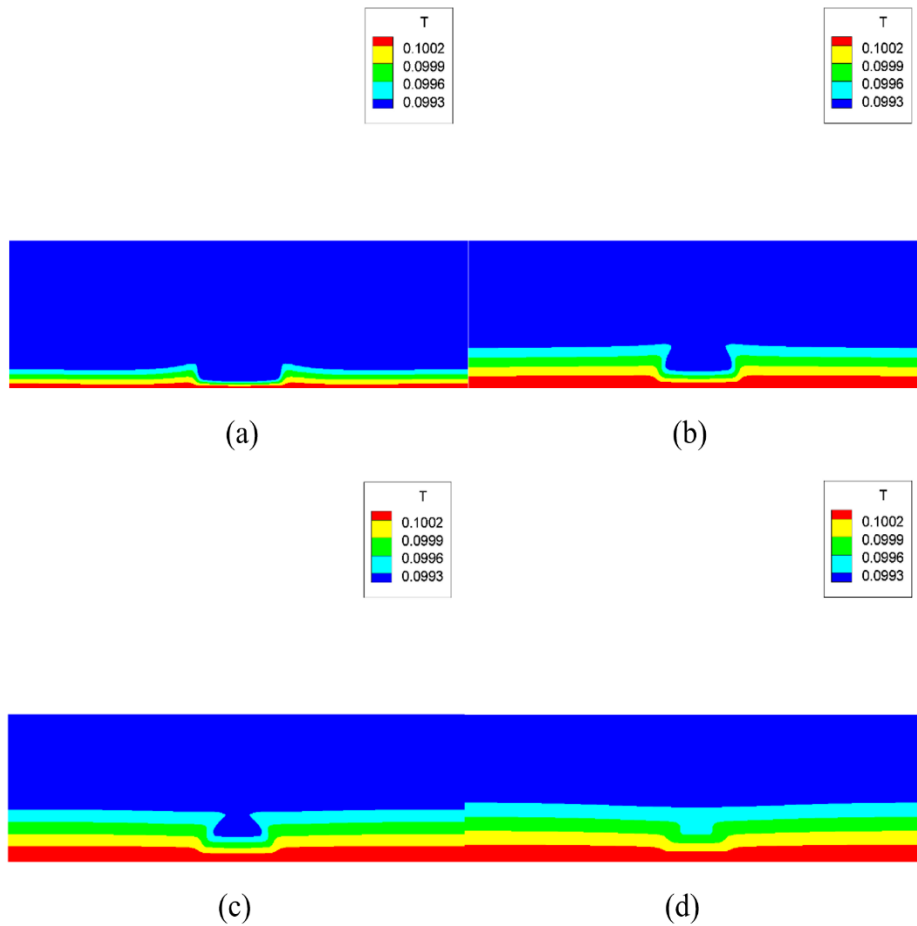
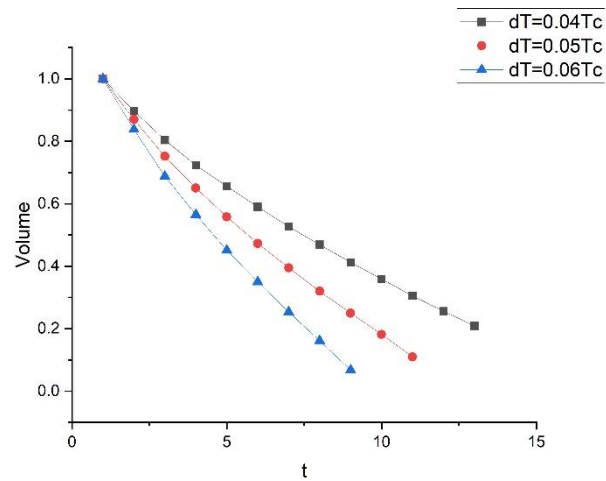
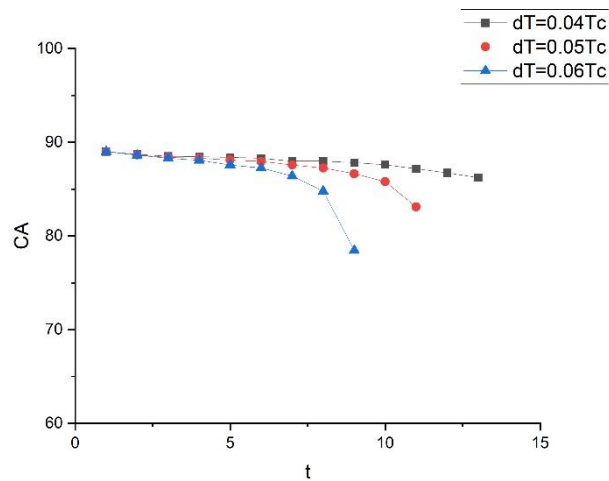


Fig. 4-5 illustrates the morphological changes of the droplet during the evaporation process, focusing on the variations in droplet volume and contact angle. Data points are recorded at intervals of 10×10^3 timesteps. The x-axis represents the timestep unit, while Fig. 4-5 (a) displays the ratio of droplet volume to the initial volume at the onset of heating on the y-axis. In Fig. 4-5 (b), the y-axis represents the contact angle in degrees as a function of evaporation time. Notably, in Fig. 4-5 (a), the trends exhibited by the droplet volume are consistent, except for variations in the rate of volume decrease, as the temperature remains below the Leidenfrost point. Furthermore, the curve depicting the volume reduction gradually flattens, indicating a decrease in contact area between the droplet and the substrate, as well as an increasing vapour concentration that hinders the evaporation. During the initial stage of

evaporation, the temperature increase within the droplet leads to a decrease in intermolecular forces and surface tension, resulting in a reduction in the contact angle. In the latter part of the evaporation process, as the evaporation mode transitions from the CCA model to the CCR model, the contact angle experiences a rapid decrease, ultimately leading to complete evaporation.



(a)



(b)

Fig. 4-5 Morphology of the droplet in the evaporation process under different superheat temperatures. (Contact angle = 90°, substrate heating) (a) the volume evolution to time. (b) the contact angle evolution to time.

4.2.3 Simulation of the droplet evaporation under localised heating

The Marangoni flow exerts a significant influence on the internal flow pattern of the droplet. The flow field, in turn, impacts heat transfer within the droplet, subsequently affecting

temperature distribution, droplet motion, morphology, and ultimately the evaporation rate. This portion of the study focuses on examining the impact of various localised heating conditions on evaporation behaviour. Additionally, different surface wettability is considered to assign distinct initial contact angles to the droplets. Fig. 4-6 presents the schematic diagram of the simulation setup employed in this study. The configuration consists of a droplet positioned on a substrate and surrounded by saturated vapour. The initial temperature of the entire simulated cavity is set to the saturated temperature $T_{sat} = 0.86T_c$, where T_c is the critical temperature derived from the equation of state. The top and bottom boundaries are assigned as bounce-back boundaries, and the temperature of the top boundary is maintained at T_{sat} , while the bottom boundary is divided into three distinct regions denoted as A, B, and C. The temperatures of regions A and C are set at T_{sat} , while the temperature of region B is set at T_h . To ensure a reasonable evaporation rate, computational efficiency, and avoidance of nuclear boiling phenomena, the heating temperature is carefully selected and set to $T_h = 0.92T_c$.

four different surface wettability conditions are considered, corresponding to major contact angles of 30° , 60° , 90° , and 120° during the CCA period of evaporation. The size of the heating area B is kept constant, while different positions are selected for the center point of the heating area. Specifically, when the contact angle is 90° , the heating area is set at 0.44 times the radius of the droplet while maintaining a fixed droplet volume. For simplicity, the position of the centre of the heating area is denoted by L_c , and the length of the heating area is represented by a dimensionless parameter 1. For instance, $L_c = 0$ indicates that the heating source is located at the centre of the droplet contact section, and when $L_c = 2$, the centre of the heating source is positioned at twice the length of the heating area from the droplet centre to the triple-phase contact point.

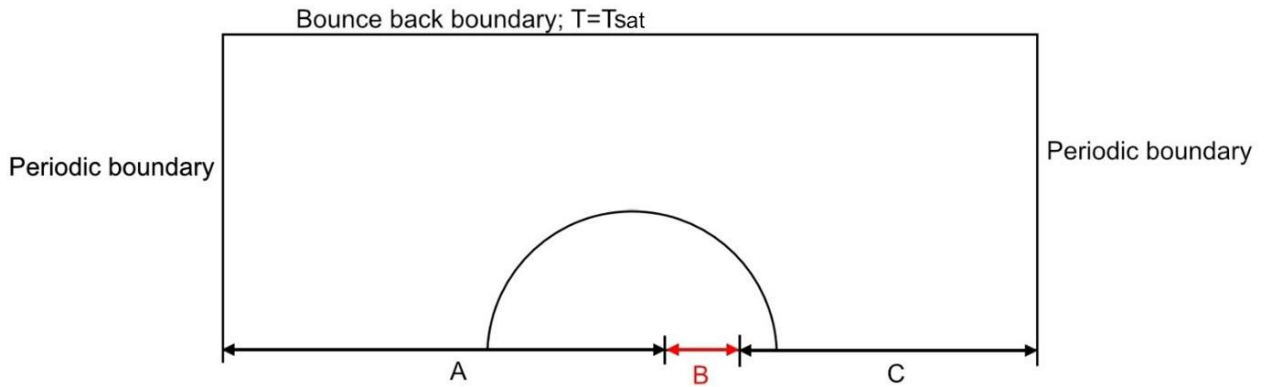
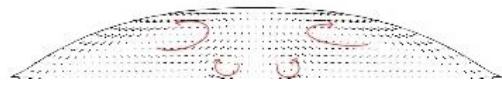


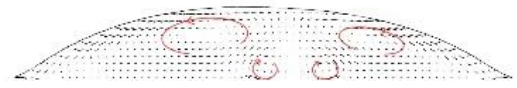
Fig. 4-6 Schematic of simulation of droplet evaporation under localised heating. (A and C: $T = T_h$; B: $T = T_h$).

Fig. 4-7 provides visual representations of the streamlines within droplets on substrates with varying wettability, corresponding to different values of L_c . Subfigures (a)-(d) present the streamlines in droplets with a contact angle of 30° degrees, subfigures (e)-(h), (i)-(l), and (m)-(o) display the streamlines for contact angles of 60° , 90° , and 120° , respectively. Values of L_c are chosen as 0, 0.5, 1 and 1.5 for contact angle from 30° to 90° . For the contact angle of 120° , due to limitations in liquid-solid contact size, three different values (0, 0.25, 0.75) are selected for L_c . The data at time step 100×10^3 is specifically chosen to ensure that the droplet evaporation is in a steady CCA mode. Upon observation, it becomes apparent that regardless of variations in contact angles and heating source positions, two vortices consistently form adjacent to the heat source. These vortices arise due to natural convection, which occurs as a result of temperature gradients both horizontally and vertically around the heat source. Furthermore, vortices can also be identified on the upper surface of the droplet, flanking both sides of the heat source. These flows can be attributed to the Marangoni effect. The Marangoni effect operates on the principle that surface tension decreases as temperature increases. The flow directions along the droplet interface are determined by the surface tension, moving from areas of lower surface tension towards those

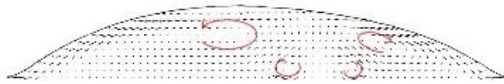
with higher surface tension. As the temperature above the heat source surpasses that of the surrounding regions, the flow is driven from the droplet surface positioned above the heating source towards the triple-phase contact point on either side. The flow pattern near the triple-phase contact point, influenced by capillary flow, moves from the liquid phase to the triple-phase contact line[213], counteracting the flow induced by the Marangoni effect. Upon comparison between the sizes of the upper and lower vortices, a noteworthy observation is that droplets with smaller contact angles exhibit a more prominent flow induced by the upper surface tension gradient. This finding substantiates the dominance of the Marangoni flow in terms of magnitude. Simultaneously, an examination of the lower flow field reveals that droplets with larger contact angles, under a constant heat source area, manifest vortices resulting from natural convection that occupy a larger region than the capillary flow. This observation implies that the influence of natural convection becomes more prominent for droplets with larger contact angles, leading to a greater extent of vortices in the lower flow field, surpassing the influence of capillary flow. This observation is attributed to the weakening of capillary flow for droplets with larger contact angles, as the ratio of droplet height to diameter (h/d ratio) increases. Another significant conclusion drawn from the study is that when asymmetrical localised heating conditions are applied, the droplet shape exhibits a propensity for asymmetry. This occurs due to the impact of the asymmetric heating condition on the evaporation rate distribution, particularly in the case of flatter droplets. In such scenarios, the spherical cap shape of the droplet is compromised as the capillary flow fails to adequately compensate for the mass loss within a given timeframe. As a result, the droplet assumes an asymmetric morphology. The asymmetry is more evident for droplets on superhydrophilic substrates, such as Fig 4-7 (c) and (d), and the hemisphere where the heat source is located shows a smaller average height than the opposite hemisphere.



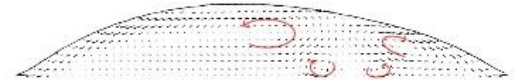
(a)



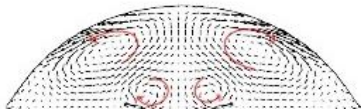
(b)



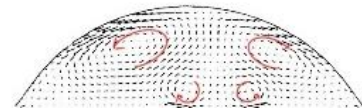
(c)



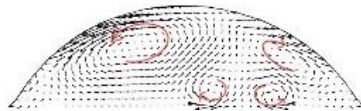
(d)



(e)



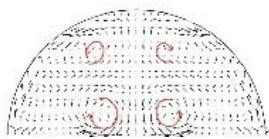
(f)



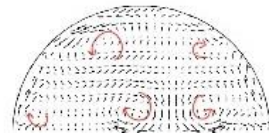
(g)



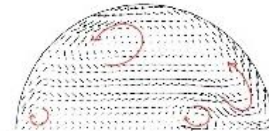
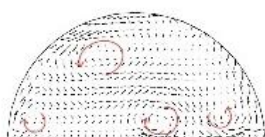
(h)



(i)



(j)



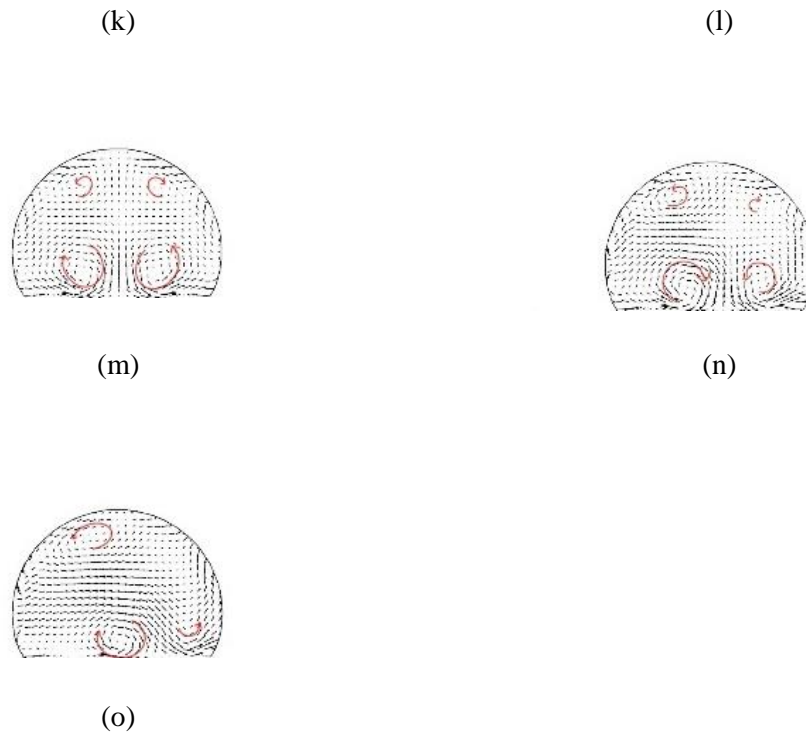
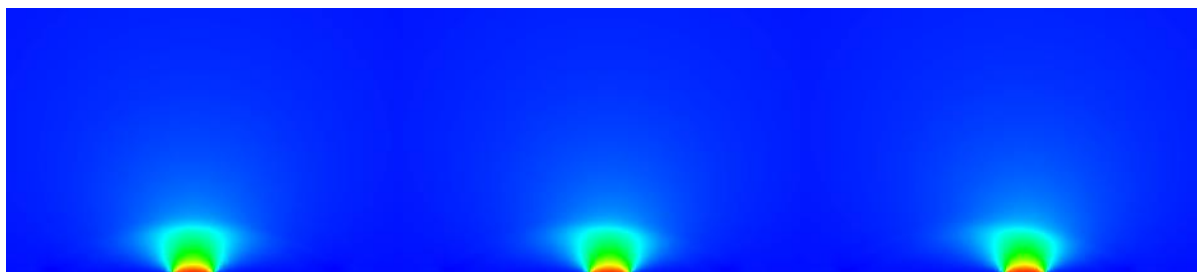


Fig. 4-7 Streamlines inside the droplet on substrates with different wettability under localised heating conditions. (a-d: contact angle = 30° , $L_c = 0, 0.5, 1, 1.5$; e-h: contact angle = 60° , $L_c = 0, 0.5, 1, 1.5$; i-l: contact angle = 90° , $L_c = 0, 0.5, 1, 1.5$; m-o: contact angle = 120° , $L_c = 0, 0.5, 1$)

As captured in the figure below is the temperature distribution of the droplet when localised heating is applied. The data is also captured at 100×10^3 timesteps after the heat distribution reaches a steady state. The contact angle and heat source location remain the same as the corresponding figures in Fig. 4-7. It is predictable that the temperature distribution within the droplet will move along with the movement of the heat source. Unlike the heating condition of a heat plate, where the entire bottom of the droplet is evenly heated, in this case, a significant portion of the droplet's bottom region remains at a relatively low temperature. This is primarily because the heat is mainly transferred upwards from the heat source. Consequently, the upper part of the droplet tends to exhibit a higher mean temperature compared to the bottom part. The highest temperature on the droplet surface is located directly above the heating source. Additionally, a noticeable temperature jump occurs at the droplet interface, attributable to the difference in thermal conductivity and heat

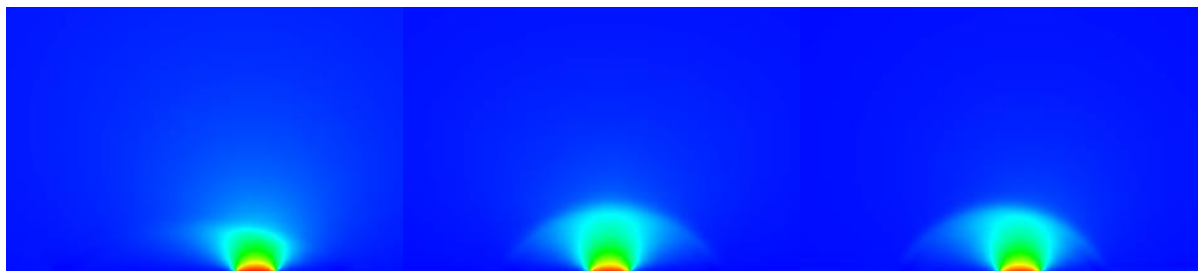
capacity between the two fluid phases. Furthermore, the influence of the Marangoni flow becomes apparent as the heated area on the droplet surface expands from directly above the heat source towards the triple-phase contact line, aligning with the direction of the Marangoni flow. This expansion of heat is more pronounced in droplets with larger contact angles, as the capillary flow, which counters the Marangoni flow, is weaker in such cases. Consequently, the Marangoni flow occupies a larger surface area before being counteracted by the capillary flow. A more detailed temperature distribution of the droplet is presented in Fig. 4-8.



(a)

(b)

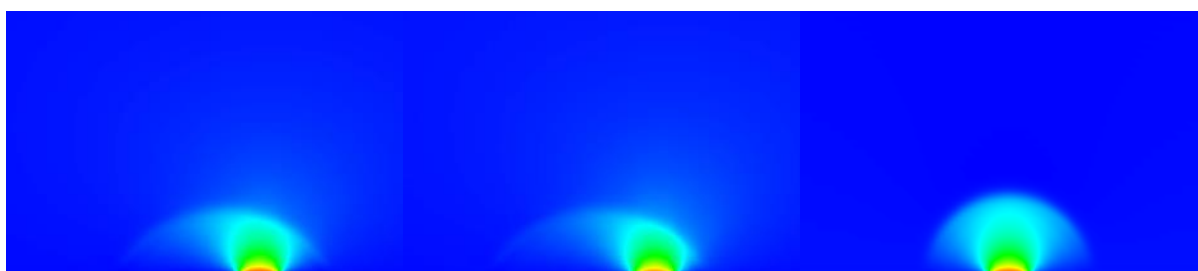
(c)



(d)

(e)

(f)



(g)

(h)

(i)

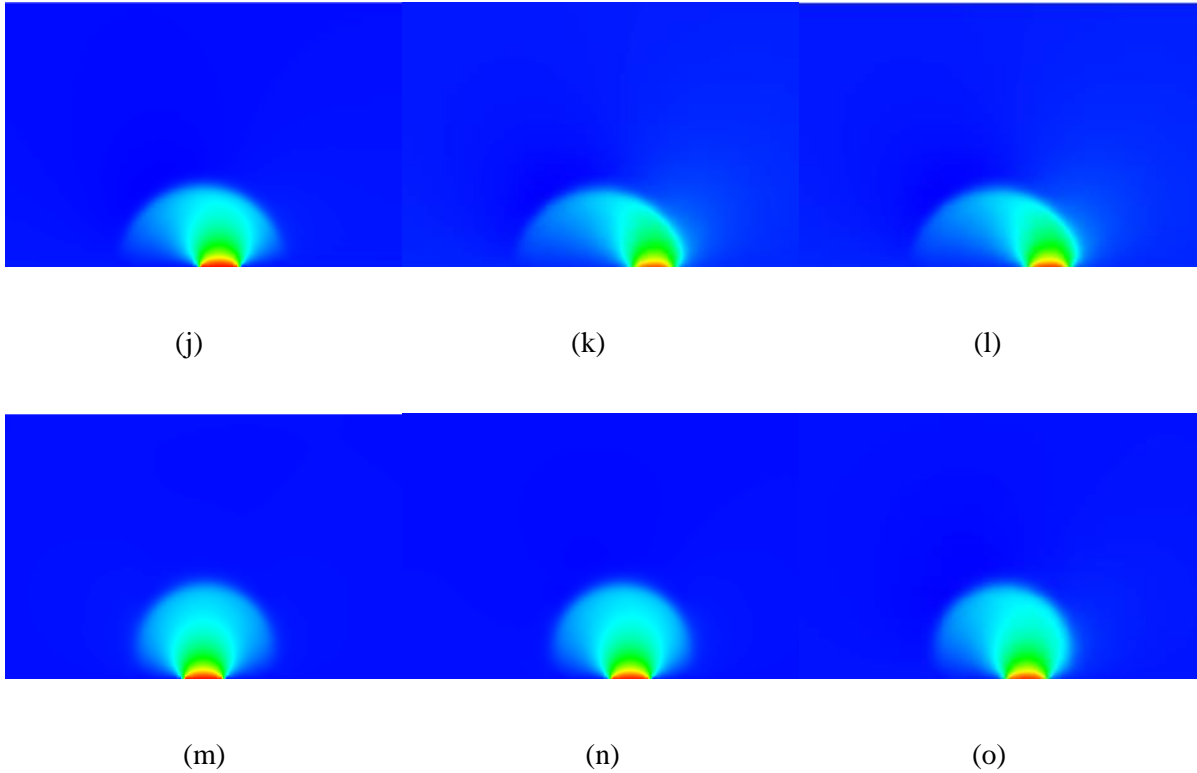


Fig. 4-8 Temperature distribution in the flow field of droplets with different contact angles under localised heating conditions. (a-d: contact angle = 30° ; $L_c = 0, 0.5, 1, 1.5$; e-h: contact angle = 60° ; $L_c = 0, 0.5, 1, 1.5$; i-l: contact angle = 90° ; $L_c = 0, 0.5, 1, 1.5$; m-o: contact angle = 120° ; $L_c = 0, 0.5, 1$)

Fig. 4-9 illustrates the variation in temperature along the droplet interface in response to changes in the heat source location. The droplet is positioned on a substrate with a contact angle of 90° , and four different heat source locations are examined, respectively $L_c = 0, 0.5, 1$ and 1.5 . The x-axis of the graph represents different positions along the droplet interface, with a value of 0.5 denoting the centre of the droplet surface and a value of 1.0 corresponding to the right triple-phase contact point. Temperature measurements are recorded at each lattice length unit along the droplet interface, and the average surface temperature is calculated by summing up the temperature data and dividing it by the total number of length units. The results demonstrate that as the heat source position is shifted, the temperature profile curve becomes asymmetric. The peak value of the maximum temperature moves from the centre towards the heat source direction. Additionally, an increase in the parameter leads to a higher

mean temperature of the droplet surface. This is attributed to the fact that the edge of the droplet is thinner compared to the centre, resulting in a decreased vertical distance between the heat source and the droplet interface. Consequently, the maximum temperature at the interface becomes higher.

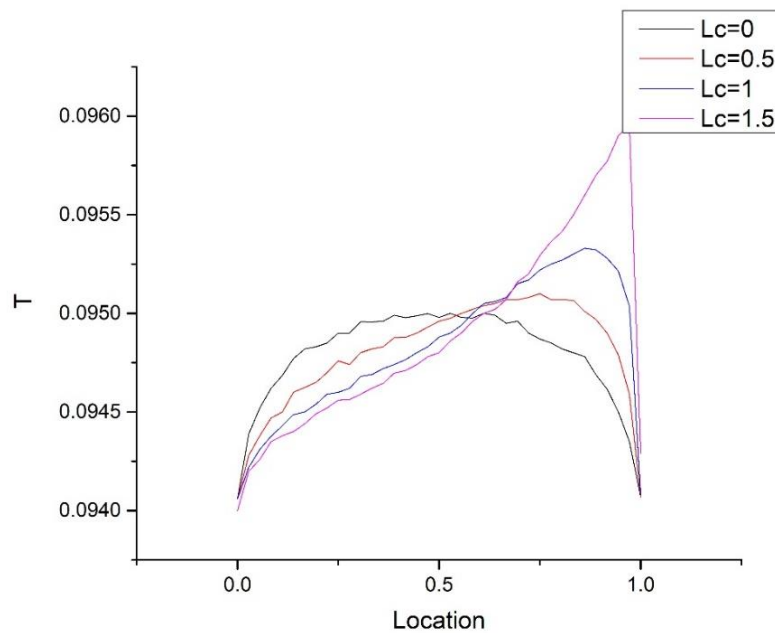
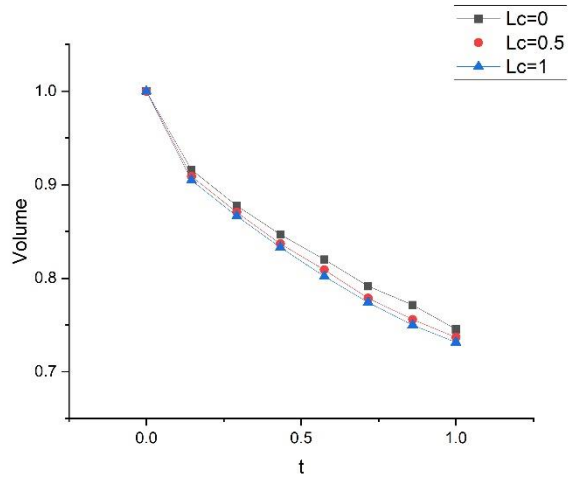
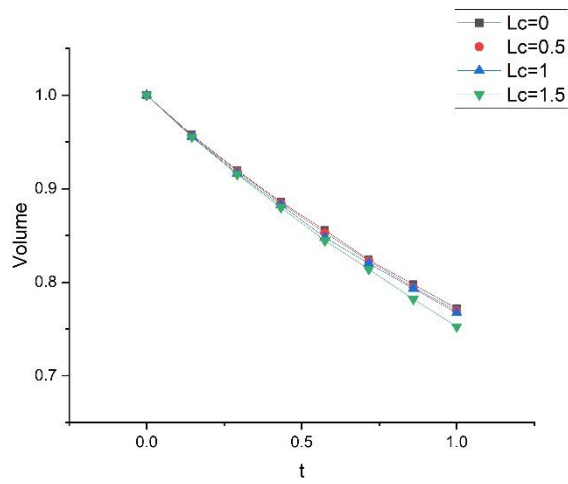


Fig. 4-9 Interface temperature profile for a droplet with contact angle = 90°

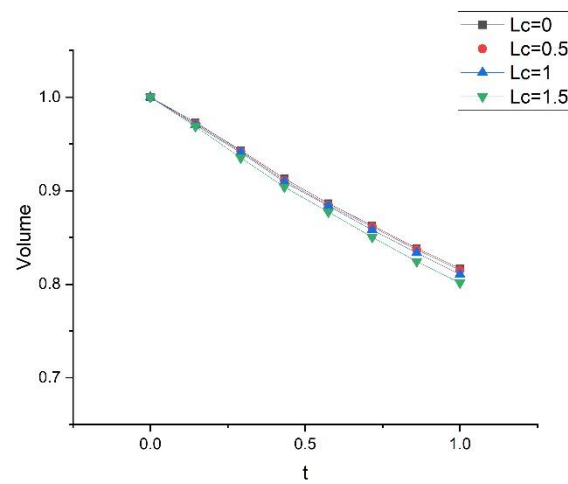
The role of droplet interface temperature in influencing the evaporation rate is supported by the findings presented in Fig. 4-10. The graph depicts the evolution of droplet volume over time for droplets subjected to different local heat sources on substrates with varying wettability. It should be noted that the case of a contact angle of 120° is excluded from consideration due to the limited contact area, and the case $L_c = 1.5$ of a contact angle of 30° is not taken into account because it results in an asymmetric droplet shape, making it challenging to calculate the droplet volume accurately. From the figure, it is evident that regardless of surface wettability, the evaporation rate of the droplet increases when the heat source is positioned closer to the droplet edge. This trend is more pronounced in cases with



(a)



(b)



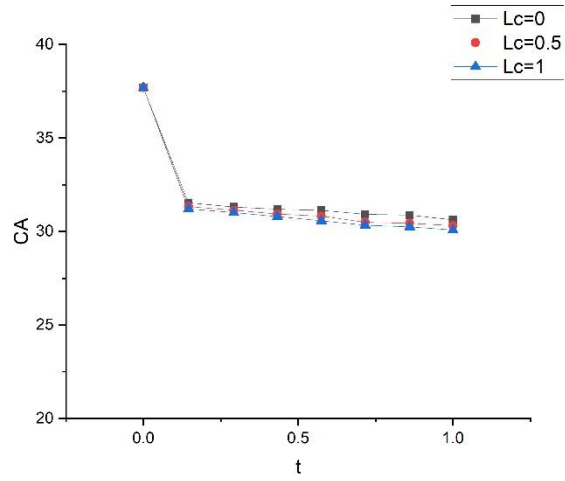
(c)

Fig. 4-10 Evolution of droplet volume under localised heating conditions. (a) contact angle = 30°; (b) contact angle = 60°; (c) contact angle = 90°

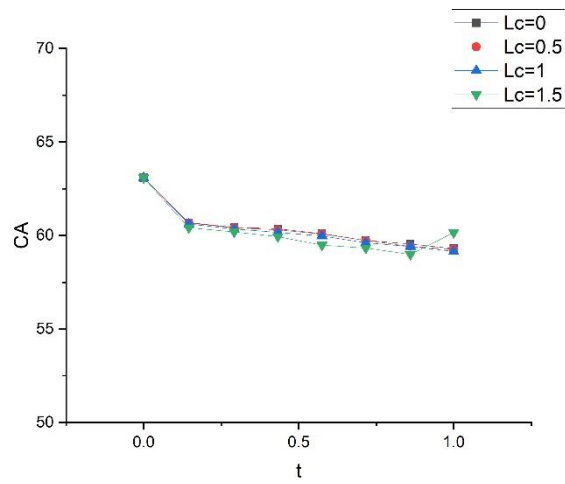
larger contact angles, where the heat source location has a more significant impact on the droplet surface temperature. Furthermore, droplets with smaller contact angles also exhibit a higher evaporation rate, similar to the scenario of substrate heating. These observations reinforce the notion that a higher droplet interface temperature leads to an enhanced evaporation rate, highlighting the importance of heat source positioning in controlling and manipulating the evaporation process.

The evolution of droplet morphology under localised heating is examined through the analysis of the contact angle, as presented in Fig. 4-11. The results shown in the figure cover the initial 360×10^3 timesteps from the start of heating, considering that evaporation takes longer when localised heating is applied. It can be observed that the contact angle undergoes a decrease during the heating-up phase, with a more significant reduction observed in droplets with smaller contact angles. This behaviour can be explained by Young's equation, which states that as the temperature increases, the surface tension of the liquid decreases, resulting in a decrease in the apparent contact angle. For hydrophilic surfaces, the increase in the contact angle, along with the variation in heat source locations, leads to changes in droplet morphology. Additionally, when asymmetric heating conditions are employed, the droplet shape becomes more or less asymmetric, especially in the case of droplets on superhydrophilic surfaces. This asymmetry is likely due to the influence of the asymmetric heating condition on the distribution of evaporation rate, particularly for flatter droplets. In such cases, the capillary flow fails to compensate adequately for the mass loss within a given timeframe, resulting in an asymmetric droplet morphology.

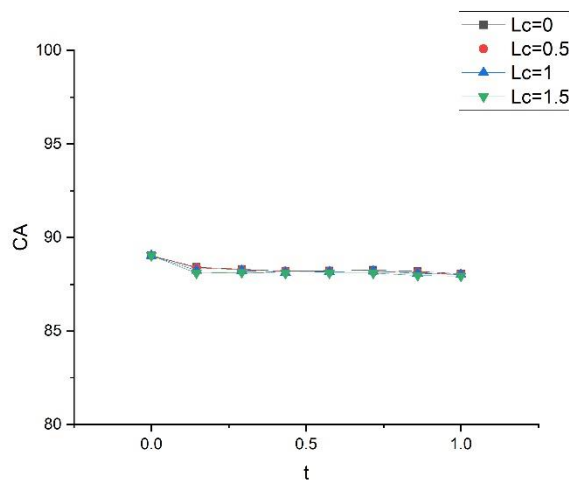
On a smooth substrate, the occurrence of an asymmetric flow pattern can result in the slipping of a droplet. This phenomenon can be attributed to two underlying factors. Firstly, the flow dynamics at the droplet interface interact with the surrounding vapour, generating forces that contribute to the slip. Secondly, the uneven distribution of evaporation rates on the



(a)



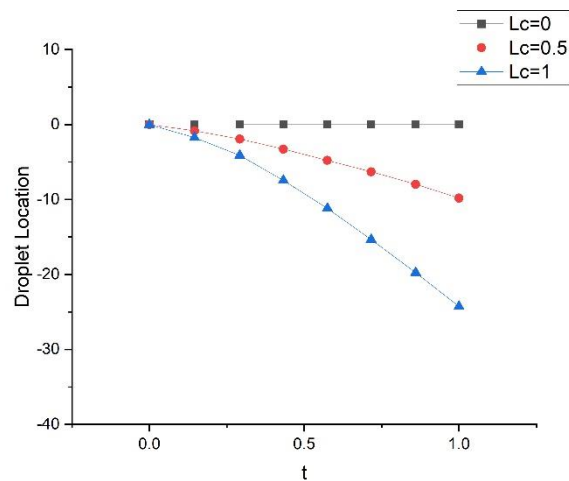
(b)



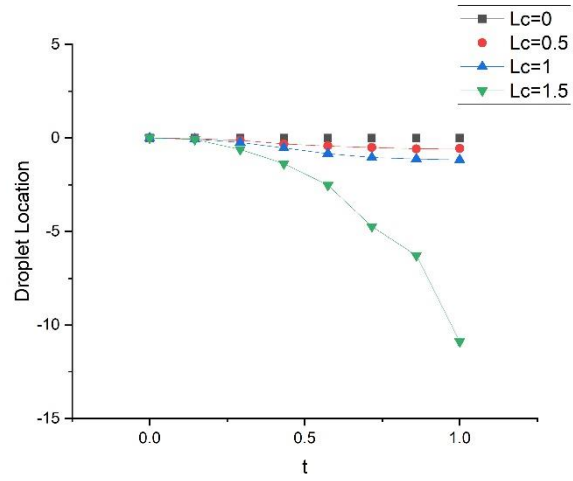
(c)

Fig. 4-11 Evolution of the contact angle for droplets on substrates with different surface wettability under different localised heating conditions. (a), (b), (c): evolution of contact angles of the droplet with basic contact angles at 30°, 60° and 90°

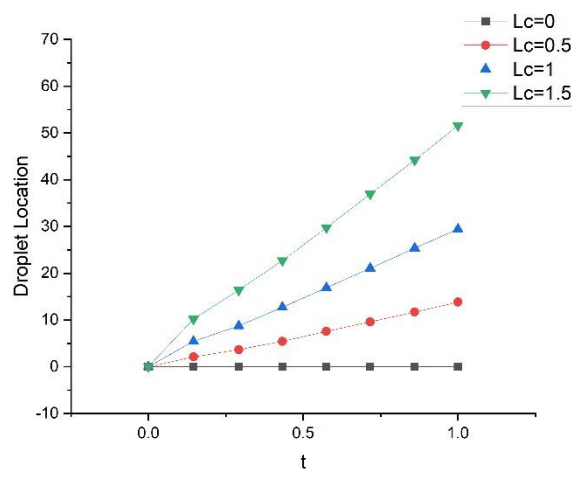
droplet surface arises from the asymmetric temperature distribution. The present study specifically examines the influence of asymmetric localised heating on droplet slip, and the findings are presented in Fig. 4-12. Note that the case $L_c = 1.5$ is still excluded in this part. The analysis of Fig. 4-12 reveals the prominent occurrence of droplet slip on superhydrophilic substrates. Moreover, when the heating source is positioned closer to the triple-phase contact point, the velocity of droplet slip increases. An interesting observation is that for contact angles of 30° and 60° , the droplet exhibits slip in the opposite direction to the placement of the heat source relative to the droplet centre. However, for a contact angle of 90° , the droplet slip direction is towards the side away from the droplet centre and towards the heat source. This suggests the presence of a critical point between 60° and 90° , beyond which the direction of droplet slipping reverses. It is important to acknowledge the complexity of the underlying mechanism driving this phenomenon, as multiple factors can influence droplet slip behaviour. Consequently, a comprehensive theoretical analysis is warranted, and further research should be dedicated to gaining a deeper understanding of this phenomenon.



(a)



(b)



(c)

Fig. 4-12 Droplet position evolution under asymmetric localised heating conditions when placed on a smooth substrate. (a) Contact angle = 30°; (b) Contact angle = 60°; (c) Contact angle = 90°

4.3 Conclusion

In this chapter, the research focused on investigating the influence of localised heating on the droplet evaporation process. To achieve this, a pseudo-potential multi-component multi-phase lattice Boltzmann method model is adopted. The validity of the model was successfully verified, and simulations were conducted considering different heating sources and various surface wettability conditions. Through numerical simulations, several key aspects are analysed and observed, leading to the following conclusions:

1. Asymmetrical localised heating conditions lead to the development of asymmetric flow patterns and temperature distributions within the droplet, consequently resulting in an asymmetric droplet shape. This effect is particularly prominent for droplets situated on superhydrophilic substrates.
2. Three different flows are observed in the droplet, the Marangoni flow, the natural convection, and the Capillary flow. The Marangoni flow aids in distributing heat across the droplet surface until it is counterbalanced by the Capillary flow. This behaviour becomes more evident in droplets with larger contact angles, where the Capillary flow is comparatively weaker.
3. The proximity of the heat source to the triple-phase contact point plays a significant role in determining the evaporation rate. Closer positioning of the heat source results in higher evaporation rates. Additionally, for the same heat source location, droplets with smaller contact angles exhibit higher evaporation rates.
4. Under asymmetrical localised heating conditions, droplets exhibit horizontal slipping on the substrate. The occurrence of droplet slip is influenced by both the droplet contact angle and the location of the heating source. It is worth noting that the

transition point for the slipping direction falls within the range of contact angles between 60° and 90° .

Chapter 5. Droplet impingement on a conical obstacle: A lattice Boltzmann study

Aside from evaporation, the phenomenon of droplet impingement has garnered significant attention in recent years due to its wide-ranging applications. In this chapter, a multi-component multiphase Lattice Boltzmann model is employed to investigate the impingement of droplets on conical obstacles. To accurately simulate the wetting behaviour of droplets on the hypotenuse of the cones, a modified non-slip bounce-back boundary condition is implemented. First, the model is validated to ensure its capability to produce accurate results. Subsequently, the influence of gravity, surface wettability, and surface temperature on the droplet impingement process are analysed. Three distinct droplet behaviours are observed upon impingement: deposition on the vertex of the cone, sliding down along the hypotenuse and splashing. An increase in gravity and hydrophilicity reduces the likelihood of droplet deposition on the vertex of the cone. Conversely, an increase in hydrophobicity and temperature enhances the probability of droplet splashing. To provide a comprehensive understanding, a detailed snapshot illustrating the influence of surface wettability on the droplet's movement and morphology is presented. Furthermore, the droplet's behaviour in the Leidenfrost stage is examined, and the relationship between the Jakob number and the droplet's velocity and temperature distribution is established. This investigation aims to unveil the characteristics of droplet impingement on conical obstacles and contribute fundamental insights to engineering applications such as spray cooling.

5.1 Introduction

The behaviour of droplets upon impingement is influenced by a multitude of factors, including the thermophysical properties of the liquid, droplet volume, impact velocity, and temperature. In a comprehensive investigation by Cheng et al.[214], the impact velocity, surface tension, initial droplet radius, equilibrium contact angle, and liquid viscosity were examined to understand their effects on droplet spreading. The findings revealed that an increase in impact velocity, surface tension, and initial droplet radius, or a decrease in equilibrium contact angle and liquid viscosity, leads to an enhanced rate of droplet spreading. Lin et al.[215] focused on exploring the impact dynamics of droplets and its dependence on liquid viscosity, impact velocity, and surface wettability. By systematically manipulating these factors, diverse droplet behaviors, including deposition, rebounding, and splashing, were observed, underscoring the significance of these parameters in governing the outcome of droplet impingement. Liu et al.[216] delved into the influence of the Weber number and surface temperature on droplet impingement. The investigation encompassed both non-Leidenfrost and Leidenfrost droplets, elucidating the interplay between temperature changes over time and the impact dynamics.

Droplet impingement phenomena are not limited to flat surfaces but also occur on surfaces with complex structures. Researchers have employed a combination of experimental and numerical methods to investigate droplet impingement on such surfaces, revealing the significant influence of surface geometry on impingement behaviors. Among the various surface geometries that have received extensive attention, some notable examples include flat surfaces[217, 218] and inclined walls[219, 220], pillars[221, 222], spheres[223, 224], cylinders[225], rectangular obstacles[226] and surfaces with microstructures[227, 228].

Droplet impingement on conical obstacles is an intriguing area of research that has garnered growing interest among scientists. The distinct geometric shape of cones distinguishes them from other surfaces and presents unique dynamics during droplet impingement. Despite being relatively less explored, this phenomenon holds great potential and has captured the attention of researchers. The pointed structure of cones plays a pivotal role in the behaviour of droplets upon impingement. Due to the sharp apex of the cone, the droplet is more prone to rupture upon impact, leading to the formation of multiple smaller droplets that slide down the surface. This fragmentation process significantly increases the contact area between the droplets and the cone, thereby enhancing heat transfer efficiency. This characteristic makes droplet impingement on conical obstacles a promising approach for applications requiring efficient heat transfer. Moreover, the interaction between the droplet and the conical surface is fundamentally altered due to the redirection of the droplet's vertical momentum along the hypotenuse of the cone. This redirection causes a deviation from the conventional behaviour observed on flat surfaces. The altered dynamics of the droplet-surface interaction on conical obstacles open up new avenues for investigation and offer unique opportunities for studying droplet behaviour under varied conditions. By delving into the intricate dynamics of droplet impingement on conical obstacles, researchers can gain valuable insights into the underlying mechanisms and leverage this understanding for diverse applications. The exploration of this relatively uncharted territory has the potential to contribute to advancements in areas such as heat transfer, surface engineering, and various technological fields that rely on efficient droplet-surface interactions. Shen et al.[229] adopted both experimental and numerical methods to investigate the impingement of a droplet on dome convex superhydrophobic surfaces. They observed that the utilisation of a convex surface resulted in a 28.5% reduction in droplet contact time compared to a flat superhydrophobic surface. The reduction in contact time was predominantly influenced by the retracting process. Similarly, Liu et al.[230]

examined the impingement of droplets on a copper surface decorated with conical nanostructures. They observed a phenomenon known as pancake bouncing, which led to a fourfold reduction in contact time compared to traditional complete rebound scenarios. Luo et al.[231] simulated the droplet impingement on a superhydrophobic cone. Their findings indicated that the contact time could be further reduced to 54% by appropriately selecting the Weber number and cone angle. They also constructed a phase diagram mapping the Weber number and cone angle. However, it is worth noting that these investigations primarily concentrated on reducing contact time, with limited attention given to other droplet behaviours such as rupturing and sliding. Additionally, those studies neglected the influence of temperature, which could affect the impingement behaviour dramatically. Moreover, the studies predominantly examined superhydrophobic surfaces, with hydrophilic and neutral wetting surfaces receiving relatively less attention.

Compared to numerical methods, experimental approaches encounter disadvantages in addressing challenges related to droplet size, timescale, and the fabrication of complex surfaces. Numerical simulations provide detailed information about the flow field, including velocity distribution and temperature profiles, and offer flexibility in adjusting relevant parameters[232]. In the aforementioned numerical research, the VOF method has been commonly employed. However, CFD encounters complexities when dealing with liquid-air interfaces, requiring substantial computational resources to solve pressure and velocity fields[233]. Compared to VOF, LBM has gained popularity among researchers due to its automatic phase interface tracking capability. Numerous studies have demonstrated the satisfactory performance of LBM in simulating droplet impingement cases. For instance, Gac and Gradoń[234] utilised a two-colour LBM model to simulate droplet impingement on spherical particles. They observed that as the Weber number increased, the droplet behaviour transitioned from merging with the particle to tearing and skirt scattering. Yan and Zu[200] proposed a LBM scheme and validated

its accuracy by simulating droplet wetting on heterogeneous surfaces. Their work further demonstrated the capability of LBM as a tool for solving wetting-related cases. Shen et al.[235] applied the famous Shan-Chen LBM model to study the droplet impact on a spherical obstacle. They observed various deformation processes, including droplet movement, spreading, nucleation, and falling. The occurrence of droplet splashing depended on the impact velocity and surface wettability. Merdasi et al.[236] and Bakhshan et al.[237] studied the droplet impingement on rectangular obstacles in a channel. The He-Chen-Zhang method and MRT collision operator were adopted respectively in their studies. The outcomes revealed that increased gravity, higher Weber numbers, increased hydrophobicity of the obstacles, and lower liquid viscosity contributed to droplet rupture.

In this chapter, the impingement of a droplet on the vertex of a conical obstacle is investigated using a MCMP pseudopotential LBM model. The model incorporates a modified boundary treatment method to accurately capture the wetting behaviour of the droplet on the hypotenuses of the cone. The model is first validated through Laplace law, D^2 law and equilibrium wetting test, and factors like gravity magnitude, surface wettability and surface temperature are studied for their influence on the droplet's impingement. This study aims to reveal the characteristics of the impingement between a droplet and a conical obstacle and provide fundamental support to related engineering applications such as spray cooling.

5.2 Numerical Methodology

The multi-component multiphase lattice Boltzmann method is adopted in this study, which is introduced in section 3.5. Besides, the ordinary half-way bounce-back boundary condition is modified to better suit the inclined cone hypotenuse while maintaining numerical stability and minimising the density fluctuation caused by thermodynamic inconsistency at the triple-phase contact line.

5.2.1 Geometry Setup and Boundary Conditions

The simulations in this study are performed in a 2D rectangular domain with dimensions of $L_x \times L_y$ to optimize computational resources. A conical obstacle is positioned at the centre of the bottom substrate, characterized by its vertex angle of 90° . Periodic boundaries are implemented along the left and right boundaries of the computational domain, while non-slip bounce-back boundaries[166] are adopted for the top and bottom boundaries, as well as the upper surface of the obstacle. The halfway bounce-back scheme proposed by Zou and He[238] is utilised at the non-slip boundaries. For the left and right boundaries, the boundary equations are given as: $f_{\sigma,i}((0-1, y), t) = f_{\sigma,i}((L_x, y), t)$ for the left boundary, and $f_{\sigma,i}((L_x + 1, y), t) = f_{\sigma,i}((0, y), t)$ for the right boundary. For thermal boundary conditions, $g_{\sigma,i}((0-1, y), t) = g_{\sigma,i}((L_x, y), t)$ and $g_{\sigma,i}((L_x + 1, y), t) = g_{\sigma,i}((0, y), t)$ can be obtained.

The non-slip bounce-back boundary conditions applied to the substrates can be written in the following forms, taking the bottom substrate as an example:

$$f_{\sigma,2}(x, t) = f_{\sigma,4}(x, t), \quad f_{\sigma,5}(x, t) = f_{\sigma,7}(x, t) + 0.5(f_{\sigma,3}(x, t) - f_{\sigma,1}(x, t)) - 0.25(F_{\sigma,x} + F_{\sigma,y}) \quad \text{and}$$
$$f_{\sigma,6}(x, t) = f_{\sigma,8}(x, t) + 0.5(f_{\sigma,1}(x, t) - f_{\sigma,3}(x, t)) + 0.25(F_{\sigma,x} - F_{\sigma,y}). \quad \text{To address the inclined}$$

hypotenuses of the obstacle, the boundary condition is established by combining the tuned non-slip bounce-back scheme with Filippova and Hänel's scheme[131].

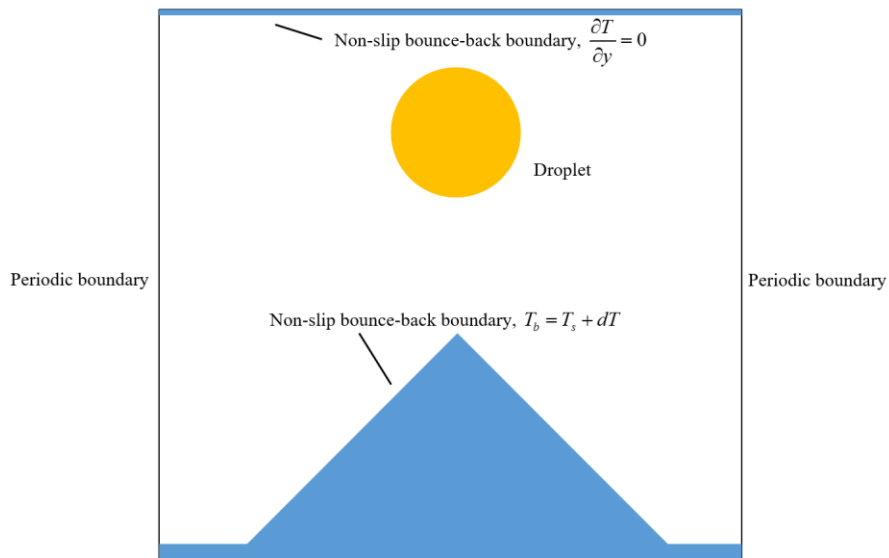


Fig. 5-1 Schematic of the simulation domain

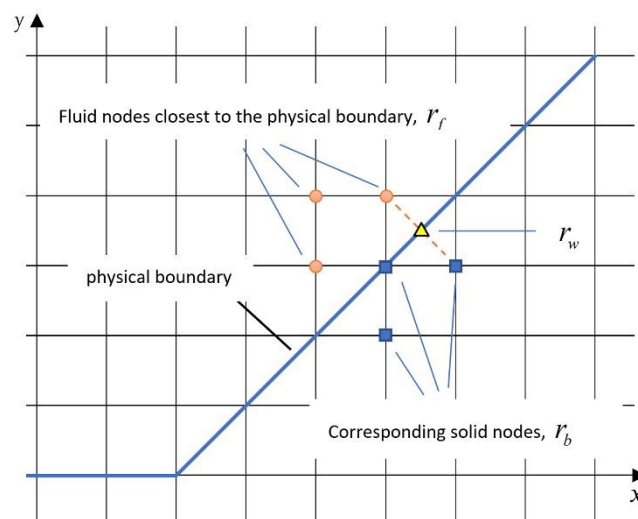


Fig. 5-2 Illustration of the hypotenuse boundary treatment using Filippova and Hänel's scheme.

As shown in Fig. 5-2, the relative distance between the fluid node adjusting a solid node and its closest neighbouring physical boundary is represented by a variable q , given as

$$q = \frac{|r_f - r_w|}{|r_f - r_b|}, \quad 0 < q < 1 \quad (5.1)$$

where r_w represents the location of the actual physical boundary.

To calculate the boundary momentum distribution function, a virtual equilibrium distribution function is constructed, written as:

$$f_i(r_b, t) = w_i \rho(r_f, t) \left[1 + \frac{3}{c^2} e_i \cdot u_{bf} + \frac{9}{2c^4} (e_i \cdot u_f)^2 - \frac{3}{2c^4} u_f \cdot u_f \right] \quad (5.2)$$

where u_{bf} is a virtual velocity to be determined.

The momentum distribution function after the collision step can be obtained as:

$$f_i(r_b, t) = (1 - \chi) f_i(r_f, t) + \chi f_i(r_b, t) + 2\omega_i \rho \frac{3}{c^2} e_i \cdot u_w \quad (5.3)$$

where u_w is the velocity of the wall, and it equals 0 in this case.

In Eq.(5.2) and (5.3), the values of u_{bf} and χ depend on the value of q :

$$\begin{cases} u_{bf} = u_f(r_f + e_i \delta t, t), & \chi = \frac{2q-1}{\tau-2} & q < 1/2 \\ u_{bf} = \frac{q-1}{q} u_f + \frac{1}{q} u_w, & \chi = \frac{2q-1}{\tau} & q \geq 1/2 \end{cases} \quad (5.4)$$

It can be observed that, in this case, $f_i(r_b, t)$ matches the standard bounce-back scheme when $q = 1/2$. However, the standard bounce-back boundary condition suffers from problems such as low numerical accuracy, and the absence of anti-slip terms can lead to an unstable wetting condition for the droplet. Hence, the modified non-slip bounce-back scheme is applied here as a solution. Taking the left-side hypotenuse as an example, the modified non-slip bounce-back boundary condition can be written as: $f_6(x, t) = f_8(x, t)$,

$$f_2(x, t) = f_4(x, t) + 0.5(f_7(x, t) - f_5(x, t)) + F_x / \kappa_x + F_y / \kappa_y \text{ and}$$

$$f_3(x, t) = f_1(x, t) + 0.5(f_5(x, t) - f_7(x, t)) + F_x / \kappa_x + F_y / \kappa_y, \text{ where } \kappa_x \text{ and } \kappa_y \text{ are adjustable}$$

parameters related to the angle of the hypotenuse and the solid-fluid interaction force coefficient G_s . While for fluid nodes with other values of q , the algorithm (5.1) - (5.4) is adopted. By introducing the modified boundary condition treatment method, a steady wetting condition for droplets on hypotenuses can be achieved.

For the thermal boundary condition, constant temperatures are applied to the lower solid substrates. The lower substrates are set at five different temperatures throughout this study as $T_b = T_s + dT$, with dT being 0, $0.05T_c$, $0.1T_c$, $0.2T_c$ and $0.3T_c$ respectively. The upper substrate adopts the thermal non-equilibrium extrapolation scheme in all cases.

5.2.2 Model Validation

In this section, the validity and accuracy of the model will be assessed through three distinct simulations: the Laplace law, the D^2 law, and stable wetting condition on inclined surfaces.

1. The Laplace law

The model is compared against the Laplace law for verification. The Laplace law reflects the relationship between the pressure difference across the vapour/droplet interface Δp , and the droplet radius R , that the pressure difference is inversely proportional to the droplet radius with the proportionality coefficient equalling to the surface tension σ . The simulation is conducted using the same geometry setup as previously described, but without the inclusion of the conical obstacle. The droplet is placed in the centre of the domain, of which the density is initialised as

$$\rho_{\sigma}(x, y) = \frac{\rho_{\sigma, \text{in}} + \rho_{\sigma, \text{out}}}{2} - \frac{\rho_{\sigma, \text{in}} - \rho_{\sigma, \text{out}}}{2} \tanh \left[\frac{2(\sqrt{(x-x_0)^2 + (y-y_0)^2} - R_0)}{W} \right] \quad (5.5)$$

where $\rho_{\sigma, \text{in}}$ and $\rho_{\sigma, \text{out}}$ are the density of the σ_{th} component inside and outside of the droplet, R_0 is the radius of the droplet and W is the thickness of the initial interface width.

The simulation is carried out at different temperatures: $T = 0.8T_c$, $T = 0.85T_c$ and $T = 0.9T_c$, with the saturated liquid and vapour density listed in the Table 1.

Table 1

Saturated density distribution at different temperatures

	$0.8T_c$	$0.85T_c$	$0.9T_c$
ρ_l	7.2039	6.6293	5.9079
ρ_v	0.1971	0.3413	0.5801

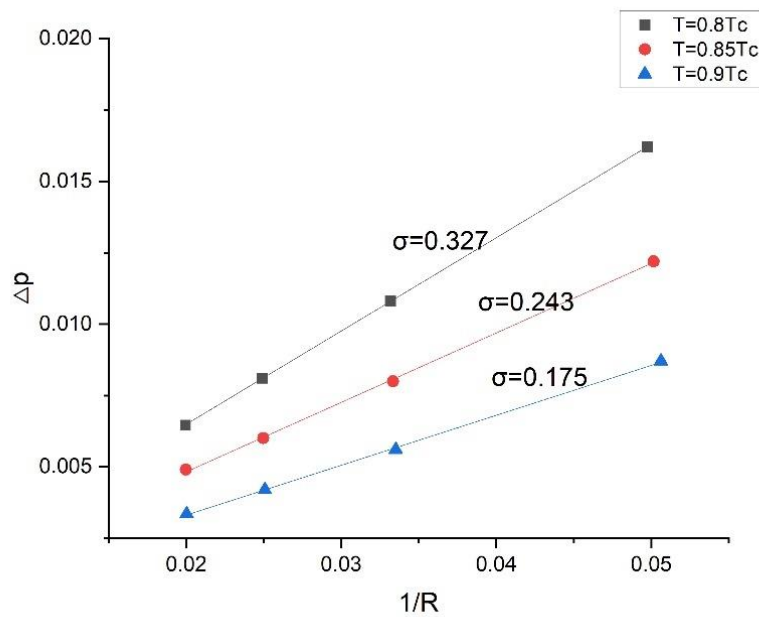


Fig. 5-3 The relationship between the pressure drops at the droplet interface and droplet radius for different temperatures. (σ : surface tension).

The initial density of the non-condensable gas is set to 0.0017, resulting in a weight fraction of approximately 0.025%. The droplet radius is varied from 20 lattice units (l.u.) to 50 l.u. with a step size of 10 l.u. The relationship between the droplet radius and the pressure difference is then analysed and plotted in Fig. 5-3. The obtained results indicate that the model successfully satisfies the Laplace law.

2. The D^2 law

The D^2 law indicates that when the thermal-physical parameters remain constant, the square of the droplet diameter should exhibit a linear relationship with time during the entire evaporation process[239]. Satisfying the D^2 law would prove the model's capacity to solve cases with phase changes. The simulation setup is similar to that in section 5.2.1, except that the temperature of the surrounding vapour is set to $T_v = T_l + \Delta T$, while that of the liquid droplet is set to T_l . Also, a non-equilibrium extrapolation momentum boundary condition is

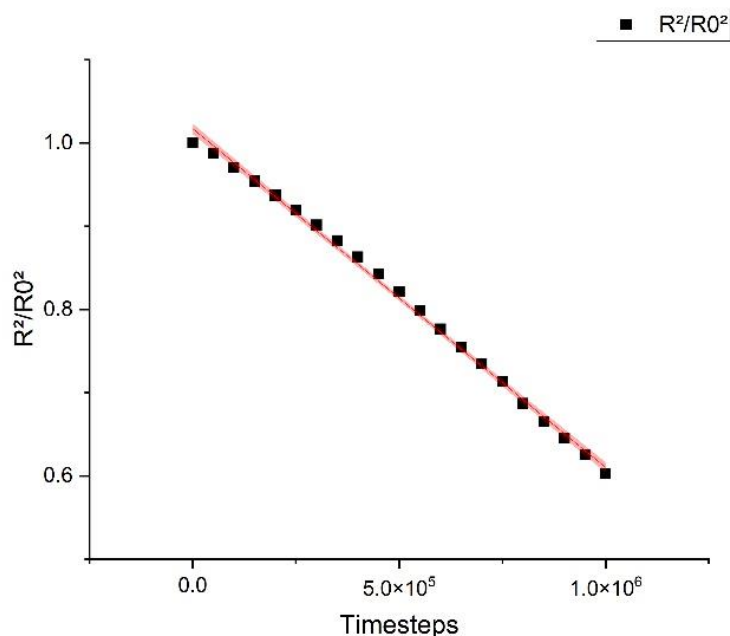


Fig. 5-4 Normalised square of droplet diameter versus the evaporating time

applied to all boundaries to enable the vapour to escape from the simulating domain, so the density and the pressure of the vapour can remain constant. Other thermophysical parameters, such as thermal diffusivity and specific heat capacity, are kept constant. A droplet with an initial radius of 40 l.u. is placed in the centre of the domain, and after the first 10^6 timesteps, the relation between R^2 / R_0^2 and evaporation time is depicted in Fig. 5-4. It can be observed that the evaporating curve obeys the D^2 law, confirming that the model is capable of accurately simulating cases involving phase change.

3. Wettability on inclined surfaces

To investigate the capability of the modified boundary treatment method in achieving stable contact angles during droplet wetting on inclined surfaces, dedicated simulations are conducted. The simulation setup aligns with the geometry described above, where a droplet with a radius of 30 l.u. is positioned at the centre of a hypotenuse inclined at 45° . The upper and lower boundaries use the halfway bounce-back boundary conditions, while the left and right boundaries are periodic boundaries. The modified boundary condition treatment method introduced in section 5.2 is adopted for the inclined surface. The domain remains unaffected by external forces, and the temperature is maintained at a constant value. The surrounding environment of the droplet consists of both vapour and non-condensable gas. The different contact angles of the droplet can be achieved by tuning the interaction force coefficient G_s in the formula (3.36) as well as κ_x and κ_y . The relationship of G_s and the equilibrium contact angle are shown in the figure below, proving that stable wetting conditions can be achieved using this method.

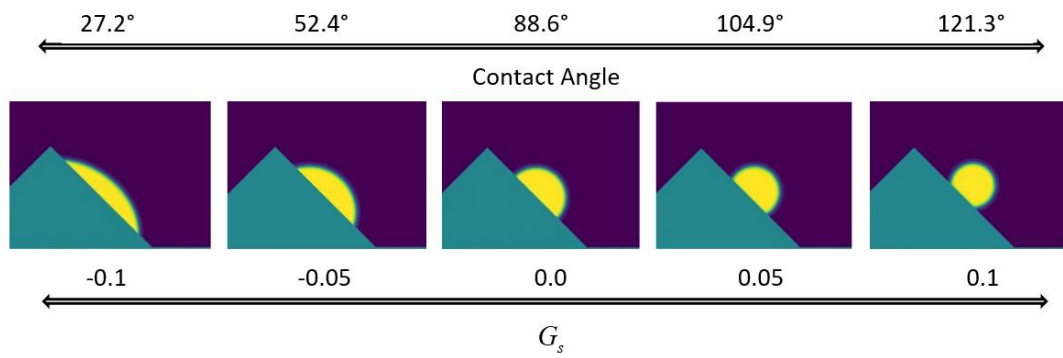


Fig. 5-5 Different wetting conditions of the droplet on the cone hypotenuse achieved by adjusting coefficient G_s

5.3 Results and Discussion

In this study, simulations are conducted to investigate the impingement behaviour of droplets on the vertex of conical obstacles. The behaviour of a droplet upon impingement is influenced by various factors, including its thermophysical properties and the angle at which it impacts the surface. The occurrence of off-centre impingement and impingement at different angles introduces additional complexity and potential variations in outcomes. However, due to the scope of this study, the focus is primarily on examining a representative case involving symmetric impact on a cone with a fixed vertex angle of 90° . The geometry setup utilized in the simulations aligns with the configuration shown in Fig. 5-1. Initially, the system is set to a temperature equal to the saturated temperature $T_s = 0.85T_c$. A droplet with a radius of 30 l.u. is positioned at a height of 225 l.u. and allowed to stabilize for 5000 timesteps. Subsequently, gravity force is applied to the system, enabling it to reach a thermodynamic equilibrium state. The study explores the impact of various factors, including the magnitude of gravity, the surface wettability of the obstacle, and the temperature of the obstacle. However, it is important to note that due to the limitations of the 2D model used in this simulation, the influence of surface tension in the horizontal direction is not considered. This aspect will be further addressed in subsequent chapters of the thesis.

5.3.1. The effect of gravity

In the investigation of droplet impingement scenarios, two main approaches are commonly utilized. The first approach involves neglecting the influence of gravity and imparting an initial velocity to the droplet. The second approach involves allowing the droplet to undergo free fall, driven solely by the force of gravity, without any initial velocity. In the context of this study, it is important to consider that gravity not only affects the

droplet's velocity but also has an impact on its shape and internal flow dynamics. Given that both the upper and lower boundaries in the simulation are implemented as bounce-back boundaries, the first approach, which involves providing an initial velocity to the droplet, does not produce the desired outcome. This is because the drag force exerted by the boundaries would impede the droplet's acceleration. As a result, the second approach, which allows the droplet to freely fall under the influence of gravity, is adopted in this study.

According to the research of Rahmati and Zarareh[240], the parameters associated with the impingement, like the impingement velocity, Reynold number, Weber number and Bond number, can be given in the following forms:

$$v_0 = \sqrt{2g(H' - r)} \quad (5.6)$$

$$Re = \frac{v_0 d}{\nu} \quad (5.7)$$

$$We = \frac{\rho_l v_0^2 d}{\sigma} \quad (5.8)$$

$$Bo = \frac{\rho_l d^2 g}{\sigma} \quad (5.9)$$

where H' is the initial height of the droplet centre, d is the droplet diameter, ν is the kinematic viscosity of the droplet. Also, the dimensionless time is given as

$$t^* = \frac{t}{\sqrt{d/g}} \quad (5.10)$$

Note that in this study, the dimensionless time counts from the moment that gravity is applied.

In this simulation, three different magnitudes of gravity are considered, respectively 1×10^{-5} , 2×10^{-5} and 3×10^{-5} . The initial height of the droplet is fixed at 225 l.u., and the

initial fluid properties remain constant. Based on these values, the corresponding dimensionless parameters can be obtained as follows:

Table 2

Corresponding parameters of different gravity magnitudes

g	v_0	Re	We	Bo
0.00001	0.05	18.00	4.09	0.98
0.00002	0.07	25.46	8.18	1.96
0.00003	0.09	31.18	12.28	2.95

For each gravity magnitude, three different stages of the impingement process are investigated. The first stage occurs when the droplet fully wraps around the vertex, followed by the second stage, which is the moment prior to the droplet rupturing at the vertex. Finally, the third stage is characterized by the droplet sliding down the hypotenuse of the conical obstacle, reaching a state of relative equilibrium in terms of its advancing and receding contact angles. The substrates used in these simulations have neutral wettability, and no heating condition is applied. As shown in the pictures below, for $g = 1 \times 10^{-5}$, the droplet rebounds upon impinging against the vertex and eventually comes to a stop while depositing on the vertex. The contact angle on each side of the droplet is observed to be approximately 84° . This behaviour arises due to the weak momentum of the droplet, which is unable to overcome the interaction force between the liquid molecules that wrap around the vertex. While for $g = 2 \times 10^{-5}$ and $g = 3 \times 10^{-5}$, the increased gravitational force and momentum enable the droplet to rupture at the vertex. Furthermore, it is noted that a stronger gravitational force leads to a higher vertical velocity for the droplet during its descent. Additionally, as the droplet slides down the hypotenuse, it exhibits a flattened shape. In the third stage, the advancing and receding contact angles are measured as 91.4° and 78.1° for $g = 2 \times 10^{-5}$, while for $g = 3 \times 10^{-5}$, they are 96.5° and 69.3° , respectively.

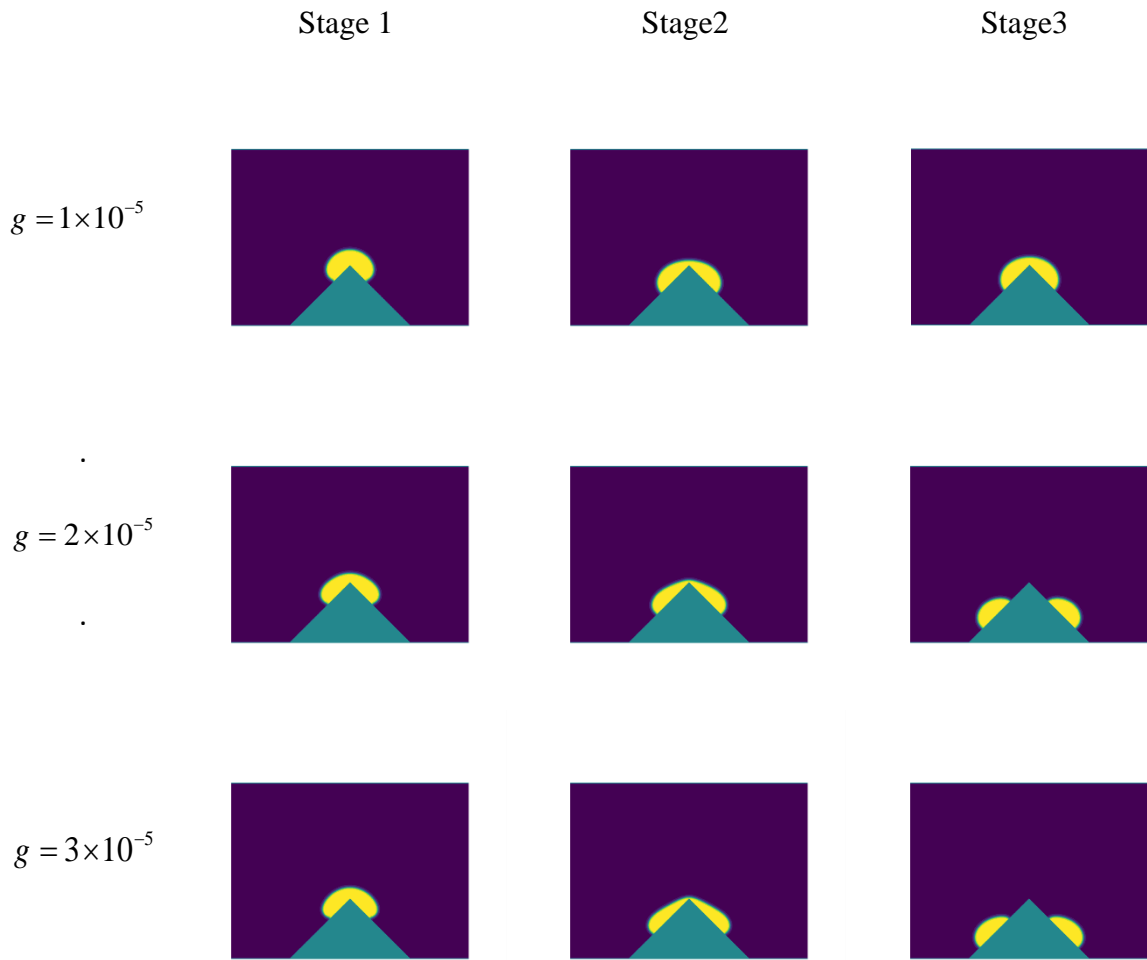


Fig. 5-6 Droplet impingement on the cone vertex under different gravity magnitudes

5.3.2. The effect of surface wettability

While investigating the impingement and sliding behaviour of droplets on inclined surfaces, the surface wettability plays a significant role. However, in practical scenarios, altering the surface wettability while keeping other surface parameters constant can be challenging. Simulations provide a valuable tool to isolate and study the effect of surface wettability on droplet behaviour. Ma et al.[241] used the LBM model to examine the impingement of droplets on inclined surfaces with varying wettability. However, the Zheng-Shu-Chew (ZSC) model used in their study requires improvements in terms of

thermodynamic consistency. In this current study, four different wetting conditions are investigated by modifying the value of G_s in Eq. (3.36). The gravity is set to $g = 2 \times 10^{-5}$, and no heating condition is considered. The results are shown in the snapshot below. Since the geometry setup is symmetric, only the right half of the obstacle is displayed.

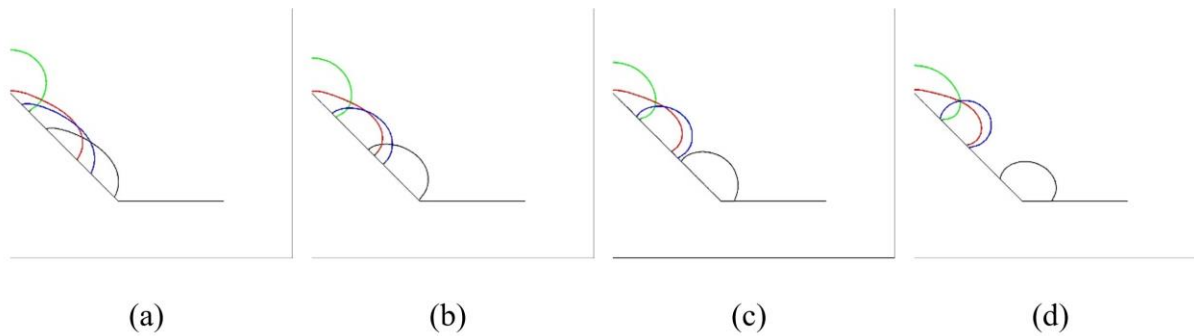


Fig. 5-7 Snapshot of the droplet impinging on surfaces of different wettability (a: contact angle = 69.9°; b: contact angle = 88.5°; c: contact angle = 104.5°; d: contact angle = 120.4°. Green line: $t^ = 2.31$; red line: $t^* = 3.46$; blue line $t^* = 4.91$; black line: $t^* = 8.08$)*

In Fig 5-7, (a)-(d) represent different values of G_s (-0.05, 0, 0.05, and 0.1) corresponding to different surface wettability conditions. The contact angle of the droplet on a flat surface is 69.9°, 88.5°, 104.5°, and 120.4° for these respective values of G_s . These four snapshots, outlined in different colours, are taken at specific time intervals: $t^* = 2.31$ for green, $t^* = 3.46$ for red, $t^* = 4.91$ for blue and $t^* = 8.08$ for black. At $t^* = 2.31$, the difference in advancing contact angles is minimal as the droplet-surface interaction just started. As time proceeds to $t^* = 3.46$, the influence of surface wettability becomes more apparent, and the advancing contact angle gradually reaches a stable value. Meanwhile, on the vertex of the obstacle, the droplet starts to rupture. For $t^* = 4.91$, the droplet fully breaks apart, and the force acting on the receding contact line becomes the interaction force between the liquid and the surface, which is much smaller than the interaction force between liquid molecules on a hydrophobic surface. This leads to a rapid downward movement of the

receding contact line, causing the droplet's centre of gravity to descend quickly. This phenomenon resembles weightlessness. On hydrophobic surfaces, the advancing contact line of the droplet remains relatively stationary due to this weightlessness effect. Conversely, on hydrophilic surfaces, this weightlessness phenomenon is not observed, as the interaction force between liquid molecules is weaker compared to the force between the liquid and the surface. In the final snapshot, the droplet smoothly slides down the surface, with both the advancing and receding contact angles remaining relatively stable. The velocity profile of the droplet on a hydrophilic surface appears more linear, whereas, on a hydrophobic surface, the velocity undergoes a stall when the droplet ruptures on the vertex due to the weightlessness phenomenon. Furthermore, the droplet on a hydrophobic surface exhibits a higher overall velocity compared to a hydrophilic surface, attributable to the reduced interaction force with the surface. This is further proved in Fig. 5-8, in which the relationship between the droplet centre point and dimensionless time is shown.

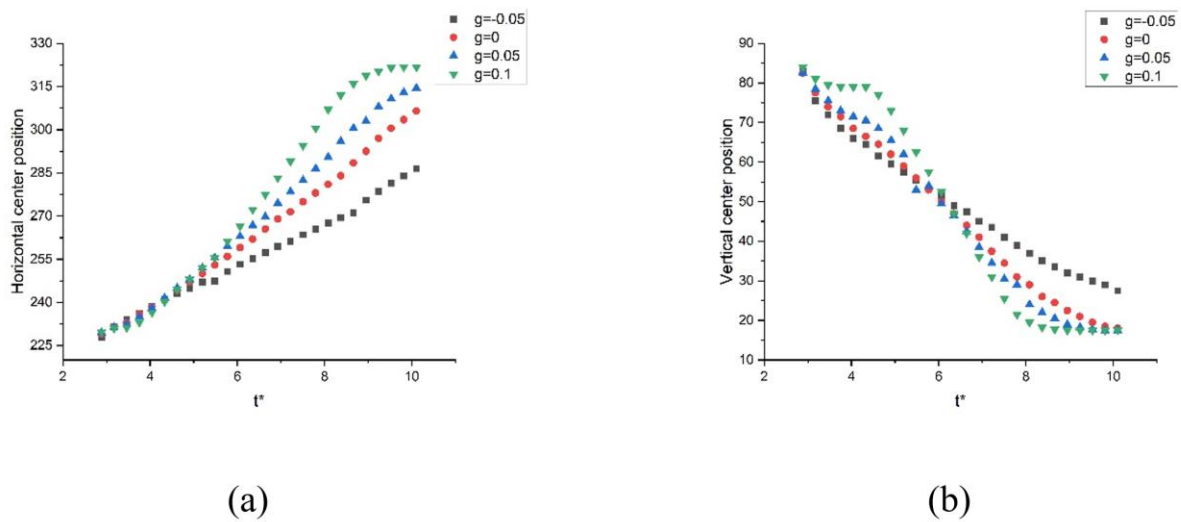


Fig. 5-8 Evolution of droplet position upon impingement on surfaces of different wettability. (Position unit: l.u.)

5.3.3. The effect of surface temperature

While the impingement of droplets has been extensively investigated by researchers, the influence of temperature is often overlooked. This is primarily due to the short duration of the impingement process, which allows the assumption of negligible droplet evaporation. However, it's observed that the temperature of the obstacle surface plays a crucial role in shaping the droplet's behaviour, particularly when the temperature reaches a threshold to induce the Leidenfrost effect. Therefore, in this section, the effect of varying surface temperatures on the droplet's dynamics is examined by subjecting the conical obstacle to different temperature conditions.

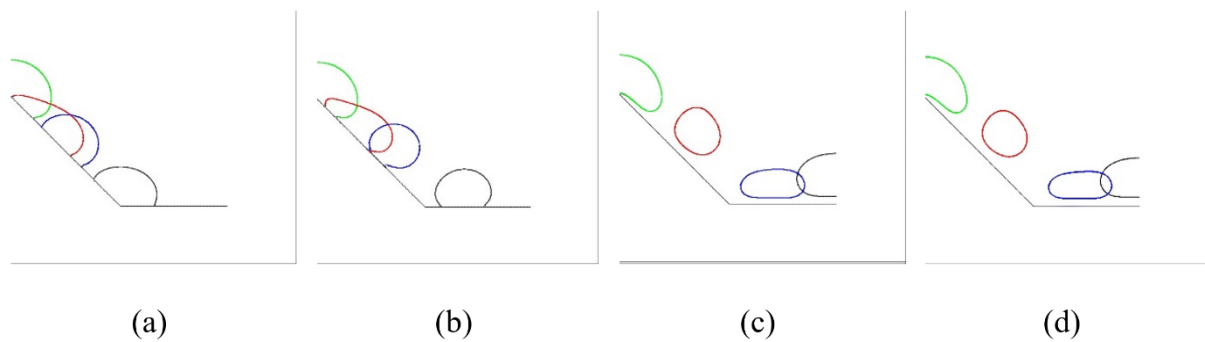


Fig. 5-9 Snapshot of the droplet impinging on surfaces of different temperatures. (a: $dT = 0.05$; b: $dT = 0.1$; c: $dT = 0.2$; d: $dT = 0.3$. Green line: $t^* = 2.31$; red line: $t^* = 3.46$; blue line $t^* = 4.91$; black line: $t^* = 8.08$)

In Fig. 5-10, the snapshots of the droplets impinging on surfaces with different temperatures are presented. All other parameters are held constant, including a gravity force of $g = 2 \times 10^{-5}$ and neutral surface wettability ($G_s = 0$). The temperature of the surface is denoted as $T_w = T_s + dT$, with $dT = 0.05$ in Fig 5-9 (a), $dT = 0.1$ and 0.2 in (b) and (c), $dT = 0.3$ in (d) correspondingly. Jakob number, written as

$$Ja = \frac{(T_w - T_s)c_p}{h_v} \quad (5.11)$$

is used to measure the influence of the substrate temperature, where h_{lv} is the liquid-vapour latent heat. The snapshots (a)-(d) correspond to different surface temperatures, and the Jakob numbers are provided as 0.04, 0.075, 0.15, and 0.23, respectively. The time intervals between the snapshots remain the same as in section 5.3.3, and the droplets are marked with the same colours as mentioned earlier. It can be found that in Fig. 5-9 (a) and (b), with the increase of surface temperature, the contact area between the droplet and the substrate shrinks, and the droplet enters the “semi-Leidenfrost” stage. If the temperature keeps increasing, as shown in Fig. 5-9 (c), the droplet detaches from the solid surface, and the existence of the vapour layer removes all the interaction force between the droplet and the surface, making the droplet slide down at the maximum rate possible. Comparing Fig. 5-9 (c) and (d), it can be observed that there is minimal distinction between the two cases with different surface temperatures. This can be attributed to the presence of a vapour layer, which acts as an insulating cushion during the Leidenfrost phenomenon. Vapour possesses significantly lower thermal conductivity compared to water, thereby reducing the impact of increased surface temperature on the impingement process. Additionally, since the droplet is already in a levitating state, the surface temperature variation has negligible influence on the droplet velocity.

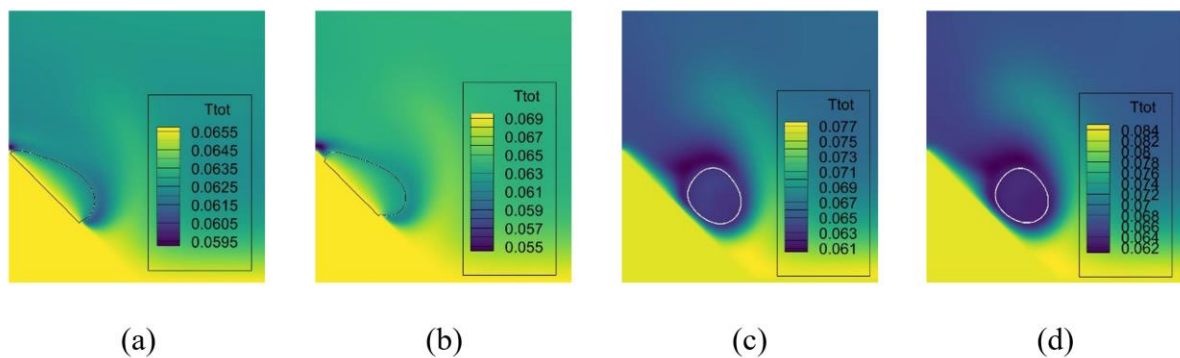


Fig. 5-10 Temperature profiles of the flow field at $t^* = 3.46$ for different surface temperatures. (a: $dT = 0.05$; b: $dT = 0.1$; c: $dT = 0.2$; d: $dT = 0.3$)

In Fig. 5-10, the temperature contours of the flow field are shown at $t^* = 3.46$ for Ja ranging from 0.04 to 0.23. In addition to the variation in the shape of the droplets, there are other observations to be made. In Fig. 5-9 (a) and (b), the temperature at the junction line between the droplet and the solid surface is nearly equal to the substrate temperature T_w . However, as the distance from the obstacle surface increases, the temperature gradually decreases. On the other hand, in Fig. 5-9 (c) and (d), the temperature dropwise remains relatively constant as the droplet is in the Leidenfrost stage. The presence of the vapour layer prevents direct heat transfer from the substrate to the droplet. Furthermore, the high velocity of the droplet hinders excessive heat absorption, resulting in the liquid component remaining relatively cool compared to the surrounding vapour. The majority of the absorbed heat is utilised for vaporisation, leading to a limited increase in the droplet's temperature.

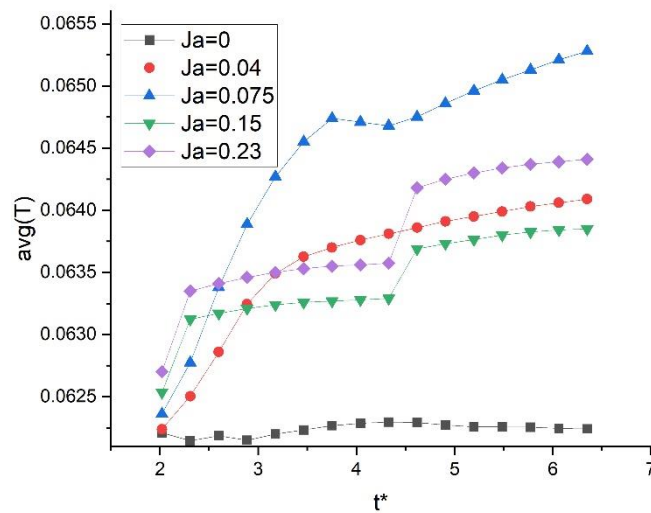


Fig. 5-11 Mean temperature of the droplet during the impingement process.

In Figure 5-11, the relationship between the droplet's mean temperature and dimensionless time is depicted. Different Ja numbers correspond to different heating rates during the impingement process. Overall, the mean temperature is highest for the case of

$Ja = 0.075$, followed by $Ja = 0.23$, $Ja = 0.04$, and $Ja = 0.15$ with the lowest mean temperature. It is worth noting that even though the Jakob number is much higher in the Leidenfrost stage, the droplet exhibits a lower temperature. This indicates that the vapor layer effectively blocks heat transfer into the droplet. Additionally, the deformation of the droplet during the impact process causes minor temperature fluctuations, as observed in the curve for $Ja = 0.0$. These fluctuations can be attributed to viscous dissipation resulting from the deformation. For the cases of $Ja = 0.04$, the mean temperature rises at a higher rate when $t^* \in (2,3)$. As t^* approaches 4, the rate of temperature increase gradually slows down. This can be explained by referring to Fig. 5-7, where it can be observed that the contact line between the droplet and the surface decreases sharply as t^* approaches 4.91. This reduction in contact area leads to a decreased heat exchange size and, consequently, a reduced rate of temperature increase. For the case of $Ja = 0.15$ and $Ja = 0.23$, a sharp increase in the droplet temperature is observed between $t^* \in (2, 2.5)$ and $t^* \in (4, 5)$. According to Fig. 5-7, during this period, the droplet is impacting the vertex of the obstacle and the bottom substrate, respectively. The impact effect can result in a temporary reduction in the vapor layer thickness or even a momentary connection between the droplet and the superheated substrate. After this initial impact phase, both droplets continue to heat up at lower rates.

5.4 Conclusion and Prospection

In this chapter, a multi-component multiphase Lattice Boltzmann model was developed to investigate the impingement process of a droplet on the vertex of a conical obstacle. The model integrates a mixed non-slip bounce-back boundary treatment method, allowing for accurate simulation of droplet wetting on the hypotenuses. The influence of various factors, including gravity magnitude, surface wettability, and substrate temperature, was examined. The focus of this investigation was on droplet morphology, velocity profiles, and temperature distributions. The following conclusions were drawn from the study:

1. Three distinct behaviours of droplets were observed during the impingement process: deposition on the vertex, sliding down along the hypotenuse and splashing. The likelihood of deposition on the vertex increased under conditions of lower gravity and hydrophobic surfaces. Conversely, a more hydrophilic surface increased the probability of sliding down along the hypotenuse. Higher temperatures and more hydrophobic surfaces facilitated droplet detachment from the surface, resulting in splashing.
2. Increased surface hydrophobicity generally led to higher sliding velocities of the droplet. However, on hydrophobic surfaces, the non-equilibrium wetting condition at the moment of droplet rupture on the receding edge caused a temporary weightlessness phenomenon, temporarily halting the droplet's motion.
3. Leidenfrost effect happens in cases where $Ja \geq 0.15$. The heat transfer rate is then reduced as the vapour layer between the droplet and substrate has a lower thermal conductivity. The highest droplet mean temperature is observed when $Ja = 0.075$. On the other hand, the droplet in the Leidenfrost stage has a higher velocity as the interaction force between the droplet and the surface disappears.

Chapter 6. Investigation on droplets impacting a conical structure

The employment of a 2D model in Chapter 5 imposes certain limitations, preventing the reconstruction of the horizontal connectivity of the droplet ring and precluding the observation of significant phenomena such as droplet retraction and rebounding. Moreover, the omission of influential factors, such as cone angles and surface roughness, in the aforementioned chapter further necessitates the conduction of an experimental study. Accordingly, this experimental investigation serves as a supplementary endeavour to explore the dynamics of droplet impingement on conical obstacles. By addressing these aforementioned limitations, the current study aims to provide a more comprehensive understanding of the impingement process and shed light on the influence of critical factors.

6.1 Introduction

The advancement of industrial applications has led to the design of enhanced surfaces that deviate from conventional flat surfaces. The dynamic behaviour of droplets on these surfaces provides insights into the redistribution of mass and momentum during the interaction between droplets and microstructures or microporous structures. In recent studies, particular attention has been given to investigating the dynamics of droplet impingement on conical substrates. The presence of the hypotenuse in conical structures expands the impingement area, transforming the droplet's interaction from a flat substrate to a three-dimensional cubic zone. This expansion facilitates the observation and analysis of processes such as droplet spreading and retracting, offering valuable insights into their behaviour. Luo et al.[231] focused on investigating the dynamics of droplet rebound on a superhydrophobic cone surface with various cone angles. Both numerical simulations and experimental observations were carried out. They identified three distinct phases based on the combination of Weber number and cone angle. The specific behaviours and characteristics of the droplet rebounding dynamics varied depending on these factors. In 2017, Shen et al.[229] designed a dome convex superhydrophobic surface and investigated the bouncing dynamics of impacting droplets. They discovered that droplets exhibited rapid bouncing behaviour, with a 28.5% reduction in the contact time compared to that observed on flat superhydrophobic surfaces.

The aforementioned investigations primarily concentrate on the phenomenon of droplet impingement specifically on superhydrophobic surfaces. The primary objective of these investigations is to minimize the contact time during the droplet bouncing process, thereby enhancing the performance of various droplet impingement applications, including self-cleaning, anti-frosting, and anti-icing. However, for alternative applications such as spray cooling, where the desired outcome may vary, it is imperative to explore the influence of additional factors. Notably, the effects of surface geometry[242] and surface roughness[243]

warrant investigation in order to comprehensively understand and optimize the performance of droplet impingement for such applications..

Experimental studies on droplet impact dynamics commonly focus on three key aspects: the spreading behaviour, the splashing threshold, and the impact of substrate properties. The spreading behaviour is typically characterized by the maximum spreading factor, denoted as β_{\max} . At lower impact velocities, droplets deposit on the surface without splashing. Upon contact, the droplet's vertical momentum is partially converted to horizontal momentum, causing the droplet to initially spread outward until it reaches a maximum spreading diameter, denoted as d_{\max} . Subsequently, the liquid lamella either remains static or retracts based on the interplay between liquid surface tension, inertia, and viscosity. Several empirical and theoretical models have been developed to evaluate β_{\max} , and various formulas have been proposed to fit experimental and numerical results[244-248].

When the impact velocity exceeds a certain threshold, droplet splashing occurs, characterized by the detachment of tiny droplets from the periphery of the lamella and the generation of secondary droplets. Two primary types of splashing can be observed: prompt splashing and corona splashing. Prompt splashing occurs when droplets impinge on rough surfaces, leading to the direct release of small droplets from the advancing lamella's periphery. On the other hand, corona splashing typically occurs on smooth surfaces, where the liquid lamella detaches from the substrate, forming a bowl-like structure that subsequently breaks up into smaller droplets. The specific impact velocities required to initiate splashing vary depending on the surface characteristics. Therefore, it is crucial to identify the splashing thresholds and determine the minimum impact velocity necessary for droplet breakup and the subsequent generation of secondary droplets. However, a comprehensive understanding of the splashing threshold and the influence of factors such as air and surface roughness is currently

lacking and requires further investigation. Xu et al.[249] conducted experiments on droplet impact on smooth substrates by manipulating the surrounding air pressure, demonstrating the suppression of corona splashing by reducing the surrounding air pressure. Josserand and Thoroddsen[88] and Moreira et al.[250] reviewed and discussed the differences among various proposed splashing thresholds. Current research efforts are dedicated to determining critical values for different impact conditions and examining the effects of various factors on splashing behaviors. However, the influence of these factors is not yet well understood, and a universal correlation between the splash threshold and other factors has yet to be established[251].

This chapter addresses a research gap by conducting an experimental investigation that explores the combined effects of surface roughness and conical structures on droplet impingement. The study involves the impact of droplets on nine conical structures with varying cone angles and surface roughness. To capture the entire impacting process and analyse the droplet behaviours, a high-speed camera is employed. Special emphasis is placed on understanding the influence of surface roughness on droplet impact behaviours. The anticipated outcomes of this work are twofold: advancing the understanding of droplet impingement on conical structures and providing valuable insights for applications such as spray cooling.

6.2 Experiment set-up

The experimental setup employed in this research aims to investigate the behaviour of droplets impacting conical substrates with different surface roughness. The test rig consists of several key components that facilitate controlled droplet generation, precise impact velocity control, and accurate data acquisition. Fig. 6-1 illustrates the schematic of the experimental apparatus. The droplet generation is accomplished using a syringe connected to a pump. The pump incorporates two pulleys on its back side, which are connected to a vertical slide. This configuration allows for easy adjustment of the droplet volume by varying the pump displacement. To control the impacting velocity, the height of the pump can be adjusted, thereby altering the height difference between the syringe and the cone tip. The impingement velocity can be obtained by $v_0 = \sqrt{2gh}$, where g and h represent the gravity acceleration and the height between the syringe and cone tip, respectively.

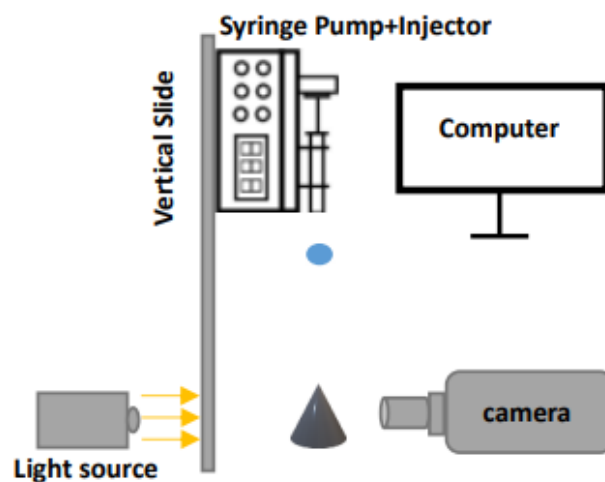


Fig. 6-1 Schematics of experimental apparatus

In this experiment, droplets are considered spherical in shape with an initial diameter $d_0 = 3 \pm 0.05 \text{ mm}$. This is achieved by tuning the pump's displacement. They are released

vertically and allowed to freefall under gravity until they impact the cone tip. To determine the drop point and further determine the placement of the cones, the drop was allowed free fall several times before the placement of the cones. The impacting velocity v_0 ranges within $0.63 \leq v_0 \leq 3.49(m/s)$, corresponding to Weber number from 16 to 501. The droplet's behaviour during the impact process is recorded using a high-speed camera (Phantom v12.1) operating at a remarkable frame rate of 6000 frames per second. Two light sources are strategically placed on either side of the cone to ensure optimal illumination and clear visualisation of the impact event. The exposure time is set at $3 \mu s$, allowing for precise capturing of the droplet's motion. The resulting videos have a high resolution of 1024×769 pixels, providing detailed visual information for subsequent analysis. The video was processed on a laptop using the Phantom Camera Control software. For each case, the experiment was conducted multiple times, and only those in which droplets fall precisely on the centre of cone tips are taken into account.

Regarding the cone substrate, it is constructed from aluminium and manufactured with three different cone angles: 60° , 90° , and 120° . The height and substrate diameter for those cones are: 8 cm and 9.24 cm for those with 60° cone angle, 4.5 cm and 9 cm for those with 90° cone angle, and 2.89 cm and 10 cm for those with 120° cone angle. In order to achieve various levels of roughness, the cone structures undergo a polishing process using abrasive paper and grinding and polishing equipment. Specifically, the $125 \mu m$ and $21.8 \mu m$ roughness structures are polished using 120-grit and 800-grit abrasive paper, respectively. The $0.2 \mu m$ structure, representing the relatively smooth surface in this study, is polished using a hemp wheel with a grit size of $0.2 \mu m$. In total, there are nine different aluminium conical substrates employed in the experiment, each with a distinct cone angle and surface roughness.

Due to the fact that for some materials, a varying surface roughness profile could affect its surface wettability, complicating direct observations of the effect of surface roughness on the droplets' impingement behaviour. Thus, in this experiment, a contact angle meter (CAM200, KSV Instruments) is employed to measure the apparent contact angle of the droplet on a flat aluminium substrate with varying levels of roughness. This instrument enables precise and repeatable contact angle measurements, providing insights into the wetting behaviour of the droplet on different surfaces. The results, presented in Figure 6-2, indicate that, in the context of this particular experiment, deviations in surface roughness did not exert a significant impact on the contact angles of the droplets.

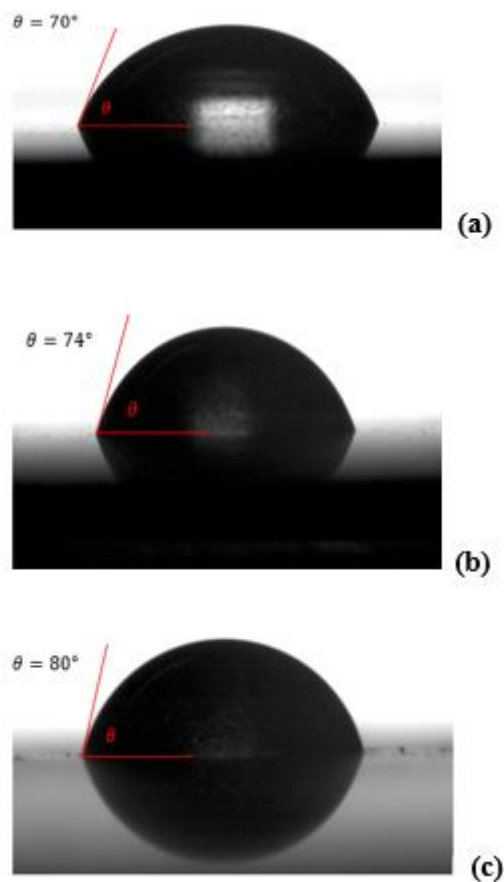


Fig. 6-2 Surface contact angle of water droplets on aluminium substrates (a) roughness = $0.2\mu\text{m}$ (b) roughness = $21.8\mu\text{m}$ (c) roughness = $125\mu\text{m}$

6.3 Results and Discussion

This section presents a series of images illustrating the impact of droplets on smooth cones and rough cones, considering different combinations of Weber numbers and cone angles. These images aim to capture the various stages of the droplet impingement process, including the initial impingement, spreading stage, retracting stage, relaxation stage, and equilibrium stage. The starting point of the impingement process is denoted as " $t = 0\text{ms}$ ", and the moment when the droplet makes contact with the cone tip is indicated by a dash-dot line.

6.3.1 Droplet impacting a relatively smooth conical structure

Fig. 6-3 to Fig. 6-5 depict the dynamic processes of droplets impacting a smooth aluminium conical structure (with a surface roughness value of $R_a=0.2\mu\text{m}$) featuring cone angles of 60° , 90° , and 120° , at various Weber numbers. These figures highlight the similarities observed during the spreading stage of droplets impacting different conical structures with varying cone angles. However, distinctions become apparent as the droplet transitions into the retracting stage. During the initial phase of impingement, the horizontal momentum fraction propels the droplet to spread downward along the cone's side, originating from the cone tip. This stage is primarily governed by inertial forces. At low Weber numbers ($We = 16$ as depicted in Fig. 6-3, case 1; Fig. 6-4, case 4; and Fig. 6-5, case 7), the droplet reaches its maximum spreading radius, denoted as R_{max} , at $t_{\text{max}}=17\text{ms}$ (case 1). Subsequently, two distinct boundaries emerge. The upper boundary arises due to the penetration of the water film, driven by the outward velocity vector at the cone tip. The lower boundary corresponds to the rim of the droplet lamella formed during spreading. Following the attainment of R_{max} , the rim liquid experiences slight retraction under the influence of capillary forces, with the velocity vector directed upward along the surface. Eventually, it merges with the descending upper boundary,

propelled downwards by gravity and kinetic energy. At $t = 30\text{ms}$ (case 1), an annulus is formed, which undergoes subsequent oscillation for a brief period. The liquid ultimately reaches a final equilibrium spreading radius, denoted as R_{equ} , which is slightly smaller than R_{max} . The distance between R_{equ} and R_{max} represents the retracting amplitude. During the spreading and retracting stages, the majority of the droplet's initial kinetic energy is dissipated. The remaining energy is further dissipated through oscillations during the relaxation stage. The contact line of the

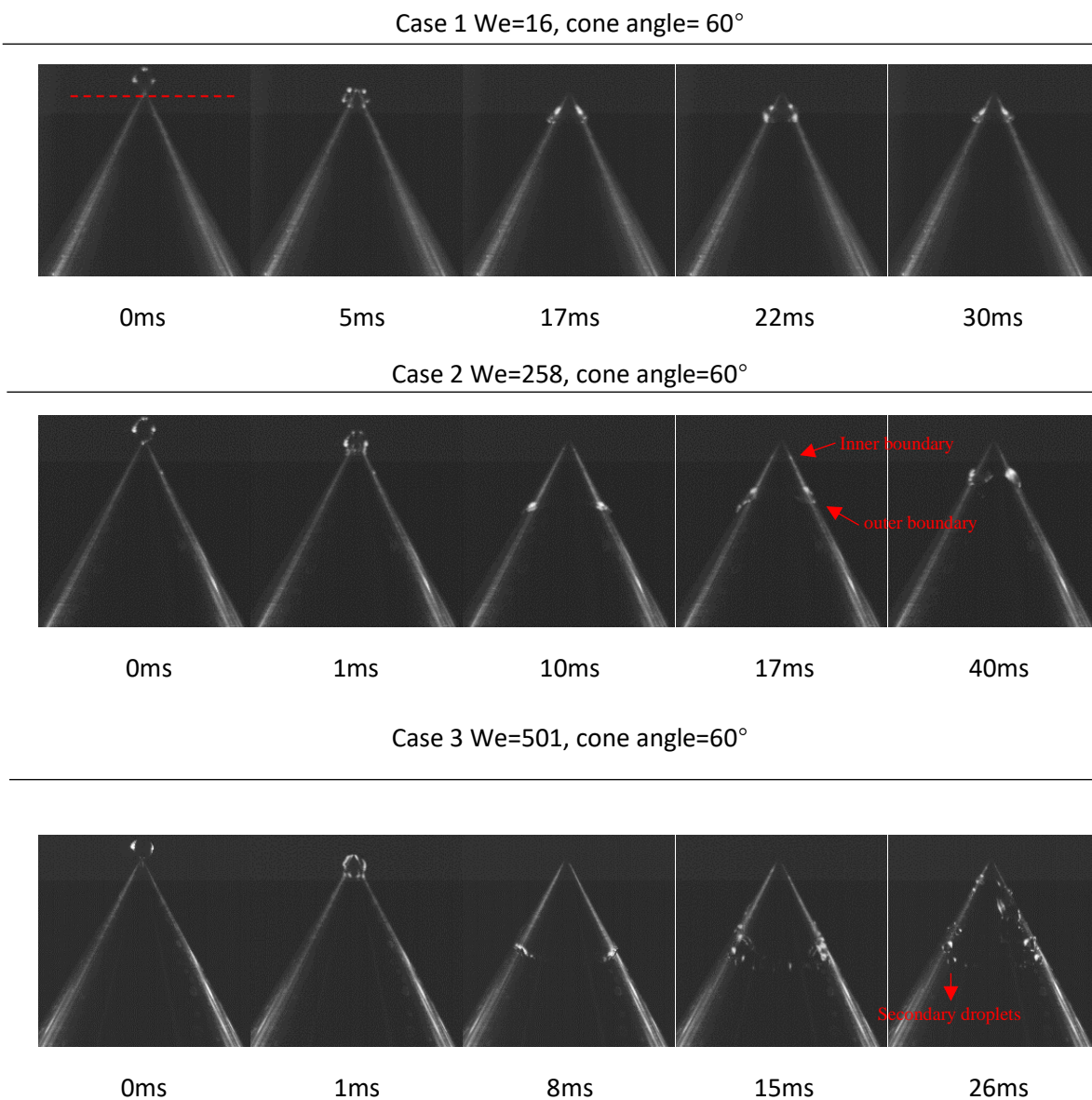


Fig. 6-3 Images of a water droplet impacting a relatively smooth aluminium conical structure with a 60° cone angle at different Weber numbers.

droplet advances during the spreading stage, recedes during the retracting stage, and eventually stabilises in the equilibrium state.

At higher Weber numbers ($We = 258$ as shown in Fig. 6-3, case 2; Fig. 6-4, case 5; and Fig. 6-5, case 8), R_{\max} increases and the spreading velocity becomes larger compared to the case with $We = 16$. This can be attributed to the larger initial vertical momentum resulting from the increased Weber number. Moreover, during the spreading stage in case 5 and case 8, "finger-like" perturbations can be observed at the rim of the droplet lamella. These perturbations are attributed to the Plateau-Rayleigh instability (P-R instability). The instability arises from the friction between the liquid stream and its surroundings, causing fluctuations in the local liquid volume. The surface tension amplifies these fluctuations, pushing the liquid from the pinching section (where the pressure is higher) to the bulging section (where the pressure is lower). Consequently, the rim of the droplet exhibits perturbations during spreading. After reaching R_{\max} , the retraction of the rim liquid becomes more pronounced compared to the case with $We = 16$. This enhanced retraction is a consequence of the increased capillary force. According to the Young-Laplace equation, the capillary pressure can be determined by:

$$p_c = \frac{2\sigma \cos \theta}{r_c} \quad (5.12)$$

where σ is surface tension, r_c represents the effective radius of the interface, θ is the wetting angle of the liquid on the surface. Therefore, the larger R_{\max} leads to an increased wetting area during spreading, resulting in a thinner rim of the droplet lamella. This, in turn, enhances the capillary force. In cases 2, 5, and 8 ($We = 258$), both the upper and lower boundaries are more noticeable compared to cases 1, 4, and 7 ($We = 16$). Subsequently, the upper and lower boundaries begin to retract until they merge into an annulus. In contrast to the oscillation observed at low Weber numbers, at higher Weber numbers, the annulus breaks into several

droplets ($t = 40\text{ms}$) during the relaxation stage. This difference can be attributed to the larger diameter and smaller thickness profile of the annulus at higher Weber numbers. The vertical component of the capillary force induced by surface tension is strong enough to overcome gravity and friction against the surface, resulting in the continuous retraction of the annulus. When the capillary pressure at the pinching section of the annulus surpasses the surface energy of the substrate, the annulus breaks, giving rise to the formation of secondary droplets. It is worth noting that R_{equ} is much smaller than R_{max} in cases with higher Weber numbers

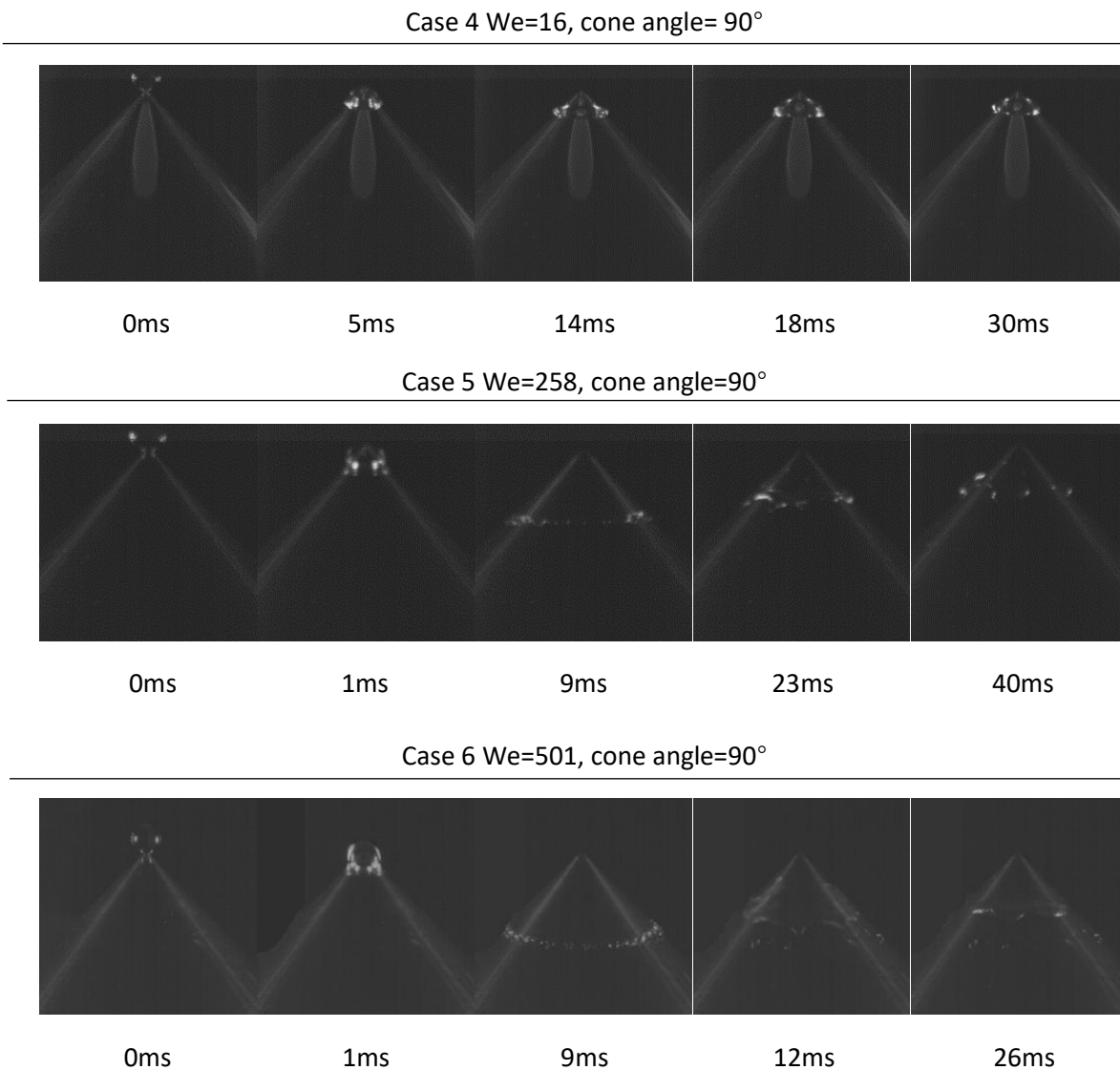
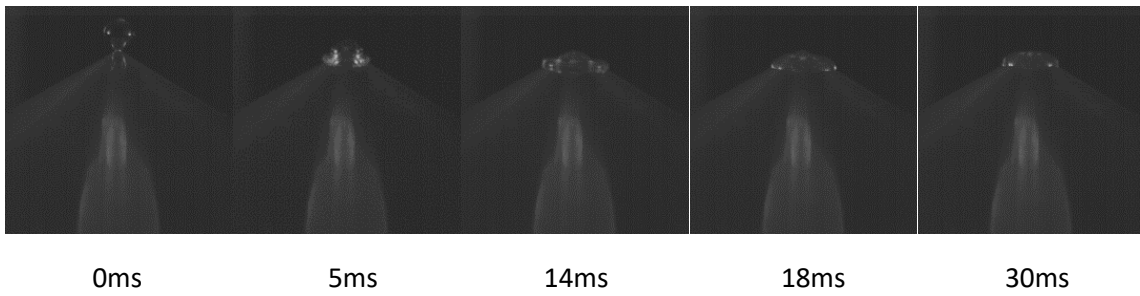


Fig. 6-4 Images of a water droplet impacting a relatively smooth aluminium conical structure with a 90° cone angle at different Weber numbers.

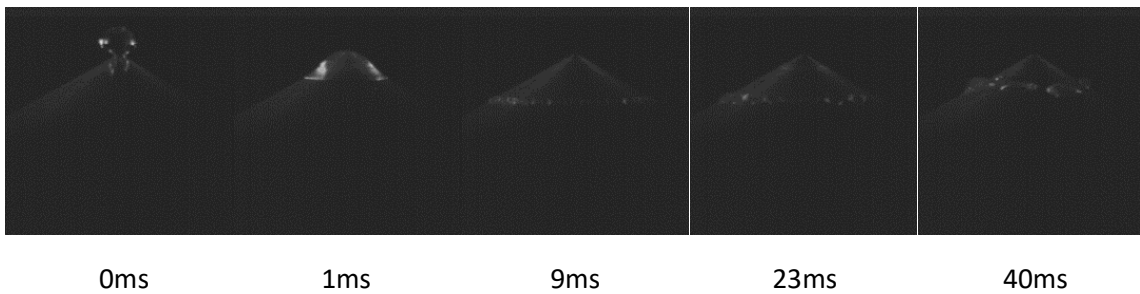
compared to cases with lower Weber numbers. This discrepancy is attributed to the intensified retraction stage observed at higher Weber numbers.

With a further increase in Weber number ($We = 501$, shown in Fig. 6-3, case 3; Fig. 6-4, case 6; and Fig. 6-5, case 9), the spreading rate and R_{\max} also increase. The droplet reaches R_{\max} at $t_{\max} = 8\text{ms}$, 9ms and 8ms for case 3, case 6 and case 9, respectively. Fingering perturbations can be observed along the outer rim of the spreading droplet lamella for all three cases. During the retracting stage, the rim liquid tends to retract back while the “fingers” are not able to be pulled back due to the smaller local surface tension. Consequently, these fingers pinch off from the outer rim, giving rise to the formation of secondary droplets. These secondary droplets settle along the maximum spreading contact line, as depicted in Fig. 6-3 case 3 ($t = 15\text{ms}$), Fig. 6-4 case 6 ($t = 12\text{ms}$), and Fig. 6-5 case 9 ($t = 12\text{ms}$). This phenomenon can be attributed to the P-R instability. As the droplet's rim moves downward along the surface, perturbations within the rim continue to grow, resulting in an increased variation in rim thickness. When the droplet approaches R_{\max} , the capillary force arising from surface tension starts to dominate over gravity and pulls the rim backward. However, at the bulging section of the annulus, the capillary force is not strong enough to counteract gravity, causing some liquid to detach from the rim and form secondary droplets. Subsequently, the remaining liquid within the rim retracts towards the cone tip in an attempt to reform an annulus. However, a significant portion of the liquid is transferred to the secondary droplets, and the retracted liquid breaks down into additional droplets randomly distributed between the maximum spreading contact line and the upper boundary at $t = 26\text{ms}$ in case 3. In case 6 and case 9, the rim liquid retracts and merges with the upper boundary, forming an annulus. Due to the larger diameter and smaller thickness profile of the annulus, it separates into several droplets instead of reaching an equilibrium state.

Case 7 We=16, cone angle= 120°



Case 8 We=258, cone angle=120°



Case 9 We=501, cone angle=120°

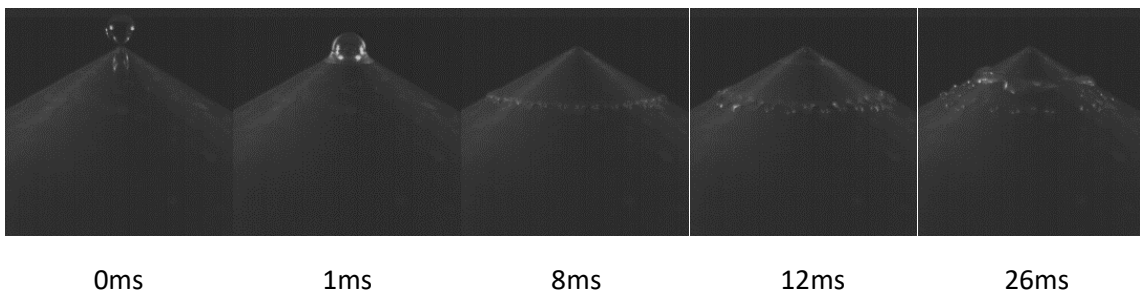


Fig. 6-5 Images of a water droplet impacting a relatively smooth aluminium conical structure with a 120° cone angle at different Weber numbers.

6.3.2 Droplet impacting a rough conical structure

Fig. 6-6 and Fig. 6-7 present images of a water droplet impacting a rough aluminium conical structure (cone angle = 60°) with varying surface roughness. These figures illustrate that the behavior of droplets impacting a rough surface is similar to that of droplets impacting a relatively smooth conical structure. The process of droplet impact includes the spreading state, retracting state, relaxation stage, and equilibrium state, which are observed in Case 10 to Case 15. Upon impact on the rough conical structure, the droplet spreads downward along the

hypotenuse of the cone from the cone tip, driven by inertial forces, until it reaches the maximum spreading radius R_{max} , which increases with Weber number. After which, the rim liquid retracts towards the cone tip and merges with the upper boundary of the liquid film formed by the penetration of the droplet. Subsequently, the rim liquid retracts towards the cone tip and merges with the upper boundary of the liquid film formed by the droplet penetration. In addition, secondary droplets can also be observed when the Weber number is 501 (Fig. 6-6, Case 12; Fig. 6-7, Case 15).

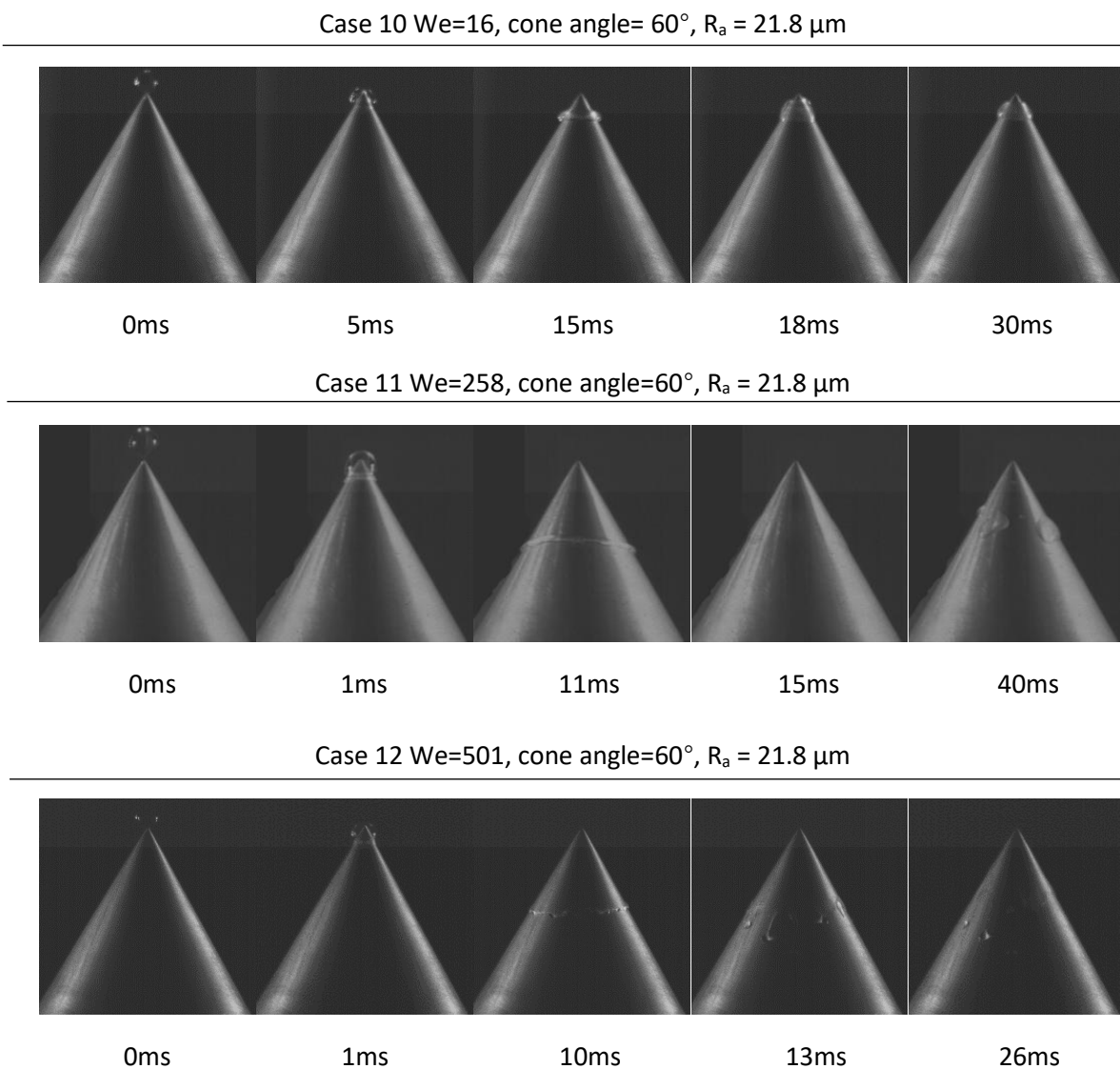
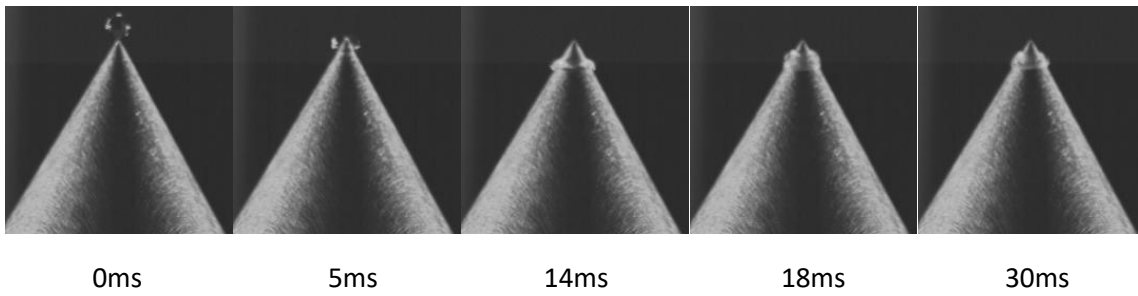
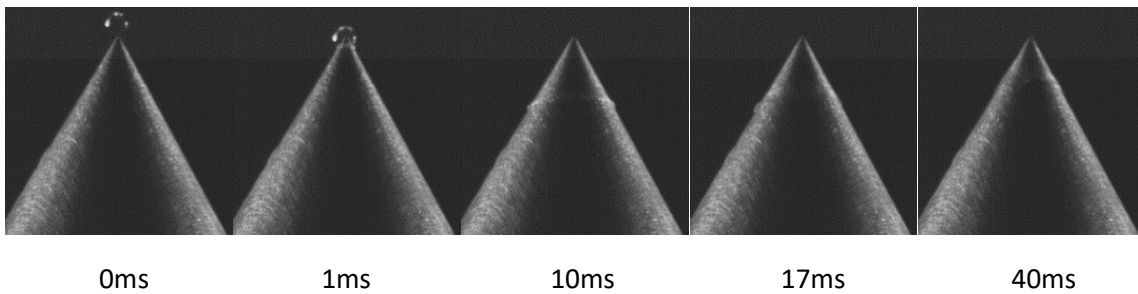


Fig. 6-6 Images of a water droplet impacting a rough aluminium conical structure with a 60° cone angle at different Weber numbers. (Roughness = 21.8 μm)

Case 13 We=16, cone angle= 60°, $R_a = 125 \mu\text{m}$



Case 14 We=258, cone angle=60°, $R_a = 125 \mu\text{m}$



Case 15 We=501, cone angle=60°, $R_a = 125 \mu\text{m}$

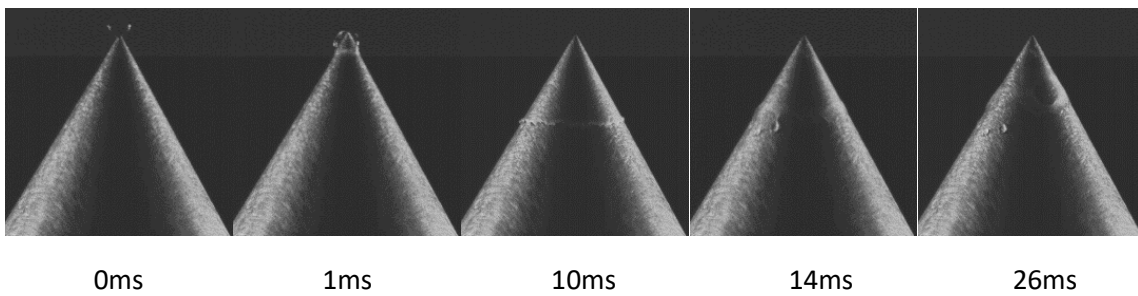
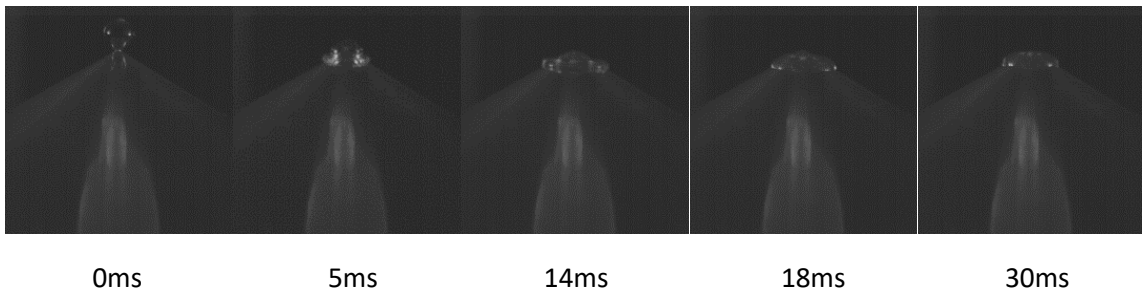


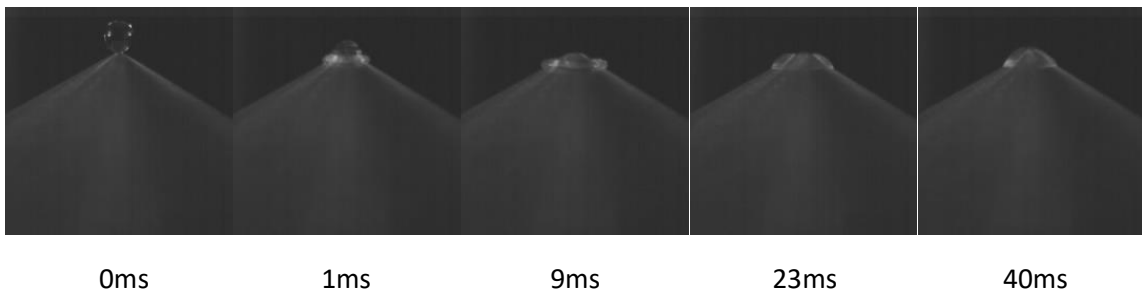
Fig. 6-7 Images of a water droplet impacting a rough aluminium conical structure with a 60° cone angle at different Weber numbers. (Roughness = 125 μm)

In particular, when the Weber number is 16 and the cone angle is 120°, the smooth conical structure (Case 7) does not have the liquid covering the cone tip at the final equilibrium stage, as depicted in Fig. 6-8. However, in the cases of roughness values of $R_a = 21.8\mu\text{m}$ (Case 16) and $R_a = 125\mu\text{m}$ (Case 17), the cone tip is covered by the liquid at the final equilibrium stage. This is because the maximum spreading factor decreases with increased roughness, making it more likely for the droplet to wrap around the cone tip.

Case 7 We=16, cone angle= 120°, $R_a = 0.2 \mu\text{m}$



Case 16 We=258, cone angle=60°, $R_a = 21.8 \mu\text{m}$



Case 17 We=501, cone angle=60°, $R_a = 125 \mu\text{m}$

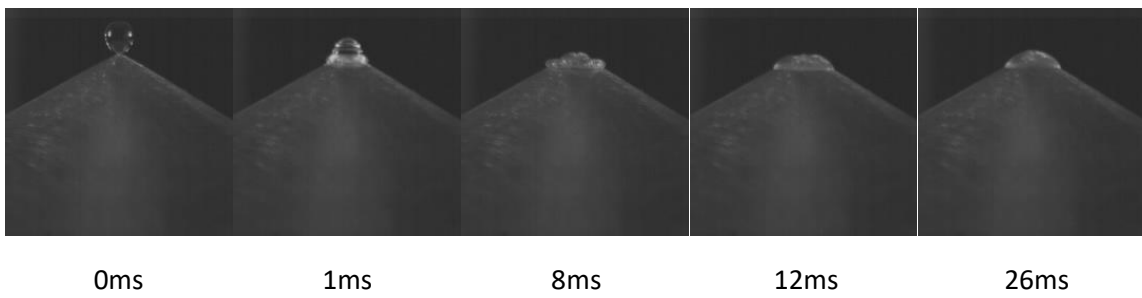


Fig. 6-8 Images of a water droplet impacting the conical aluminium structure with different surface roughness for $We = 16$ and cone angle = 120°

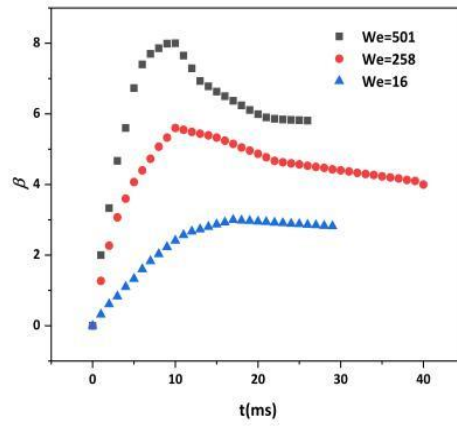
6.4 Impact Dynamic

6.4.1 Dynamic process analysis

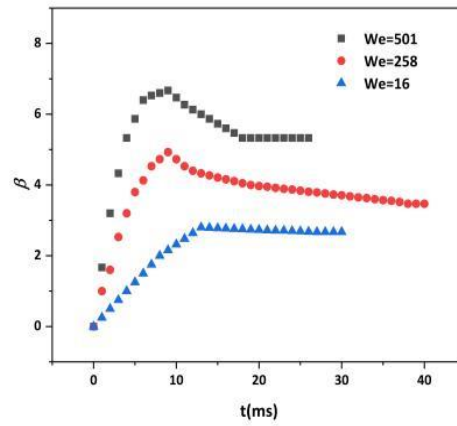
To further analyze the effect of Weber number, cone angle, and surface roughness on droplet impact dynamics, the differences between droplet impingement on smooth and rough conical structures may not be visually apparent. Therefore, in order to quantitatively assess these effects, the spreading factor β is measured as a function of the impact time t for all test cases. The spreading factor is defined as the ratio of the horizontal distance between the cone tip and the contact line to the initial radius of the droplet. The variation of the spreading factor represents the movement of the outer rim of the droplet lamella, excluding the secondary droplets. The presented figures depict the changes in the spreading factor during the spreading and retraction stages, as the variations in the relaxation and equilibrium stages are not as prominent.

Fig. 6-9 depicts the variation of the spreading factor β of droplets impacting a smooth conical structure with different cone angles. The effect of Weber numbers is analysed. With the increasing Weber number, the curve of β becomes steeper during the spreading stage, which indicates a larger spreading velocity. Meanwhile, β_{\max} increases significantly as We increases. As Fig. 6-9 (a) shows, when the cone angle is 60° , the largest maximum spreading factor ($\beta_{\max} = 8$) is obtained when $We = 501$, while the smallest one ($\beta_{\max} = 3$) is obtained when $We = 16$. The largest β_{\max} can be observed when $We = 501$ ($\beta_{\max} = 6.67$ for cone angle $= 90^\circ$, and $\beta_{\max} = 6$ for cone angle $= 120^\circ$) and the smallest β_{\max} is observed when $We = 16$ ($\beta_{\max} = 2.8$ for cone angle $= 90^\circ$, and $\beta_{\max} = 2.6$ for cone angle $= 120^\circ$) in Fig. 9 (b) and (c). Theoretical models proposed by Clanet et al., Roisman et al., and Yarin[245, 252, 253] have been used to predict and evaluate β_{\max} ; their results show that β_{\max} ranges from 1.25 to 5 when

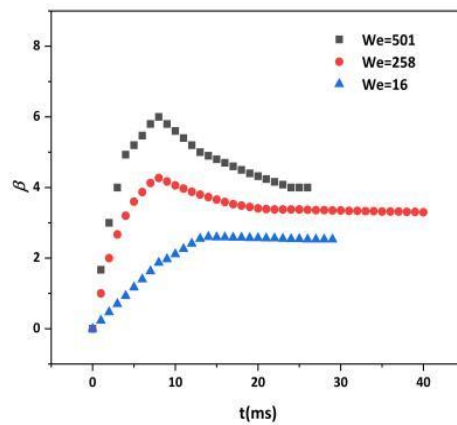
droplets impact a flat surface.



(a)



(b)



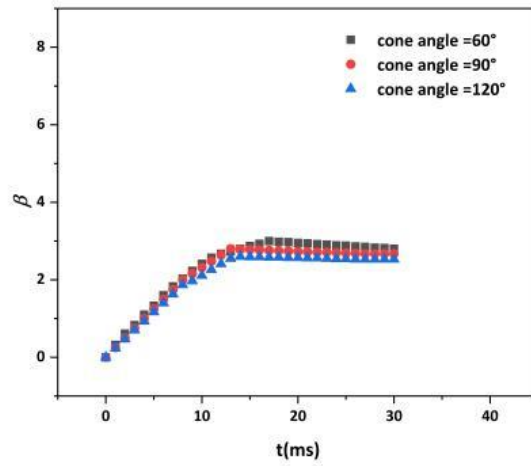
(c)

Fig. 6-9 The variation of droplet spreading factor of droplet impacts on a relatively smooth conical structure ($R_a = 0.2\mu\text{m}$) as a function of time for different conical structures with various cone angles; (a) cone angle = 60° , (b) cone angle = 90° , (c) cone angle = 120°

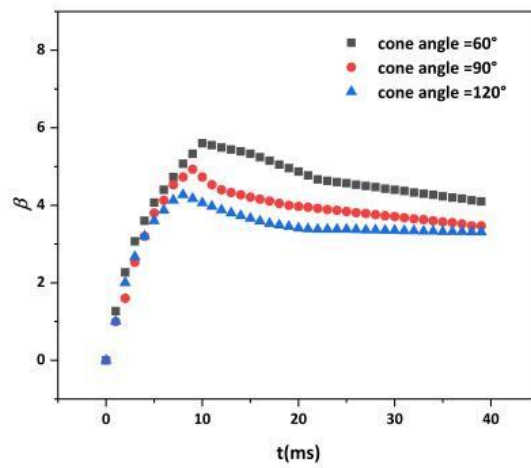
The observed larger β_{\max} when impacting a conical structure compared to a flat surface can be attributed to the reduced momentum loss during the impact. The geometry of the conical structure redirects the momentum of the droplet in a less steep manner compared to a flat surface, allowing the droplet to spread further. As a result, the maximum spreading factor is increased. This highlights the significant effect of the substrate's geometry on the droplet's spreading behaviour and could be projected to vast industrial applications.

When We reaches 501, droplet splashing occurs, leading to the detachment of secondary droplets from the outer rim of the lamella. This phenomenon is primarily attributed to the presence of P-R instability and the intensified inertial forces. Following the initial spreading stage, the extent of retraction experiences an increase in correlation with the escalating Weber number. In the case of conical structures with various cone angles at $We = 16$, the magnitude of retraction amplitude remains negligible during the retracting stage. However, as the Weber number rises to 258, the retraction amplitude expands within the range of 0.97 to 1.6. Subsequently, with a further increase in We to 501, the retraction amplitude encompasses values ranging from 2 to 2.19. The augmented retraction amplitude observed at higher Weber numbers can be attributed to the heightened capillary force arising from the diminished thickness of the lamella's rim. Furthermore, the occurrence of droplet splashing induces the formation of secondary droplets and leads to a reduction in the volume of the lamella's rim, consequently diminishing its thickness. As a result, the lighter weight and stronger capillary force of the lamella facilitate its ease of retraction, particularly in situations where the impact outcome involves splashing.

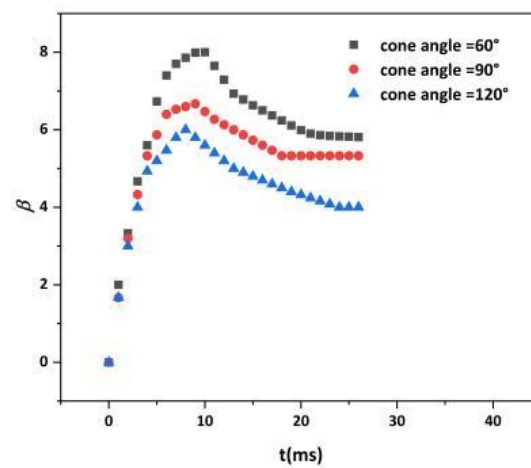
To further analyse the effect of cone angle, Fig. 6-9 is replotted and shown in Fig. 6-10. At low Weber number ($We = 16$, Fig. 6-10 (a)), the behavior of droplet spreading factors for all cases exhibits similarity. The values of β_{\max} are 3, 2.8 and 2.6 for cone angles of 60° ,



(a)



(b)

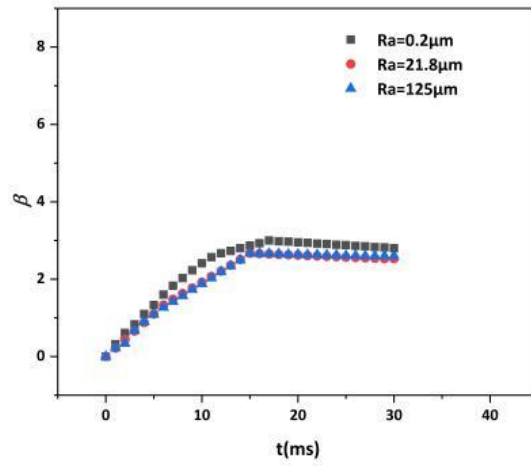


(c)

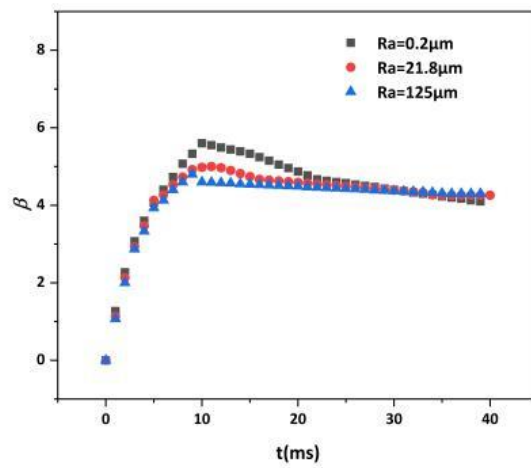
Fig. 6-10 The variation of droplet spreading factor of droplet impact on a relatively smooth conical structure ($R_o = 0.2\mu\text{m}$) with different Weber numbers as a function of time; (a) $We = 16$, (b) $We = 258$, (c) $We = 501$

90° and 120°, respectively. The effect of cone angle on β_{\max} is not prominently observed at low Weber numbers due to the smaller initial momentum. As the Weber number increases to 258 and 501 (Fig. 6-10 (b), (c)), the variation of droplet spreading factor becomes more pronounced with an increase in cone angle, indicating a higher spreading velocity. Furthermore, it is observed that the maximum spreading factor increases as the cone angle decreases. Specifically, for $We = 258$, the values of β_{\max} are 5.6, 4.93 and 4.27 for the cone angles of 60°, 90° and 120°, respectively. Similarly, for $We = 501$, the values of β_{\max} are 8, 6.67, and 6.13 for cone angles of 60°, 90°, and 120°, respectively. This observation can be attributed to the reduced kinetic energy loss associated with smaller cone angles, resulting in a higher inertia force driving the droplet spreading process.

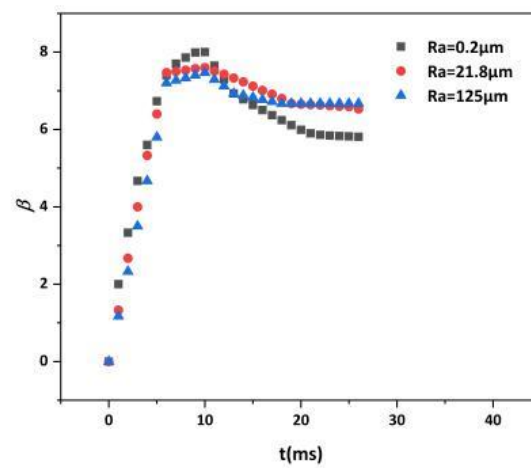
In Fig. 6-11, the influence of surface roughness R_a on the droplet spreading factor β is illustrated for water droplets impacting conical structures. The cone angle is set at 60°. The maximum spreading factor β_{\max} of droplets impacting a smooth surface is larger than those impacting a rough surface across all cases presented in Fig. 6-11. It is observed that an increase in surface roughness R_a leads to a reduction in the maximum spreading factor β_{\max} . Furthermore, when the Weber number reaches 258 and 501, the retraction amplitude is diminished on rough surfaces. This effect is evident in Figure 6-11(b) and (c), where the curve representing the evolution of the spreading factor for droplets impacting a smooth surface exhibits a steeper slope compared to those impacting a rough surface during the retracting stage. The presence of roughness increases friction, impeding the motion of the contact line and resulting in greater energy loss and a reduced maximum spreading factor. For the retracting stage, the retracting liquid needs to overcome the extract friction on a rough surface, leading to the decrease of retracting amplitude.



(a)



(b)



(c)

Fig. 6-11 The variation of droplet spreading factor of droplet impacts on a conical structure (cone angle = 60°) with different roughness and as a function of time; (a) $We = 16$, (b) $We = 258$, (c) $We = 501$

6.4.2 Splashing threshold

The critical Weber number We_c is the Weber number at which the droplet transits from spreading to splashing. Determining the splashing threshold is of significant importance in various applications like injection engines and spray cooling. Firstly, as the chamber walls of gasoline direct injection engines are impacted by spray, the splashing droplets could affect the mixture formation, resulting in the emission of unburned hydrocarbon. Secondly, splashing phenomena have implications for nucleation site generation and local film behaviors in spray cooling. The occurrence of splashing can enhance the heat transfer capabilities of the cooling process, influencing its overall efficiency and effectiveness[254].

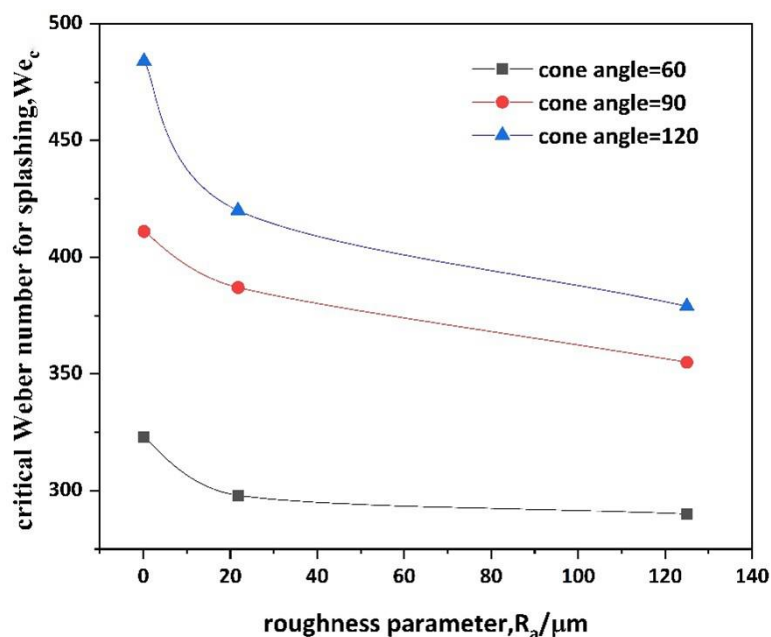


Fig. 6-12 The variation of the critical Weber number for splashing to the surface roughness for various cone structure with different cone angles.

Fig. 6-12 shows We_c for the transition from spreading to splashing as a function of the roughness parameter R_a . The influence of surface roughness and cone angle on splashing

behavior is significant, particularly when the surface roughness is low. The critical Weber number We_c decreases from 379 ~ 484 to 290 ~ 323 when the cone angle decreases from 120° to 60°. As the cone angle decreases from 120° to 60°. As discussed earlier, a smaller cone angle leads to less momentum loss upon droplet impingement, resulting in a larger maximum spreading factor β_{max} and higher inertia of the outer rim. These factors contribute to the enhanced generation of secondary droplets in conjunction with the P-R instability. Additionally, due to the inheritance of inertia from the liquid ring, higher inertia facilitates the detachment of liquid fingers, resulting in increased formation of secondary droplets.

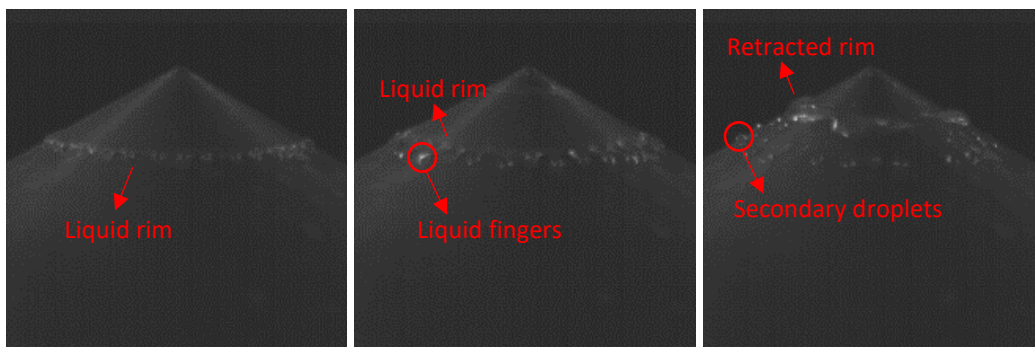


Fig. 6-13 Snapshot of the formation process of secondary droplets

Surface roughness plays a significant role in enhancing droplet splashing, and there are several reasons for this effect. One key reason is that surface roughness introduces additional friction forces during the retracting stage, hindering the retraction of the liquid fingers by the rim. As a result, the liquid fingers are more easily pinched off from the rim, leading to the formation of secondary droplets. Fig. 6-13 illustrates the formation of secondary droplets. When the rim of the lamella starts to retract towards the cone tip, liquid fingers face difficulty in overcoming the combined effects of friction and gravity. Consequently, these liquid fingers remain static, leading to the formation of secondary droplets. The presence of surface

roughness exacerbates this phenomenon, as the increased friction further impedes the retraction process and contributes to the formation of secondary droplets. Second, the surface roughness reduces the stability of the liquid lamella of the annulus, resulting in perturbations in the volume distribution along the liquid ring. This promotes the P-R instability and makes secondary droplets more easily generated.

6.5 Summary

The present study investigates the dynamics of droplet impingement and the evolution of droplet spreading on aluminium conical structures. A high-speed camera records the entire droplet impingement process on various conical structures. Upon contact with the cone tip, the droplet initially spreads downward along the cone's side until it reaches its maximum spreading factor. Subsequently, the rim liquid retracts towards the cone tip, forming an annular shape. To further analyse the dynamics of droplet impingement, the variation in the droplet spreading factor is utilised to quantify the spreading behaviours.

The maximum spreading factor is significantly influenced by the Weber number, surface roughness, and cone angle. An increase in the Weber number enhances the maximum spreading factor, whereas surface roughness and cone angle decrease it. Higher Weber numbers lead to a transition in the droplet impact outcome from spreading to splashing. This transition can be facilitated by augmenting surface roughness and reducing the cone angle. These findings contribute to an enhanced understanding of droplet impingement on conical structures with varying cone angles and surface roughness, providing fundamental insights for relevant applications such as spray cooling.

Chapter 7. Conclusion and outlook

7.1 Conclusion of the current work

In this thesis, a series of investigations were conducted to explore the kinetic and thermal dynamics of droplets utilising both numerical simulations and experimental techniques. Existing research on this topic has been concluded, and through two commonly seen phenomena, the evaporation and impingement of droplets, the mechanism of surface wettability, Marangoni flow, Leidenfrost effect and surface tension is investigated. The findings presented in this thesis significantly contribute to the comprehension of these fundamental aspects of droplets and offer insights into their potential applications.

Regarding the investigation on droplet evaporation under localised heating conditions, several noteworthy conclusions emerge:

- Droplets with small contact angles exhibit a prevailing influence of Marangoni flow, whereas those with larger contact angles are primarily governed by capillary flow.
- The overall evaporation rate increases as the heating source approaches the triple-phase contact line.
- On superhydrophobic surfaces, when the heat source is in proximity to the triple-phase contact line, droplets assume asymmetric shapes. Furthermore, such asymmetric heating conditions can induce droplet slippage on smooth surfaces.

In the numerical simulation of droplet impingement on conical structures, the following conclusions are drawn:

- Three different droplet behaviours are observed: deposition on the vertex, sliding down the hypotenuse and splashing. Increased gravitational force imparts greater kinetic energy upon impingement, making droplet rupture more likely than deposition. A hydrophilic surface reduces the likelihood of deposition, whereas higher temperatures and more hydrophobic surfaces enhance the probability of droplet detachment and subsequent splashing.
- When droplets rupture on the vertex, a weightlessness phenomenon is observed on hydrophobic surfaces due to more intense deformations compared to that on hydrophilic surfaces.
- In the Leidenfrost regime, droplets attain significantly higher velocities with reduced evaporation rates.

In the experimental analysis of droplet impact on a conical structure, the ensuing conclusions can be summarised as follows:

- The maximum spreading factor is augmented by an increase in the Weber number but impeded by heightened surface roughness and cone angle.
- A higher Weber number, rougher surface, and smaller cone angle expedite the transition from spreading to splashing.
- In instances of droplet splashing, the retracting stage is strengthened as a result of secondary droplet detachment.

7.2 Outlook for future work

Throughout the exploration of the mechanisms governing droplets, I have experienced a sense of exhilaration as this once enigmatic field unveils a captivating new realm of knowledge. However, within this process, the vast array of potential applications for droplets is revealed and the extensive research that lies ahead. In order to further enhance the understanding of this topic, the following avenues of investigation can be considered for future research:

- Chapter 4 introduced the intriguing phenomenon of droplet slipping, which holds great potential for applications such as drug delivery and contactless microfluidic devices. However, this phenomenon is inherently complex, as the direction of slipping is influenced by both the inner and outer flow of the droplet. To gain deeper insights into this phenomenon, further research analysing the flow field should be conducted.
- Replicating localised heating on a droplet in experimental settings poses significant challenges due to the small contact area of the droplet. Methods such as small-area heat conduction and laser heating have been considered, but an optimal solution has yet to be identified.
- Regrettably, due to the constraints of existing knowledge, the simulation of droplet impingement on conical structures has thus far been limited to a two-dimensional model. The absence of horizontal capillary force in this model prevents the accurate reproduction of the droplet's retracting stage. However, understanding the retracting stage is crucial for phenomena like rebounding, and gaining insights into the flow pattern within the liquid rim can provide a deeper comprehension of the impingement phenomenon. Thus, employing a three-dimensional model to investigate this topic is vital for future research endeavours.

- While the factors influencing the splashing threshold have been studied in the experimental analysis of droplet impingement on conical structures, more systematic quantitative research is necessary to establish precise threshold criteria for each variation. Furthermore, establishing an empirical correlation can facilitate the control of impingement behaviour.

References

- [1] R. J. Good, "Contact angle, wetting, and adhesion: a critical review," *Journal of Adhesion Science and Technology*, vol. 6, no. 12, pp. 1269-1302, 1992/01/01 1992.
- [2] T. Young, "III. An essay on the cohesion of fluids," *Philosophical Transactions of the Royal Society of London*, vol. 95, pp. 65-87, 1805.
- [3] A. DUPRÉ and P. DUPRÉ, *Théorie mécanique de la Chaleur. Par ... A. D. ... (Partie expérimentale en commun avec ... P. Dupré.)*. 1869.
- [4] D. Brutin, "1.1 Theoretical Concepts: Equilibrium Surface Thermodynamics," in *Droplet Wetting and Evaporation - From Pure to Complex Fluids*: Elsevier.
- [5] J.-W. Song and L.-W. Fan, "Temperature dependence of the contact angle of water: A review of research progress, theoretical understanding, and implications for boiling heat transfer," *Advances in Colloid and Interface Science*, vol. 288, p. 102339, 2021/02/01/ 2021.
- [6] M. S. Bell and A. Borhan, "A Volume-Corrected Wenzel Model," (in eng), *ACS Omega*, vol. 5, no. 15, pp. 8875-8884, Apr 21 2020.
- [7] U. Ceyhan, A. Tiktaş, and M. Özdoğan, "Pinning and depinning of Wenzel-state droplets around inclined steps," *Colloid and Interface Science Communications*, vol. 35, p. 100238, 2020/03/01/ 2020.
- [8] A. Lafuma and D. Quéré, "Superhydrophobic states," *Nature Materials*, vol. 2, no. 7, pp. 457-460, 2003/07/01 2003.
- [9] Q. S. Zheng, Y. Yu, and Z. H. Zhao, "Effects of Hydraulic Pressure on the Stability and Transition of Wetting Modes of Superhydrophobic Surfaces," *Langmuir*, vol. 21, no. 26, pp. 12207-12212, 2005/12/01 2005.
- [10] G. Wang, Z.-h. Jia, and H.-n. Yang, "Stability of a water droplet on micropillared hydrophobic surfaces," *Colloid and Polymer Science*, vol. 294, no. 5, pp. 851-858, 2016/05/01 2016.
- [11] X. Chen, R. Ma, J. Li, C. Hao, W. Guo, B. L. Luk, S. C. Li, S. Yao, and Z. Wang, "Evaporation of Droplets on Superhydrophobic Surfaces: Surface Roughness and Small Droplet Size Effects," *Physical Review Letters*, vol. 109, no. 11, p. 116101, 09/10/ 2012.
- [12] M. Jiang, Y. Wang, F. Liu, H. Du, Y. Li, H. Zhang, S. To, S. Wang, C. Pan, J. Yu, D. Quéré, and Z. Wang, "Inhibiting the Leidenfrost effect above 1,000 °C for sustained thermal cooling," *Nature*, vol. 601, no. 7894, pp. 568-572, 2022/01/01 2022.
- [13] M. Li, C. Huber, W. Tao, and J. Wei, "Study on nucleation position and wetting state for dropwise condensation on rough structures with different wettability using multiphase lattice Boltzmann method," *International Journal of Heat and Mass Transfer*, vol. 131, pp. 96-100, 2019/03/01/ 2019.
- [14] M. Gross, F. Varnik, and D. Raabe, "Fall and rise of small droplets on rough hydrophobic substrates," *Europhysics Letters*, vol. 88, no. 2, p. 26002, 2009/11/04 2009.
- [15] H. Kim, M. Y. Ha, and J. Jang, "Effects of Surface Geometry on the Wenzel-to-Cassie Transition of a Water Droplet," *Bulletin of the Korean Chemical Society*, vol. 38, no. 9, pp. 1010-1015, 2017.
- [16] J. T. Delaney, P. J. Smith, and U. S. Schubert, "Inkjet printing of proteins," *Soft Matter*, 10.1039/B909878J vol. 5, no. 24, pp. 4866-4877, 2009.
- [17] V. Mironov, T. Boland, T. Trusk, G. Forgacs, and R. R. Markwald, "Organ printing: computer-aided jet-based 3D tissue engineering," *Trends in Biotechnology*, vol. 21, no. 4, pp. 157-161, 2003/04/01/ 2003.
- [18] S. Chandra and J. Mostaghimi, "Spray Impingement Fundamentals," in *Metal Sprays and Spray Deposition*, H. Henein, V. Uhlenwinkel, and U. Fritsching, Eds. Cham: Springer International Publishing, 2017, pp. 177-220.
- [19] R. Bhardwaj, J. P. Longtin, and D. Attinger, "Interfacial temperature measurements, high-speed visualization and finite-element simulations of droplet impact and evaporation on a

- solid surface," *International Journal of Heat and Mass Transfer*, vol. 53, no. 19, pp. 3733-3744, 2010/09/01/ 2010.
- [20] A. G. Pautsch and T. A. Shedd, "Spray impingement cooling with single- and multiple-nozzle arrays. Part I: Heat transfer data using FC-72," *International Journal of Heat and Mass Transfer*, vol. 48, no. 15, pp. 3167-3175, 2005/07/01/ 2005.
- [21] J. B. Andrews and M. B. Robinson, "CONTAINERLESS LOW GRAVITY PROCESSING OF HYPERMONOTECTIC GOLD-RHODIUM ALLOYS," *Journal of Metals*, vol. 37, no. 11, pp. A68-A68, 1985.
- [22] C. D. Ahrberg, J. W. Choi, and B. G. Chung, "Droplet-based synthesis of homogeneous magnetic iron oxide nanoparticles," *Beilstein Journal of Nanotechnology*, vol. 9, pp. 2413-2420, 2018.
- [23] V. B. Varma, R. G. Wu, Z. P. Wang, and R. V. Ramanujan, "Magnetic Janus particles synthesized using droplet micro-magnetofluidic techniques for protein detection," *Lab on a Chip*, 10.1039/C7LC00830A vol. 17, no. 20, pp. 3514-3525, 2017.
- [24] M. V. Johnson, G. S. Zhu, S. K. Aggarwal, and S. S. Goldsborough, "Droplet evaporation characteristics due to wet compression under RCM conditions," *International Journal of Heat and Mass Transfer*, vol. 53, no. 5, pp. 1100-1111, 2010/02/01/ 2010.
- [25] R. T. Imaoka and W. A. Sirignano, "Vaporization and combustion in three-dimensional droplet arrays," *Proceedings of the Combustion Institute*, vol. 30, no. 2, pp. 1981-1989, 2005/01/01/ 2005.
- [26] C. C. Tseng and R. Viskanta, "Enhancement of water droplet evaporation by radiation absorption," *Fire Safety Journal*, vol. 41, no. 3, pp. 236-247, 2006/04/01/ 2006.
- [27] G. Miliuskas, S. Sinkunas, and G. Miliuskas, "Evaporation and condensing augmentation of water droplets in flue gas," *International Journal of Heat and Mass Transfer - INT J HEAT MASS TRANSFER*, vol. 53, pp. 1220-1230, 02/01 2010.
- [28] V. Dugas, J. Broutin, and E. Souteyrand, "Droplet Evaporation Study Applied to DNA Chip Manufacturing," *Langmuir*, vol. 21, no. 20, pp. 9130-9136, 2005/09/01 2005.
- [29] W. Guan, L. Chen, T. D. Rane, and T.-H. Wang, "Droplet Digital Enzyme-Linked Oligonucleotide Hybridization Assay for Absolute RNA Quantification," (in eng), *Scientific reports*, vol. 5, pp. 13795-13795, 2015.
- [30] T.-S. Wong, T.-H. Chen, X. Shen, and C.-M. Ho, "Nanochromatography Driven by the Coffee Ring Effect," *Analytical Chemistry*, vol. 83, no. 6, pp. 1871-1873, 2011/03/15 2011.
- [31] D. Brutin, B. Sobac, B. Loquet, and J. Sampol, "Pattern formation in drying drops of blood," *Journal of Fluid Mechanics*, vol. 667, pp. 85-95, 2011.
- [32] N. M. Kovalchuk, A. Trybala, and V. M. Starov, "Evaporation of sessile droplets," *Current Opinion in Colloid & Interface Science*, vol. 19, no. 4, pp. 336-342, 2014/08/01/ 2014.
- [33] H. Y. Erbil, "Evaporation of pure liquid sessile and spherical suspended drops: A review," *Advances in Colloid and Interface Science*, vol. 170, no. 1, pp. 67-86, 2012/01/15/ 2012.
- [34] C. W. Everitt, "Maxwell's Scientific Papers," (in eng), *Applied optics*, vol. 6, no. 4, pp. 639-46, Apr 1 1967.
- [35] I. Langmuir, "The Evaporation of Small Spheres," *Physical Review*, vol. 12, no. 5, pp. 368-370, 11/01/ 1918.
- [36] R. G. Picknett and R. Bexon, "The evaporation of sessile or pendant drops in still air," *Journal of Colloid and Interface Science*, vol. 61, no. 2, pp. 336-350, 1977/09/01/ 1977.
- [37] H. Hu and R. G. Larson, "Evaporation of a sessile droplet on a substrate," *The Journal of Physical Chemistry B*, vol. 106, no. 6, pp. 1334-1344, 2002.
- [38] R. D. Deegan, O. Bakajin, T. F. Dupont, G. Huber, S. R. Nagel, and T. A. Witten, "Contact line deposits in an evaporating drop," *Physical Review E - Statistical Physics, Plasmas, Fluids, and Related Interdisciplinary Topics*, Article vol. 62, no. 1 B, pp. 756-765, 2000.

- [39] R. Bhardwaj, X. Fang, and D. Attinger, "Pattern formation during the evaporation of a colloidal nanoliter drop: A numerical and experimental study," *New Journal of Physics*, Article vol. 11, 2009, Art no. 075020.
- [40] S. Moosman and G. M. Homsy, "Evaporating menisci of wetting fluids," *Journal of Colloid And Interface Science*, Article vol. 73, no. 1, pp. 212-223, 1980.
- [41] M. Potash Jr and P. C. Wayner Jr, "Evaporation from a two-dimensional extended meniscus," *International Journal of Heat and Mass Transfer*, Article vol. 15, no. 10, pp. 1851-1863, 1972.
- [42] V. Starov, "Static contact angle hysteresis on smooth, homogeneous solid substrates," *Colloid and Polymer Science*, Article vol. 291, no. 2, pp. 261-270, 2013.
- [43] V. Starov and K. Sefiane, "On evaporation rate and interfacial temperature of volatile sessile drops," *Colloids and Surfaces A: Physicochemical and Engineering Aspects*, Article vol. 333, no. 1-3, pp. 170-174, 2009.
- [44] M. Lopes, "The influence of substrate's elasticity and thermal properties on drop evaporation," 2013.
- [45] M. D. Doganci, B. U. Sesli, and H. Y. Erbil, "Diffusion-controlled evaporation of sodium dodecyl sulfate solution drops placed on a hydrophobic substrate," *Journal of Colloid and Interface Science*, vol. 362, no. 2, pp. 524-531, 2011/10/15/ 2011.
- [46] M. E. R. Shanahan and C. Bourgès, "Effects of evaporation on contact angles on polymer surfaces," *International Journal of Adhesion and Adhesives*, vol. 14, no. 3, pp. 201-205, 1994/07/01/ 1994.
- [47] A. Amini and G. M. Homsy, "Evaporation of liquid droplets on solid substrates. I. Flat substrate with pinned or moving contact line," *Physical Review Fluids*, vol. 2, no. 4, p. 043603, 04/20/ 2017.
- [48] T.-S. Lin, Y.-H. Zeng, R.-Y. Tsay, and S.-Y. Lin, "Roughness-induced strong pinning for drops evaporating from polymeric surfaces," *Journal of the Taiwan Institute of Chemical Engineers*, vol. 62, pp. 54-59, 2016/05/01/ 2016.
- [49] H. Y. Erbil, G. McHale, and M. I. Newton, "Drop Evaporation on Solid Surfaces: Constant Contact Angle Mode," *Langmuir*, vol. 18, no. 7, pp. 2636-2641, 2002/04/01 2002.
- [50] E. Y. Gatapova, A. A. Semenov, D. V. Zaitsev, and O. A. Kabov, "Evaporation of a sessile water drop on a heated surface with controlled wettability," *Colloids and Surfaces A: Physicochemical and Engineering Aspects*, vol. 441, pp. 776-785, 2014/01/20/ 2014.
- [51] H. Gelderblom, C. Diddens, and A. Marin, "Evaporation-driven liquid flow in sessile droplets," *Soft Matter*, 10.1039/D2SM00931E vol. 18, no. 45, pp. 8535-8553, 2022.
- [52] S. Abbott, "Printing Science: Principles and Practice," *Ipswich.[Google Scholar]*, 2018.
- [53] D. Zang, S. Tarafdar, Y. Y. Tarasevich, M. Dutta Choudhury, and T. Dutta, "Evaporation of a Droplet: From physics to applications," *Physics Reports*, vol. 804, pp. 1-56, 2019/04/29/ 2019.
- [54] J. R. A. Pearson, "On convection cells induced by surface tension," *Journal of Fluid Mechanics*, vol. 4, no. 5, pp. 489-500, 1958.
- [55] R. T. van Gaalen, H. M. A. Wijshoff, J. G. M. Kuerten, and C. Diddens, "Competition between thermal and surfactant-induced Marangoni flow in evaporating sessile droplets," *Journal of Colloid and Interface Science*, vol. 622, pp. 892-903, 2022/09/15/ 2022.
- [56] J. G. Leidenfrost, "On the fixation of water in diverse fire," *International Journal of Heat and Mass Transfer*, vol. 9, no. 11, pp. 1153-1166, 1966/11/01/ 1966.
- [57] D. Brutin, "7.1 Introduction," in *Droplet Wetting and Evaporation - From Pure to Complex Fluids*: Elsevier.
- [58] H. Linke, B. J. Alemán, L. D. Melling, M. J. Taormina, M. J. Francis, C. C. Dow-Hygelund, V. Narayanan, R. P. Taylor, and A. Stout, "Self-Propelled Leidenfrost Droplets," *Physical Review Letters*, vol. 96, no. 15, p. 154502, 04/19/ 2006.
- [59] J. D. Bernardin and I. Mudawar, "The Leidenfrost Point: Experimental Study and Assessment of Existing Models," *Journal of Heat Transfer*, vol. 121, no. 4, pp. 894-903, 1999.

- [60] D. Arnaldo del Cerro, Á. G. Marín, G. R. B. E. Römer, B. Pathiraj, D. Lohse, and A. J. Huis in 't Veld, "Leidenfrost Point Reduction on Micropatterned Metallic Surfaces," *Langmuir*, vol. 28, no. 42, pp. 15106-15110, 2012/10/23 2012.
- [61] J. T. Ok, E. Lopez-Oña, D. E. Nikitopoulos, H. Wong, and S. Park, "Propulsion of droplets on micro- and sub-micron ratchet surfaces in the Leidenfrost temperature regime," *Microfluidics and Nanofluidics*, vol. 10, no. 5, pp. 1045-1054, 2011/05/01 2011.
- [62] T. R. Cousins, R. E. Goldstein, J. W. Jaworski, and A. I. Pesci, "A ratchet trap for Leidenfrost drops," *Journal of Fluid Mechanics*, vol. 696, pp. 215-227, 2012.
- [63] D. Quéré, "Leidenfrost Dynamics," *Annual Review of Fluid Mechanics*, vol. 45, no. 1, pp. 197-215, 2013.
- [64] A.-L. Biance, C. Clanet, and D. Quéré, "Leidenfrost drops," *Physics of Fluids*, vol. 15, no. 6, pp. 1632-1637, 2003/06/01 2003.
- [65] G. Bleiker and E. Specht, "Film evaporation of drops of different shape above a horizontal plate," *International Journal of Thermal Sciences*, vol. 46, no. 9, pp. 835-841, 2007/09/01/ 2007.
- [66] A. M. Worthington and R. B. Clifton, "XXVIII. On the forms assumed by drops of liquids falling vertically on a horizontal plate," *Proceedings of the Royal Society of London*, vol. 25, no. 171-178, pp. 261-272, 1877.
- [67] Y. C. Liu, T. Farouk, A. J. Savas, F. L. Dryer, and C. Thomas Avedisian, "On the spherically symmetrical combustion of methyl decanoate droplets and comparisons with detailed numerical modeling," *Combustion and Flame*, vol. 160, no. 3, pp. 641-655, 2013/03/01/ 2013.
- [68] C. Cen, H. Wu, C.-f. Lee, F. Liu, and Y. Li, "Experimental investigation on the characteristic of jet break-up for butanol droplet impacting onto a heated surface in the film boiling regime," *International Journal of Heat and Mass Transfer*, vol. 123, pp. 129-136, 2018/08/01/ 2018.
- [69] D. D. Hall and I. Mudawar, "Experimental and numerical study of quenching complex-shaped metallic alloys with multiple, overlapping sprays," *International Journal of Heat and Mass Transfer*, vol. 38, no. 7, pp. 1201-1216, 1995/05/01/ 1995.
- [70] M. Pasandideh-Fard, V. Pershin, S. Chandra, and J. Mostaghimi, "Splat shapes in a thermal spray coating process: Simulations and experiments," *Journal of Thermal Spray Technology*, vol. 11, no. 2, pp. 206-217, 2002/06/01 2002.
- [71] M. Rein, "Phenomena of liquid drop impact on solid and liquid surfaces," *Fluid Dynamics Research*, vol. 12, no. 2, pp. 61-93, 1993/08 1993.
- [72] C. W. Kang and H. W. Ng, "Splat morphology and spreading behavior due to oblique impact of droplets onto substrates in plasma spray coating process," *Surface and Coatings Technology*, vol. 200, no. 18, pp. 5462-5477, 2006/05/08/ 2006.
- [73] Y. Zhibin, Z. Rui, D. Fei, W. Teck Neng, T. Kok Chuan, C. Kok Fah, C. Poh Keong, and C. Yong Sheng, "Spray Cooling," in *Two Phase Flow, Phase Change and Numerical Modeling*, A. Amimul, Ed. Rijeka: IntechOpen, 2011, p. Ch. 13.
- [74] B. Horacek, K. T. Kiger, and J. Kim, "Single nozzle spray cooling heat transfer mechanisms," *International Journal of Heat and Mass Transfer*, vol. 48, no. 8, pp. 1425-1438, 2005/04/01/ 2005.
- [75] J. D. Benthier, J. D. Pelaez-Restrepo, C. Stanley, and G. Rosengarten, "Heat transfer during multiple droplet impingement and spray cooling: Review and prospects for enhanced surfaces," *International Journal of Heat and Mass Transfer*, vol. 178, p. 121587, 2021/10/01/ 2021.
- [76] I. V. Roisman, J. Breitenbach, and C. Tropea, "Thermal atomisation of a liquid drop after impact onto a hot substrate," *Journal of Fluid Mechanics*, vol. 842, pp. 87-101, 2018.
- [77] J. Kim, "Spray cooling heat transfer: The state of the art," *International Journal of Heat and Fluid Flow*, vol. 28, pp. 753-767, 08/01 2007.

- [78] J. S. Eow and M. Ghadiri, "Electrostatic enhancement of coalescence of water droplets in oil: a review of the technology," *Chemical Engineering Journal*, vol. 85, no. 2, pp. 357-368, 2002/01/28/ 2002.
- [79] H. Wijshoff, "Drop dynamics in the inkjet printing process," *Current Opinion in Colloid & Interface Science*, vol. 36, pp. 20-27, 2018/07/01/ 2018.
- [80] R. Daly, T. S. Harrington, G. D. Martin, and I. M. Hutchings, "Inkjet printing for pharmaceuticals – A review of research and manufacturing," *International Journal of Pharmaceutics*, vol. 494, no. 2, pp. 554-567, 2015/10/30/ 2015.
- [81] H.-J. Chang, M. H. Tsai, and W.-S. Hwang, "The simulation of micro droplet behavior of molten lead-free solder in inkjet printing process and its experimental validation," *Applied Mathematical Modelling*, vol. 36, no. 7, pp. 3067-3079, 2012/07/01/ 2012.
- [82] J. Léopoldès, A. Dupuis, D. G. Bucknall, and J. M. Yeomans, "Jetting Micron-Scale Droplets onto Chemically Heterogeneous Surfaces," *Langmuir*, vol. 19, no. 23, pp. 9818-9822, 2003/11/01 2003.
- [83] G. Liang and I. Mudawar, "Review of drop impact on heated walls," *International Journal of Heat and Mass Transfer*, vol. 106, pp. 103-126, 2017/03/01/ 2017.
- [84] S. T. Thoroddsen, T. G. Etoh, and K. Takehara, "High-Speed Imaging of Drops and Bubbles," *Annual Review of Fluid Mechanics*, vol. 40, no. 1, pp. 257-285, 2008.
- [85] R. Rioboo, C. Tropea, and M. Marengo, "OUTCOMES FROM A DROP IMPACT ON SOLID SURFACES," vol. 11, no. 2, p. 12, 2001-04-01 2001.
- [86] N. Laan, K. G. de Bruin, D. Bartolo, C. Josserand, and D. Bonn, "Maximum Diameter of Impacting Liquid Droplets," *Physical Review Applied*, vol. 2, no. 4, p. 044018, 10/30/ 2014.
- [87] S. Moghtadernejad, C. Lee, and M. Jadidi, "An Introduction of Droplet Impact Dynamics to Engineering Students," *Fluids*, vol. 5, no. 3, p. 107, 2020.
- [88] C. Josserand and S. T. Thoroddsen, "Drop Impact on a Solid Surface," *Annual Review of Fluid Mechanics*, vol. 48, no. 1, pp. 365-391, 2016/01/03 2016.
- [89] H. Chen, W.-l. Cheng, Y.-h. Peng, and L.-j. Jiang, "Dynamic Leidenfrost temperature increase of impacting droplets containing high-alcohol surfactant," *International Journal of Heat and Mass Transfer*, vol. 118, pp. 1160-1168, 2018/03/01/ 2018.
- [90] S. Yun, "Impact dynamics of egg-shaped drops on a solid surface for suppression of the bounce magnitude," *International Journal of Heat and Mass Transfer*, vol. 127, pp. 172-178, 2018/12/01/ 2018.
- [91] S. Jung, M. K. Tiwari, N. V. Doan, and D. Poulikakos, "Mechanism of supercooled droplet freezing on surfaces," *Nature Communications*, vol. 3, no. 1, p. 615, 2012/01/10 2012.
- [92] Y. Pan, K. Shi, X. Duan, and G. F. Naterer, "Experimental investigation of water droplet impact and freezing on micropatterned stainless steel surfaces with varying wettabilities," *International Journal of Heat and Mass Transfer*, vol. 129, pp. 953-964, 2019/02/01/ 2019.
- [93] J. Breitenbach, I. V. Roisman, and C. Tropea, "Drop collision with a hot, dry solid substrate: Heat transfer during nucleate boiling," *Physical Review Fluids*, vol. 2, no. 7, p. 074301, 07/07/ 2017.
- [94] R. Simhadri Rajesh, P. T. Naveen, K. Krishnakumar, and S. Kumar Ranjith, "Dynamics of single droplet impact on cylindrically-curved superheated surfaces," *Experimental Thermal and Fluid Science*, vol. 101, pp. 251-262, 2019/01/01/ 2019.
- [95] C. Tang, M. Qin, X. Weng, X. Zhang, P. Zhang, J. Li, and Z. Huang, "Dynamics of droplet impact on solid surface with different roughness," *International Journal of Multiphase Flow*, vol. 96, pp. 56-69, 2017/11/01/ 2017.
- [96] C. D. Stow and M. G. Hadfield, "An experimental investigation of fluid flow resulting from the impact of a water drop with an unyielding dry surface," *Proceedings of the Royal Society of London. A. Mathematical and Physical Sciences*, vol. 373, pp. 419 - 441, 1981.

- [97] R. K. Singh, P. D. Hodgson, N. Sen, and S. Das, "Effect of Surface Roughness on Hydrodynamic Characteristics of an Impinging Droplet," *Langmuir*, vol. 37, no. 10, pp. 3038-3048, 2021/03/16 2021.
- [98] M. A. Quetzeri-Santiago, A. A. Castrejón-Pita, and J. R. Castrejón-Pita, "The Effect of Surface Roughness on the Contact Line and Splashing Dynamics of Impacting Droplets," *Scientific Reports*, vol. 9, no. 1, p. 15030, 2019/10/21 2019.
- [99] I. V. Roisman, A. Lembach, and C. Tropea, "Drop splashing induced by target roughness and porosity: The size plays no role," *Advances in Colloid and Interface Science*, vol. 222, pp. 615-621, 2015/08/01/ 2015.
- [100] Q. Wang, X. Lin, Y. Lin, J. Ma, J. Xiao, Y. Wu, and J. Wang, "Effects of surface roughness on splashing characteristics of large droplets with digital inline holographic imaging," *Cold Regions Science and Technology*, vol. 191, p. 103373, 2021/11/01/ 2021.
- [101] R. D. Groot and P. B. Warren, "Dissipative particle dynamics: Bridging the gap between atomistic and mesoscopic simulation," *The Journal of Chemical Physics*, vol. 107, no. 11, pp. 4423-4435, 1997.
- [102] S. Wolfram, "Cellular automaton fluids 1: Basic theory," *Journal of Statistical Physics*, vol. 45, no. 3, pp. 471-526, 1986/11/01 1986.
- [103] G. R. McNamara and G. Zanetti, "Use of the Boltzmann Equation to Simulate Lattice-Gas Automata," *Physical Review Letters*, vol. 61, no. 20, pp. 2332-2335, 11/14/ 1988.
- [104] F. J. Higuera and J. Jiménez, "Boltzmann Approach to Lattice Gas Simulations," *Europhysics Letters*, vol. 9, no. 7, p. 663, 1989/08/01 1989.
- [105] F. J. Higuera, S. Succi, and R. Benzi, "Lattice Gas Dynamics with Enhanced Collisions," *Europhysics Letters*, vol. 9, no. 4, p. 345, 1989/06/15 1989.
- [106] S. Chen, H. Chen, D. Martnez, and W. Matthaeus, "Lattice Boltzmann model for simulation of magnetohydrodynamics," *Physical Review Letters*, vol. 67, no. 27, pp. 3776-3779, 12/30/ 1991.
- [107] J. M. V. A. Koelman, "A Simple Lattice Boltzmann Scheme for Navier-Stokes Fluid Flow," *Europhysics Letters*, vol. 15, no. 6, p. 603, 1991/07/15 1991.
- [108] Y. H. Qian, D. D. Humières, and P. Lallemand, "Lattice BGK Models for Navier-Stokes Equation," *Europhysics Letters*, vol. 17, no. 6, p. 479, 1992/02/01 1992.
- [109] D. D'Humieres, "Generalized Lattice-Boltzmann Equations," in *18th International symposium, Rarefied gas dynamics*, Washington, DC, Vancouver; Canada, 1994, vol. 159: AIAA;, pp. 450-458.
- [110] P. Nathen, D. Gaudlitz, M. J. Krause, and N. A. Adams, "On the Stability and Accuracy of the BGK, MRT and RLB Boltzmann Schemes for the Simulation of Turbulent Flows," (in english), *Communications in computational physics*, vol. 23, no. 2, pp. 846-876, 2018// 2018.
- [111] S. Chen and G. D. Doolen, "LATTICE BOLTZMANN METHOD FOR FLUID FLOWS," *Annual Review of Fluid Mechanics*, vol. 30, no. 1, pp. 329-364, 1998.
- [112] X. Shan, "Simulation of Rayleigh-Bénard convection using a lattice Boltzmann method," *Physical Review E*, vol. 55, no. 3, pp. 2780-2788, 03/01/ 1997.
- [113] X. He, S. Chen, and G. D. Doolen, "A Novel Thermal Model for the Lattice Boltzmann Method in Incompressible Limit," *Journal of Computational Physics*, vol. 146, no. 1, pp. 282-300, 1998/10/10/ 1998.
- [114] A. J. C. Ladd, "Numerical simulations of particulate suspensions via a discretized Boltzmann equation. Part 1. Theoretical foundation," *Journal of Fluid Mechanics*, vol. 271, pp. 285-309, 1994.
- [115] A. J. C. Ladd, "Numerical simulations of particulate suspensions via a discretized Boltzmann equation. Part 2. Numerical results," *Journal of Fluid Mechanics*, vol. 271, pp. 311-339, 1994.
- [116] C. K. Aidun and Y. Lu, "Lattice Boltzmann simulation of solid particles suspended in fluid," *Journal of Statistical Physics*, vol. 81, no. 1, pp. 49-61, 1995/10/01 1995.

- [117] S. Succi, G. Bella, and F. Papetti, "Lattice Kinetic Theory for Numerical Combustion," *Journal of Scientific Computing*, vol. 12, no. 4, pp. 395-408, 1997/12/01 1997.
- [118] D. Zhang, S. Li, and Y. Li, "Pore-scale investigation on the effect of gas-liquid phase separation on reactive flow in a horizontal rough fracture using the lattice Boltzmann method," *Chemical Engineering Science*, vol. 236, p. 116483, 2021/06/08/ 2021.
- [119] S. Ponce Dawson, S. Chen, and G. D. Doolen, "Lattice Boltzmann computations for reaction-diffusion equations," *The Journal of Chemical Physics*, vol. 98, no. 2, pp. 1514-1523, 1993/01/15 1993.
- [120] P. Lallemand and L. S. Luo, "Theory of the lattice boltzmann method: dispersion, dissipation, isotropy, galilean invariance, and stability," (in eng), *Physical review. E, Statistical physics, plasmas, fluids, and related interdisciplinary topics*, vol. 61, no. 6 Pt A, pp. 6546-62, Jun 2000.
- [121] R. Benzi, S. Succi, and M. Vergassola, "The lattice Boltzmann equation: theory and applications," *Physics Reports*, vol. 222, no. 3, pp. 145-197, 1992/12/01/ 1992.
- [122] S. Chen, D. Martínez, and R. Mei, "On boundary conditions in lattice Boltzmann methods," *Physics of Fluids*, vol. 8, no. 9, pp. 2527-2536, 1996/09/01 1996.
- [123] Z. Guo and C. G. Zheng, "Theory and Applications of Lattice Boltzmann Method," *Science, Beijing*, 01/01 2009.
- [124] D. P. Ziegler, "Boundary conditions for lattice Boltzmann simulations," *Journal of Statistical Physics*, vol. 71, no. 5, pp. 1171-1177, 1993/06/01 1993.
- [125] D. R. Noble, J. G. Georgiadis, and R. O. Buckius, "Direct assessment of lattice Boltzmann hydrodynamics and boundary conditions for recirculating flows," *Journal of Statistical Physics*, vol. 81, no. 1, pp. 17-33, 1995/10/01 1995.
- [126] Q. Zou and X. He, "On pressure and velocity boundary conditions for the lattice Boltzmann BGK model," *Physics of Fluids*, vol. 9, no. 6, pp. 1591-1598, 1997/06/01 1997.
- [127] T. Inamuro, M. Yoshino, and F. Ogino, "A non-slip boundary condition for lattice Boltzmann simulations," *Physics of Fluids*, vol. 7, no. 12, pp. 2928-2930, 1995/12/01 1995.
- [128] C. Q. Tong, Y. L. He, G. H. Tang, Y. Wang, and Y. W. Liu, "MASS MODIFIED OUTLET BOUNDARY FOR A FULLY DEVELOPED FLOW IN THE LATTICE BOLTZMANN EQUATION," *International Journal of Modern Physics C*, vol. 18, no. 07, pp. 1209-1221, 2007/07/01 2007.
- [129] S. Chen, D. Martinez, and R. Mei, "On boundary conditions in lattice Boltzmann methods," *Physics of fluids*, vol. 8, no. 9, pp. 2527-2536, 1996.
- [130] Z.-L. Guo, C.-G. Zheng, and B.-C. Shi, "Non-equilibrium extrapolation method for velocity and pressure boundary conditions in the lattice Boltzmann method," *Chinese Physics*, vol. 11, no. 4, p. 366, 2002/04/01 2002.
- [131] O. Filippova and D. Hänel, "Grid Refinement for Lattice-BGK Models," *Journal of Computational Physics*, vol. 147, no. 1, pp. 219-228, 1998/11/20/ 1998.
- [132] M. h. Bouzidi, M. Firdaouss, and P. Lallemand, "Momentum transfer of a Boltzmann-lattice fluid with boundaries," *Physics of Fluids*, vol. 13, no. 11, pp. 3452-3459, 2001/11/01 2001.
- [133] P. Lallemand and L.-S. Luo, "Lattice Boltzmann method for moving boundaries," *Journal of Computational Physics*, vol. 184, no. 2, pp. 406-421, 2003/01/20/ 2003.
- [134] C. W. Hirt and B. D. Nichols, "Volume of fluid (VOF) method for the dynamics of free boundaries," *Journal of Computational Physics*, vol. 39, no. 1, pp. 201-225, 1981/01/01/ 1981.
- [135] S. Osher and J. A. Sethian, "Fronts propagating with curvature-dependent speed: Algorithms based on Hamilton-Jacobi formulations," *Journal of Computational Physics*, vol. 79, no. 1, pp. 12-49, 1988/11/01/ 1988.
- [136] H. Liu, A. J. Valocchi, and Q. Kang, "Three-dimensional lattice Boltzmann model for immiscible two-phase flow simulations," *Physical Review E*, vol. 85, no. 4, p. 046309, 04/20/ 2012.
- [137] R. Scardovelli and S. Zaleski, "DIRECT NUMERICAL SIMULATION OF FREE-SURFACE AND INTERFACIAL FLOW," *Annual Review of Fluid Mechanics*, vol. 31, no. 1, pp. 567-603, 1999.

- [138] D. H. Rothman and J. M. Keller, "Immiscible cellular-automaton fluids," *Journal of Statistical Physics*, vol. 52, no. 3, pp. 1119-1127, 1988/08/01 1988.
- [139] Q. Li, K. H. Luo, Q. J. Kang, Y. L. He, Q. Chen, and Q. Liu, "Lattice Boltzmann methods for multiphase flow and phase-change heat transfer," *Progress in Energy and Combustion Science*, vol. 52, pp. 62-105, 2016/02/01/ 2016.
- [140] A. K. Gunstensen, D. H. Rothman, S. Zaleski, and G. Zanetti, "Lattice Boltzmann model of immiscible fluids," *Physical Review A*, vol. 43, no. 8, pp. 4320-4327, 04/01/ 1991.
- [141] X. Shan and H. Chen, "Lattice Boltzmann model for simulating flows with multiple phases and components," *Physical Review E*, Article vol. 47, no. 3, pp. 1815-1819, 1993.
- [142] M. R. Swift, W. R. Osborn, and J. M. Yeomans, "Lattice Boltzmann Simulation of Nonideal Fluids," *Physical Review Letters*, vol. 75, no. 5, pp. 830-833, 07/31/ 1995.
- [143] M. R. Swift, E. Orlandini, W. R. Osborn, and J. M. Yeomans, "Lattice Boltzmann simulations of liquid-gas and binary fluid systems," *Physical Review E*, vol. 54, no. 5, pp. 5041-5052, 11/01/ 1996.
- [144] A. Kuzmin, A. A. Mohamad, and S. Succi, "MULTI-RELAXATION TIME LATTICE BOLTZMANN MODEL FOR MULTIPHASE FLOWS," *International Journal of Modern Physics C*, vol. 19, no. 06, pp. 875-902, 2008/06/01 2008.
- [145] X. He, S. Chen, and R. Zhang, "A Lattice Boltzmann Scheme for Incompressible Multiphase Flow and Its Application in Simulation of Rayleigh–Taylor Instability," *Journal of Computational Physics*, vol. 152, no. 2, pp. 642-663, 1999/07/01/ 1999.
- [146] D. Jacqmin, "Calculation of Two-Phase Navier–Stokes Flows Using Phase-Field Modeling," *Journal of Computational Physics*, vol. 155, no. 1, pp. 96-127, 1999/10/10/ 1999.
- [147] X. He and G. D. Doolen, "Thermodynamic Foundations of Kinetic Theory and Lattice Boltzmann Models for Multiphase Flows," *Journal of Statistical Physics*, vol. 107, no. 1, pp. 309-328, 2002/04/01 2002.
- [148] Q. Li, K. H. Luo, and X. J. Li, "Forcing scheme in pseudopotential lattice Boltzmann model for multiphase flows," *Physical Review E*, vol. 86, no. 1, p. 016709, 07/23/ 2012.
- [149] S. Khajepour, J. Wen, and B. Chen, "Multipseudopotential interaction: A solution for thermodynamic inconsistency in pseudopotential lattice Boltzmann models," *Physical Review E*, vol. 91, no. 2, p. 023301, 02/02/ 2015.
- [150] J. S. Orr, J. F. Powers, and H. Q. Yang, "Lattice Boltzmann method for spacecraft propellant slosh simulation," in *2015 American Astronautical Society (AAS) Guidance, Navigation, and Control Conference*, 2015, no. M15-4348.
- [151] Q. Kang, D. Zhang, and S. Chen, "Immiscible displacement in a channel: simulations of fingering in two dimensions," *Advances in Water Resources*, vol. 27, no. 1, pp. 13-22, 2004/01/01/ 2004.
- [152] R. Zhang, X. He, G. Doolen, and S. Chen, "Surface tension effects on two-dimensional two-phase Kelvin–Helmholtz instabilities," *Advances in Water Resources*, vol. 24, no. 3, pp. 461-478, 2001/02/01/ 2001.
- [153] Q. Li, Y. Xing, and R. Huang, "Equations of state in multiphase lattice Boltzmann method revisited," *Physical Review E*, vol. 107, no. 1, p. 015301, 01/06/ 2023.
- [154] P. Yuan and L. Schaefer, "Equations of state in a lattice Boltzmann model," *Physics of Fluids*, vol. 18, no. 4, p. 042101, 2006/04/01 2006.
- [155] X. He, X. Shan, and G. D. Doolen, "Discrete Boltzmann equation model for nonideal gases," *Physical Review E*, vol. 57, no. 1, pp. R13-R16, 01/01/ 1998.
- [156] N. S. Martys, X. Shan, and H. Chen, "Evaluation of the external force term in the discrete Boltzmann equation," *Physical Review E*, vol. 58, no. 5, pp. 6855-6857, 11/01/ 1998.
- [157] A. L. Kupershtokh and D. A. Medvedev, "Lattice Boltzmann equation method in electrohydrodynamic problems," *Journal of Electrostatics*, vol. 64, no. 7, pp. 581-585, 2006/07/01/ 2006.

- [158] X. Shan and G. Doolen, "Multicomponent lattice-Boltzmann model with interparticle interaction," *Journal of Statistical Physics*, vol. 81, no. 1, pp. 379-393, 1995/10/01 1995.
- [159] Z. Guo, C. Zheng, and B. Shi, "Discrete lattice effects on the forcing term in the lattice Boltzmann method," *Physical Review E*, vol. 65, no. 4, p. 046308, 04/10/ 2002.
- [160] S. Gong and P. Cheng, "Numerical investigation of droplet motion and coalescence by an improved lattice Boltzmann model for phase transitions and multiphase flows," *Computers & Fluids*, vol. 53, pp. 93-104, 2012/01/15/ 2012.
- [161] N. S. Martys and H. Chen, "Simulation of multicomponent fluids in complex three-dimensional geometries by the lattice Boltzmann method," (in eng), *Physical review. E, Statistical physics, plasmas, fluids, and related interdisciplinary topics*, vol. 53, no. 1, pp. 743-750, Jan 1996.
- [162] Q. Kang, D. Zhang, and S. Chen, "Displacement of a two-dimensional immiscible droplet in a channel," *Physics of Fluids*, vol. 14, no. 9, pp. 3203-3214, 2002/09/01 2002.
- [163] P. Raïskinmäki, A. Koponen, J. Merikoski, and J. Timonen, "Spreading dynamics of three-dimensional droplets by the lattice-Boltzmann method," *Computational Materials Science*, vol. 18, no. 1, pp. 7-12, 2000/07/01/ 2000.
- [164] R. Benzi, L. Biferale, M. Sbragaglia, S. Succi, and F. Toschi, "Mesoscopic modeling of a two-phase flow in the presence of boundaries: The contact angle," *Physical Review E*, vol. 74, no. 2, p. 021509, 08/30/ 2006.
- [165] C. E. Colosqui, M. E. Kavousanakis, A. G. Papathanasiou, and I. G. Kevrekidis, "Mesoscopic model for microscale hydrodynamics and interfacial phenomena: Slip, films, and contact-angle hysteresis," *Physical Review E*, vol. 87, no. 1, p. 013302, 01/03/ 2013.
- [166] Q. Li, K. H. Luo, Q. J. Kang, and Q. Chen, "Contact angles in the pseudopotential lattice Boltzmann modeling of wetting," *Physical Review E*, vol. 90, no. 5, p. 053301, 11/03/ 2014.
- [167] B. Han and H. Meng, "Lattice Boltzmann simulation of liquid water transport in turning regions of serpentine gas channels in proton exchange membrane fuel cells," *Journal of Power Sources*, vol. 217, pp. 268-279, 2012/11/01/ 2012.
- [168] Y. Gao, X. Zhang, P. Rama, R. Chen, H. Ostadi, and K. Jiang, "Lattice Boltzmann simulation of water and gas flow in porous gas diffusion layers in fuel cells reconstructed from microtomography," *Computers & Mathematics with Applications*, vol. 65, no. 6, pp. 891-900, 2013/03/01/ 2013.
- [169] G. R. Molaeimanesh and M. H. Akbari, "Impact of PTFE distribution on the removal of liquid water from a PEMFC electrode by lattice Boltzmann method," *International Journal of Hydrogen Energy*, vol. 39, no. 16, pp. 8401-8409, 2014/05/27/ 2014.
- [170] K. N. Kim, J. H. Kang, S. G. Lee, J. H. Nam, and C.-J. Kim, "Lattice Boltzmann simulation of liquid water transport in microporous and gas diffusion layers of polymer electrolyte membrane fuel cells," *Journal of Power Sources*, vol. 278, pp. 703-717, 2015/03/15/ 2015.
- [171] S. G. Lee, D. H. Jeon, B. M. Kim, J. H. Kang, and C.-J. Kim, "Lattice Boltzmann Simulation for Electrolyte Transport in Porous Electrode of Lithium Ion Batteries," *Journal of The Electrochemical Society*, vol. 160, no. 4, p. H258, 2013/02/26 2013.
- [172] T. Inamuro, S. Tajima, and F. Ogino, "Lattice Boltzmann simulation of droplet collision dynamics," *International Journal of Heat and Mass Transfer*, vol. 47, no. 21, pp. 4649-4657, 2004/10/01/ 2004.
- [173] S. Mukherjee and J. Abraham, "Investigations of drop impact on dry walls with a lattice-Boltzmann model," *Journal of Colloid and Interface Science*, vol. 312, no. 2, pp. 341-354, 2007/08/15/ 2007.
- [174] A. Gupta and R. Kumar, "Droplet impingement and breakup on a dry surface," *Computers & Fluids*, vol. 39, no. 9, pp. 1696-1703, 2010/10/01/ 2010.
- [175] W. Zhou, D. Loney, A. G. Fedorov, F. L. Degertekin, and D. W. Rosen, "Lattice Boltzmann simulations of multiple-droplet interaction dynamics," (in eng), *Physical review. E, Statistical, nonlinear, and soft matter physics*, vol. 89, no. 3, p. 033311, Mar 2014.

- [176] A. Jaramillo, V. Pessoa Mapelli, and L. Cabezas-Gómez, "Pseudopotential Lattice Boltzmann Method for boiling heat transfer: A mesh refinement procedure," *Applied Thermal Engineering*, vol. 213, p. 118705, 2022/08/01/ 2022.
- [177] W. Gong, Y. Y. Yan, S. Chen, and E. Wright, "A modified phase change pseudopotential lattice Boltzmann model," *International Journal of Heat and Mass Transfer*, vol. 125, pp. 323-329, 2018/10/01/ 2018.
- [178] Y. Yu, Q. Li, C. Q. Zhou, P. Zhou, and H. J. Yan, "Investigation of droplet evaporation on heterogeneous surfaces using a three-dimensional thermal multiphase lattice Boltzmann model," *Applied Thermal Engineering*, vol. 127, pp. 1346-1354, 2017/12/25/ 2017.
- [179] F. Qin, L. Del Carro, A. Mazloomi Moqaddam, Q. Kang, T. Brunschwiler, D. Derome, and J. Carmeliet, "Study of non-isothermal liquid evaporation in synthetic micro-pore structures with hybrid lattice Boltzmann model," *Journal of Fluid Mechanics*, vol. 866, pp. 33-60, 2019.
- [180] A. S. Joshi and Y. Sun, "Wetting dynamics and particle deposition for an evaporating colloidal drop: A lattice Boltzmann study," *Physical Review E*, vol. 82, no. 4, p. 041401, 10/07/ 2010.
- [181] W. Miller and S. Succi, "A Lattice Boltzmann Model for Anisotropic Crystal Growth from Melt," *Journal of Statistical Physics*, vol. 107, no. 1, pp. 173-186, 2002/04/01 2002.
- [182] D. Medvedev and K. Kassner, "Lattice Boltzmann scheme for crystal growth in external flows," (in eng), *Physical review. E, Statistical, nonlinear, and soft matter physics*, vol. 72, no. 5 Pt 2, p. 056703, Nov 2005.
- [183] S. Chakraborty and D. Chatterjee, "An enthalpy-based hybrid lattice-Boltzmann method for modelling solid-liquid phase transition in the presence of convective transport," *Journal of Fluid Mechanics*, vol. 592, pp. 155-175, 2007.
- [184] D. Gao and Z. Chen, "Lattice Boltzmann simulation of natural convection dominated melting in a rectangular cavity filled with porous media," *International Journal of Thermal Sciences*, vol. 50, no. 4, pp. 493-501, 2011/04/01/ 2011.
- [185] C. Huber, A. Parmigiani, B. Chopard, M. Manga, and O. Bachmann, "Lattice Boltzmann model for melting with natural convection," *International Journal of Heat and Fluid Flow*, vol. 29, no. 5, pp. 1469-1480, 2008/10/01/ 2008.
- [186] F. Qin, A. Mazloomi Moqaddam, Q. Kang, D. Derome, and J. Carmeliet, "Entropic multiple-relaxation-time multirange pseudopotential lattice Boltzmann model for two-phase flow," *Physics of Fluids*, vol. 30, no. 3, p. 032104, 2018/03/01 2018.
- [187] W. Xiong and P. Cheng, "3D lattice Boltzmann simulation for a saturated liquid droplet at low Ohnesorge numbers impact and breakup on a solid surface surrounded by a saturated vapor," *Computers & Fluids*, vol. 168, pp. 130-143, 2018/05/30/ 2018.
- [188] P. Yuan and L. Schaefer, "A Thermal Lattice Boltzmann Two-Phase Flow Model and Its Application to Heat Transfer Problems—Part 1. Theoretical Foundation," *Journal of Fluids Engineering*, vol. 128, no. 1, pp. 142-150, 2005.
- [189] P. L. Bhatnagar, E. P. Gross, and M. Krook, "A Model for Collision Processes in Gases. I. Small Amplitude Processes in Charged and Neutral One-Component Systems," *Physical Review*, vol. 94, no. 3, pp. 511-525, 05/01/ 1954.
- [190] C. Zhang, P. Cheng, and W. J. Minkowycz, "Lattice Boltzmann simulation of forced condensation flow on a horizontal cold surface in the presence of a non-condensable gas," *International Journal of Heat and Mass Transfer*, vol. 115, pp. 500-512, 2017/12/01/ 2017.
- [191] J. Zhang, H. Chen, Y. Zhou, and G. Cao, "Simulation on the process of single bubble floating and colliding oil droplet based on improved three-component pseudo-potential Boltzmann method," *Journal of Petroleum Science and Engineering*, vol. 198, p. 108119, 2021/03/01/ 2021.
- [192] S. Gong and P. Cheng, "A lattice Boltzmann method for simulation of liquid-vapor phase-change heat transfer," *International Journal of Heat and Mass Transfer*, vol. 55, no. 17, pp. 4923-4927, 2012/08/01/ 2012.

- [193] C. Zhang and P. Cheng, "Mesoscale simulations of boiling curves and boiling hysteresis under constant wall temperature and constant heat flux conditions," *International Journal of Heat and Mass Transfer*, vol. 110, pp. 319-329, 2017/07/01/ 2017.
- [194] A. Hu, L. Li, S. Chen, Q. Liao, and J. Zeng, "On equations of state in pseudo-potential multiphase lattice Boltzmann model with large density ratio," *International Journal of Heat and Mass Transfer*, vol. 67, pp. 159-163, 2013/12/01/ 2013.
- [195] X. Xu and J. Luo, "Marangoni flow in an evaporating water droplet," *Applied Physics Letters*, vol. 91, no. 12, p. 124102, 2007/09/17 2007.
- [196] H. Hu and R. G. Larson, "Marangoni Effect Reverses Coffee-Ring Depositions," *The Journal of Physical Chemistry B*, vol. 110, no. 14, pp. 7090-7094, 2006/04/01 2006.
- [197] H. Hu and R. G. Larson, "Analysis of the effects of Marangoni stresses on the microflow in an evaporating sessile droplet," *Langmuir*, vol. 21, no. 9, pp. 3972-3980, Apr 2005.
- [198] A.-L. Ljung and T. S. Lundström, "Heat and mass transfer boundary conditions at the surface of a heated sessile droplet," *Heat and Mass Transfer*, vol. 53, no. 12, pp. 3581-3591, 2017/12/01 2017.
- [199] R. Savino and S. Fico, "Transient Marangoni convection in hanging evaporating drops," *Physics of Fluids*, vol. 16, no. 10, pp. 3738-3754, 2004/10/01 2004.
- [200] Y. Y. Yan and Y. Q. Zu, "A lattice Boltzmann method for incompressible two-phase flows on partial wetting surface with large density ratio," *Journal of Computational Physics*, vol. 227, no. 1, pp. 763-775, 2007/11/10/ 2007.
- [201] T. Inamuro, "Lattice Boltzmann methods for viscous fluid flows and for two-phase fluid flows," *Fluid Dynamics Research*, vol. 38, no. 9, pp. 641-659, 2006/09/01/ 2006.
- [202] P. V. Coveney, S. Succi, A. J. Briant, P. Papatzacos, and J. M. Yeomans, "Lattice Boltzmann simulations of contact line motion in a liquid-gas system," *Philosophical Transactions of the Royal Society of London. Series A: Mathematical, Physical and Engineering Sciences*, vol. 360, no. 1792, pp. 485-495, 2002/03/15 2002.
- [203] M. Taghilou and M. H. Rahimian, "Lattice Boltzmann model for thermal behavior of a droplet on the solid surface," *International Journal of Thermal Sciences*, vol. 86, pp. 1-11, 2014.
- [204] Q. Guo and P. Cheng, "Direct numerical simulations of sessile droplet evaporation on a heated horizontal surface surrounded by moist air," *International Journal of Heat and Mass Transfer*, vol. 134, pp. 828-841, 2019.
- [205] S. Sohrabi and Y. Liu, "Modeling thermal inkjet and cell printing process using modified pseudopotential and thermal lattice Boltzmann methods," *Phys Rev E*, vol. 97, no. 3-1, p. 033105, Mar 2018.
- [206] Y. Takata, S. Hidaka, A. Yamashita, and H. Yamamoto, "Evaporation of water drop on a plasma-irradiated hydrophilic surface," *International Journal of Heat and Fluid Flow*, vol. 25, no. 2, pp. 320-328, 2004/04/01/ 2004.
- [207] X. Zhang, S. Tan, N. Zhao, X. Guo, X. Zhang, Y. Zhang, and J. Xu, "Evaporation of Sessile Water Droplets on Superhydrophobic Natural Lotus and Biomimetic Polymer Surfaces," *ChemPhysChem*, vol. 7, no. 10, pp. 2067-2070, 2006.
- [208] G. McHale, S. Aqil, N. J. Shirtcliffe, M. I. Newton, and H. Y. Erbil, "Analysis of Droplet Evaporation on a Superhydrophobic Surface," *Langmuir*, vol. 21, no. 24, pp. 11053-11060, 2005/11/01 2005.
- [209] H. Gelderblom, Á. G. Marín, H. Nair, A. van Houselt, L. Lefferts, J. H. Snoeijer, and D. Lohse, "How water droplets evaporate on a superhydrophobic substrate," *Physical Review E*, vol. 83, no. 2, p. 026306, 02/17/ 2011.
- [210] B. Sobac and D. Brutin, "Triple-Line Behavior and Wettability Controlled by Nanocoated Substrates: Influence on Sessile Drop Evaporation," *Langmuir*, vol. 27, no. 24, pp. 14999-15007, 2011/12/20 2011.

- [211] M. J. Gibbons, P. Di Marco, and A. J. Robinson, "Local heat transfer to an evaporating superhydrophobic droplet," *International Journal of Heat and Mass Transfer*, vol. 121, pp. 641-652, 2018/06/01/ 2018.
- [212] S. Dash and S. V. Garimella, "Droplet Evaporation Dynamics on a Superhydrophobic Surface with Negligible Hysteresis," *Langmuir*, vol. 29, no. 34, pp. 10785-10795, 2013/08/27 2013.
- [213] S. Rattle, O. Hofmann, C. P. Price, L. J. Kricka, and D. Wild, "Lab-on-a-Chip, Micro- and Nanoscale Immunoassay Systems, and Microarrays," (in eng), *The Immunoassay Handbook*, pp. 175-202, 2013.
- [214] Y. Cheng, F. Wang, J. Xu, D. Liu, and Y. Sui, "Numerical investigation of droplet spreading and heat transfer on hot substrates," *International Journal of Heat and Mass Transfer*, vol. 121, pp. 402-411, 2018/06/01/ 2018.
- [215] S. Lin, B. Zhao, S. Zou, J. Guo, Z. Wei, and L. Chen, "Impact of viscous droplets on different wettable surfaces: Impact phenomena, the maximum spreading factor, spreading time and post-impact oscillation," *Journal of Colloid and Interface Science*, vol. 516, pp. 86-97, 2018/04/15/ 2018.
- [216] L. Liu, Y. Zhang, G. Cai, and P. A. Tsai, "High-speed dynamics and temperature variation during drop impact on a heated surface," *International Journal of Heat and Mass Transfer*, vol. 189, p. 122710, 2022/06/15/ 2022.
- [217] J. Wu, J. J. Huang, and W. W. Yan, "Lattice Boltzmann investigation of droplets impact behaviors onto a solid substrate," *Colloids and Surfaces A: Physicochemical and Engineering Aspects*, vol. 484, pp. 318-328, 2015/11/05/ 2015.
- [218] J. Philippi, P.-Y. Lagrée, and A. Antkowiak, "Drop impact on a solid surface: short-time self-similarity," *Journal of Fluid Mechanics*, vol. 795, pp. 96-135, 2016.
- [219] H. Wang, C. Liu, H. Zhan, and Y. Liu, "Droplet Asymmetric Bouncing on Inclined Superhydrophobic Surfaces," *ACS Omega*, vol. 4, no. 7, pp. 12238-12243, 2019/07/31 2019.
- [220] S. LeClear, J. LeClear, Abhijeet, K.-C. Park, and W. Choi, "Drop impact on inclined superhydrophobic surfaces," *Journal of Colloid and Interface Science*, vol. 461, pp. 114-121, 2016/01/01/ 2016.
- [221] M. Arogeti, E. Sher, and T. Bar-Kohany, "Drop impact on small targets with different target-to-drop diameters ratio," *Chemical Engineering Science*, vol. 193, pp. 89-101, 2019/01/16/ 2019.
- [222] S. Ding, Z. Hu, L. Dai, X. Zhang, and X. Wu, "Droplet impact dynamics on single-pillar superhydrophobic surfaces," *Physics of Fluids*, vol. 33, no. 10, p. 102108, 2021/10/01 2021.
- [223] Y. Zhu, H.-R. Liu, K. Mu, P. Gao, H. Ding, and X.-Y. Lu, "Dynamics of drop impact onto a solid sphere: spreading and retraction," *Journal of Fluid Mechanics*, vol. 824, p. R3, 2017, Art no. R3.
- [224] X. Liu, J. Min, and X. Zhang, "Dynamic behavior and maximum spreading of droplets impacting concave spheres," *Physics of Fluids*, vol. 32, no. 9, p. 092109, 2020/09/01 2020.
- [225] X. Liu, Y. Zhao, S. Chen, S. Shen, and X. Zhao, "Numerical research on the dynamic characteristics of a droplet impacting a hydrophobic tube," *Physics of Fluids*, vol. 29, no. 6, p. 062105, 2017/06/01 2017.
- [226] W. Zhao, Y. Zhang, W. Shang, Z. Wang, B. Xu, and S. Jiang, "Simulation of droplet impacting a square solid obstacle in microchannel with different wettability by using high density ratio pseudopotential multiple-relaxation-time (MRT) lattice Boltzmann method (LBM)," *Canadian Journal of Physics*, vol. 97, no. 1, pp. 93-113, 2019.
- [227] Y. Q. Zu and Y. Y. Yan, "Lattice Boltzmann method for modelling droplets on chemically heterogeneous and microstructured surfaces with large liquid-gas density ratio," *IMA Journal of Applied Mathematics*, vol. 76, no. 5, pp. 743-760, 2011.
- [228] Y. Q. Zu, Y. Y. Yan, J. Q. Li, and Z. W. Han, "Wetting Behaviours of a Single Droplet on Biomimetic Micro Structured Surfaces," *Journal of Bionic Engineering*, vol. 7, no. 2, pp. 191-198, 2010/06/01/ 2010.

- [229] Y. Shen, S. Liu, C. Zhu, J. Tao, Z. Chen, H. Tao, L. Pan, G. Wang, and T. Wang, "Bouncing dynamics of impact droplets on the convex superhydrophobic surfaces," *Applied Physics Letters*, vol. 110, no. 22, p. 221601, 2017/05/29 2017.
- [230] Y. Liu, L. Moevius, X. Xu, T. Qian, J. M. Yeomans, and Z. Wang, "Pancake bouncing on superhydrophobic surfaces," *Nature Physics*, vol. 10, no. 7, pp. 515-519, 2014/07/01 2014.
- [231] J. Luo, F. Chu, Z. Ni, J. Zhang, and D. Wen, "Dynamics of droplet impacting on a cone," *Physics of Fluids*, vol. 33, no. 11, p. 112116, 2021/11/01 2021.
- [232] K. Sun, M. Jia, and T. Wang, "Numerical investigation of head-on droplet collision with lattice Boltzmann method," *International Journal of Heat and Mass Transfer*, vol. 58, no. 1, pp. 260-275, 2013/03/01/ 2013.
- [233] L. Chen, Q. Kang, Y. Mu, Y.-L. He, and W.-Q. Tao, "A critical review of the pseudopotential multiphase lattice Boltzmann model: Methods and applications," *International Journal of Heat and Mass Transfer*, vol. 76, pp. 210-236, 2014/09/01/ 2014.
- [234] J. M. Gac and L. Gradoń, "Lattice-Boltzmann modeling of collisions between droplets and particles," *Colloids and Surfaces A: Physicochemical and Engineering Aspects*, vol. 441, pp. 831-836, 2014/01/20/ 2014.
- [235] S. Shen, F. Bi, and Y. Guo, "Simulation of droplets impact on curved surfaces with lattice Boltzmann method," *International Journal of Heat and Mass Transfer*, vol. 55, no. 23, pp. 6938-6943, 2012/11/01/ 2012.
- [236] A. Merdasi, S. Ebrahimi, A. Moosavi, M. B. Shafii, and F. Kowsary, "Simulation of a falling droplet in a vertical channel with rectangular obstacles," *European Journal of Mechanics - B/Fluids*, vol. 68, pp. 108-117, 2018/03/01/ 2018.
- [237] M. Bakhshan, M. Wörner, and A. Dadvand, "Simulation of droplet impingement on a rigid square obstacle in a microchannel using multiphase lattice Boltzmann method," *Computational Particle Mechanics*, vol. 8, no. 4, pp. 973-991, 2021/07/01 2021.
- [238] Q. Zou and X. He, "On pressure and velocity flow boundary conditions and bounceback for the lattice Boltzmann BGK model," *Phys. Fluids*, vol. 9, no. 6, 1997.
- [239] C. K. Law, "Recent advances in droplet vaporization and combustion," *Progress in Energy and Combustion Science*, vol. 8, no. 3, pp. 171-201, 1982/01/01/ 1982.
- [240] A. R. Rahmati and A. Zarareh, "Application of a modified pseudopotential lattice Boltzmann model for simulation of splashing phenomenon," *European Journal of Mechanics - B/Fluids*, vol. 70, pp. 19-35, 2018/07/01/ 2018.
- [241] R. Ma, X. Zhou, B. Dong, W. Li, and J. Gong, "Simulation of impacting process of a saturated droplet upon inclined surfaces by lattice Boltzmann method," *International Journal of Heat and Fluid Flow*, vol. 71, pp. 1-12, 2018/06/01/ 2018.
- [242] E. Silk, J. Kim, and K. Kiger, "Investigation of Enhanced Surface Spray Cooling," *American Society of Mechanical Engineers, Heat Transfer Division, (Publication) HTD*, vol. 375, 02/01 2004.
- [243] M. S. Sehmbe, M. R. Pais, and L. C. Chow, "Effect of surface material properties and surface characteristics in evaporative spray cooling," *Journal of Thermophysics and Heat Transfer*, vol. 6, no. 3, pp. 505-512, 1992/07/01 1992.
- [244] B. L. Scheller and D. W. Bousfield, "Newtonian drop impact with a solid surface," *AIChE Journal*, vol. 41, no. 6, pp. 1357-1367, 1995.
- [245] C. Clanet, C. BÉGuin, D. Richard, and D. QuÉRÉ, "Maximal deformation of an impacting drop," *Journal of Fluid Mechanics*, vol. 517, pp. 199-208, 2004.
- [246] M. Pasandideh-Fard, Y. M. Qiao, S. Chandra, and J. Mostaghimi, "Capillary effects during droplet impact on a solid surface," *Physics of Fluids*, vol. 8, no. 3, pp. 650-659, 1996.
- [247] C. Ukiwe and D. Y. Kwok, "On the Maximum Spreading Diameter of Impacting Droplets on Well-Prepared Solid Surfaces," *Langmuir*, vol. 21, no. 2, pp. 666-673, 2005/01/01 2005.
- [248] J. Eggers, M. A. Fontelos, C. Josserand, and S. Zaleski, "Drop dynamics after impact on a solid wall: Theory and simulations," *Physics of Fluids*, vol. 22, no. 6, p. 062101, 2010.

- [249] L. Xu, W. W. Zhang, and S. R. Nagel, "Drop splashing on a dry smooth surface," (in eng), *Phys Rev Lett*, vol. 94, no. 18, p. 184505, May 13 2005.
- [250] A. L. N. Moreira, A. S. Moita, and M. R. Panão, "Advances and challenges in explaining fuel spray impingement: How much of single droplet impact research is useful?," *Progress in Energy and Combustion Science*, vol. 36, no. 5, pp. 554-580, 2010/10/01/ 2010.
- [251] J. Palacios, J. Hernández, P. Gómez, C. Zanzi, and J. López, "Experimental study of splashing patterns and the splashing/deposition threshold in drop impacts onto dry smooth solid surfaces," *Experimental Thermal and Fluid Science*, vol. 44, pp. 571-582, 2013/01/01/ 2013.
- [252] I. V. Roisman, R. Rioboo, and C. Tropea, "Normal impact of a liquid drop on a dry surface: model for spreading and receding," *Proceedings of the Royal Society of London. Series A: Mathematical, Physical and Engineering Sciences*, vol. 458, no. 2022, pp. 1411-1430, 2002/06/08 2002.
- [253] A. L. Yarin, "DROP IMPACT DYNAMICS: Splashing, Spreading, Receding, Bouncing...," *Annual Review of Fluid Mechanics*, vol. 38, no. 1, pp. 159-192, 2006.
- [254] Y. Yonemoto, M. Yamashita, K. Tashiro, and T. Kunugi, "Estimating the number of fingers and size of ejected droplets in droplet impingement processes on solid substrates," *Colloid and Interface Science Communications*, vol. 50, p. 100651, 2022/09/01/ 2022.

Appendix: C++ code

The provided code illustrates the case of a sessile droplet placed on a heat plate. The code is based on the multi-component multiphase pseudopotential Lattice Boltzmann model. For particular studies in this thesis, the code is developed by modifying the code below.

```
#include <iostream>
#include <direct.h>
#include <windows.h>
#include <stdio.h>
#include <string>
#include <stdlib.h>
#include <math.h>
#include <cmath>
#include <limits>
#include <stdexcept>
#include <typeinfo>
#include <vector>
#include <algorithm>

using namespace std;

#define R0 40.0
#define X0 99
#define Y0 1

#define LX 200
#define LY 201
#define LXY (LX * LY)
#define Q 9

#define a (2.0 / 49)
#define b (2.0 / 21)
#define R 1.0
#define ome 0.344

#define Tc (0.0778 / 0.45724 * a / (b * R))
#define Ts (0.85 * Tc)
#define dT 0.10 * Tc

#define rho_l 6.6293
#define rho_v 0.3413
#define rho_a ((rho_l + rho_v) / 2)
#define rho_gi 0.00171
#define rho_go 0.00171
#define rho_wall 0.0
#define width 5

#define cvl 3.23
#define cvv 2.27
#define cvg 1.0
#define lambda_l 0.96
#define lambda_v 0.066
#define cpl 4.0
#define cpv 0.75
#define cpg 0.75

#define nu_l (0.5 / 3)
#define nu_v (0.5 / 3)
#define nu_g (0.5 / 3)
#define alpha_l (0.5 / 3)
```

```

#define alpha_v (0.5 / 3)
#define alpha_g (0.5 / 3)

#define cc 1.0
#define c_squ (cc * cc / 3.0)

#define G00 -1.0
#define G11 0.0
#define G01 0.25
#define GW0 0.0
#define GW1 0.0
#define GR 1e-5

#define beta0 1.16
#define beta1 1.0
#define karmap 0.9

#define fluid 0
#define solid 1

#define PI 3.1415926

#define ERR 1.0e-9
#define IT 1000000

double w[Q] = {4.0 / 9, 1.0 / 9, 1.0 / 9, 1.0 / 9, 1.0 / 9, 1.0 / 36, 1.0 / 36, 1.0 / 36,
1.0 / 36};
double e[Q][2] = {{0, 0}, {1, 0}, {0, 1}, {-1, 0}, {0, -1}, {1, 1}, {-1, 1}, {-1, -1}, {1,
-1}};

double
    flag[LX][LY],
    s[LX][LY], fluid_node[LX][LY], tau[2][LX][LY], tau_T[2][LX][LY],
    ff[2][LX][LY][Q], fe[2][LX][LY][Q], gf[2][LX][LY][Q], ge[2][LX][LY][Q],
    rho[2][LX][LY], rho_mean, nu[2][LX][LY], alpha[2][LX][LY],
    phi[LX][LY], pressure[LX][LY], p[2][LX][LY], ptotal[LX][LY], psx[2][LX][LY],
psi[2][LX][LY],
    u[2][LX][LY][2], ureal[2][LX][LY][2], utot[LX][LY][2], ab_u[LX][LY],
    Ttot[LX][LY], T[2][LX][LY], lambda[2][LX][LY], cv[2][LX][LY], cp[2][LX][LY],
sita[2][LX][LY], Tb,
    F[2][LX][LY][2], Fw[2][LX][LY][2], Fm[2][LX][LY][2], Fb[2][LX][LY][2], gravity;

double feq(int k, double rho, double u[2]);
double feq_g(int k, double T, double u[2]);
void ini_geo(void);
void initial(void);
void collision(void);
void stream(void);
void boundary(void);
void macrop(void);
void forces(void);
void evolve(void);
void contact_angle(int T, double err, int N);
double err(double p[LX][LY]);
void write(int W);

double feq(int k, double rho, double u[2])
{
    double eu, uv, feq;
    eu = e[k][0] * u[0] + e[k][1] * u[1];
    uv = u[0] * u[0] + u[1] * u[1];
    feq = w[k] * rho * (1.0 + 3.0 * eu + 4.5 * eu * eu - 1.5 * uv);
    return feq;
}
double feq_g(int k, double T, double u[2])
{

```

```

double eu, uv, feq_g;
eu = e[k][0] * u[0] + e[k][1] * u[1];
uv = u[0] * u[0] + u[1] * u[1];
feq_g = w[k] * T * (1.0 + 3.0 * eu + 4.5 * eu * eu - 1.5 * uv);
return feq_g;
}

void ini_geo()
{
    int i, j;
    for (j = 0; j < LY; j++)
        for (i = 0; i < LX; i++)
        {
            if (j == 0)
            {
                flag[i][j] = solid;
                s[i][j] = 1.0;
            }
            else
            {
                flag[i][j] = fluid;
                s[i][j] = 0.0;
            }
        }
}

void initial()
{
    int i, j, k, v;
    double rho_sum = 0.0, flow_field = 0.0;

    for (j = 0; j < LY; j++)
    {
        for (i = 0; i < LX; i++)
        {
            if (flag[i][j] == fluid)
            {
                T[0][i][j] = T[1][i][j] = Ttot[i][j] = Ts;

                rho[0][i][j] = (rho_v + rho_l) / 2.0 + (rho_v - rho_l) * tanh(2.0 *
(sqrt(pow((i - X0), 2) + pow((j - Y0), 2)) - R0) / width) / 2.0;
                rho[1][i][j] = (rho_go + rho_gi) / 2.0 + (rho_go - rho_gi) * tanh(2 *
(sqrt(pow((i - X0), 2) + pow((j - Y0), 2)) - R0) / width) / 2.0;
            }
            else
            {
                T[0][i][j] = T[1][i][j] = Ttot[i][j] = Ts;

                rho[0][i][j] = rho_wall;
                rho[1][i][j] = rho_wall;
            }

            for (v = 0; v < 2; v++)
            {
                u[v][i][j][0] = u[v][i][j][1] = 0.0;
                F[v][i][j][0] = F[v][i][j][1] = 0.0;
                ureal[v][i][j][0] = ureal[v][i][j][1] = 0.0;
            }

            utot[i][j][0] = utot[i][j][1] = 0.0;

            if (flag[i][j] == fluid)
            {
                cv[0][i][j] = (cvl * (rho[0][i][j] - rho_v) + cvv * (rho_l - rho[0][i][j]))
/ (rho_l - rho_v);

```

```

        lambda[0][i][j] = (lambda_l * (rho[0][i][j] - rho_v) + lambda_v * (rho_l -
rho[0][i][j])) / (rho_l - rho_v);
        nu[0][i][j] = (nu_l * (rho[0][i][j] - rho_v) + nu_v * (rho_l -
rho[0][i][j])) / (rho_l - rho_v);
        alpha[0][i][j] = (alpha_l * (rho[0][i][j] - rho_v) + alpha_v * (rho_l -
rho[0][i][j])) / (rho_l - rho_v);

        cv[1][i][j] = cvg;
        lambda[1][i][j] = 0.028 * rho[1][i][j];
        nu[1][i][j] = nu_g;
        alpha[1][i][j] = alpha_g;

        for (v = 0; v < 2; v++)
        {
            tau[v][i][j] = 3.0 * nu[v][i][j] + 0.5;
            tau_T[v][i][j] = 3 * alpha[v][i][j] + 0.5;
        }

        phi[i][j] = pow((1.0 + (0.37464 + 1.54226 * ome - 0.26992 * ome * ome) * (1
- sqrt(Ttot[i][j] / Tc))), 2.0);
        p[0][i][j] = karmap * (rho[0][i][j] * R * Ttot[i][j]) / (1 - b *
rho[0][i][j]) - a * phi[i][j] * (rho[0][i][j] * rho[0][i][j]) / (1 + 2 * b * rho[0][i][j] -
(b * b) * (rho[0][i][j] * rho[0][i][j]));
        p[1][i][j] = rho[1][i][j] * R * Ttot[i][j];
        ptotal[i][j] = p[0][i][j] + p[1][i][j];
        pressure[i][j] = ptotal[i][j];

        for (v = 0; v < 2; v++)
        {
            for (k = 0; k < Q; ++k)
            {
                fe[v][i][j][k] = feq(k, rho[v][i][j], u[v][i][j]);
                ff[v][i][j][k] = fe[v][i][j][k];

                ge[v][i][j][k] = feq_g(k, Ttot[i][j], utot[i][j]);
                gf[v][i][j][k] = ge[v][i][j][k];
            }
        }
    }
else
{
    for (k = 0; k < Q; ++k)
    {
        for (v = 0; v < 2; v++)
        {
            fe[v][i][j][k] = 0.0;
            ff[v][i][j][k] = 0.0;

            ge[v][i][j][k] = 0.0;
            gf[v][i][j][k] = 0.0;
        }
    }
}
}
}

void stream()
{
    int v, i, j, k, id, jd;
    for (j = 0; j < LY; j++)
        for (i = 0; i < LX; i++)
        {
            if (flag[i][j] == fluid)
            {
                for (k = 0; k < Q; k++)

```

```

        {
            id = i - int(e[k][0]);
            jd = j - int(e[k][1]);
            if (id > LX - 1)
                id = 0;
            if (id < 0)
                id = LX - 1;

            for (v = 0; v < 2; v++)
            {
                ff[v][i][j][k] = fe[v][id][jd][k];
                gf[v][i][j][k] = ge[v][id][jd][k];
            }
        }
    }
}

void boundary()
{
    int v, i, k;
    for (i = 0; i < LX; i++)
    {
        for (v = 0; v < 2; v++)
        {
            ff[v][i][1][2] = ff[v][i][1][4];
            ff[v][i][1][5] = ff[v][i][1][7] + (ff[v][i][1][3] - ff[v][i][1][1]) / 2 -
(F[v][i][1][0] + F[v][i][1][1]) / 4.0;
            ff[v][i][1][6] = ff[v][i][1][8] + (ff[v][i][1][1] - ff[v][i][1][3]) / 2 +
(F[v][i][1][0] - F[v][i][1][1]) / 4.0;

            u[v][i][LY - 1][0] = u[v][i][LY - 2][0];
            u[v][i][LY - 1][1] = u[v][i][LY - 2][1];
            ureal[v][i][LY - 1][0] = ureal[v][i][LY - 2][0];
            ureal[v][i][LY - 1][1] = ureal[v][i][LY - 2][1];

            T[v][i][LY - 1] = T[v][i][LY - 2];
            T[v][i][1] = Tb;
        }

        utot[i][LY - 1][0] = utot[i][LY - 2][0];
        utot[i][LY - 1][1] = utot[i][LY - 2][1];
        Ttot[i][LY - 1] = Ttot[i][LY - 2];
        Ttot[i][1] = Tb;

        for (v = 0; v < 2; v++)
        {
            for (k = 0; k < Q; k++)
            {
                ff[v][i][LY - 1][k] = feq(k, rho[v][i][LY - 1], u[v][i][LY - 1]) + (1 - 1 /
tau[v][i][LY - 1]) * (ff[v][i][LY - 2][k] - feq(k, rho[v][i][LY - 2], u[v][i][LY - 2]));

                gf[v][i][LY - 1][k] = feq_g(k, Ttot[i][LY - 1], utot[i][LY - 1]) + (1 - 1 /
tau_T[v][i][LY - 2]) * (gf[v][i][LY - 2][k] - feq_g(k, Ttot[i][LY - 2], utot[i][LY - 2]));
                gf[v][i][1][k] = feq_g(k, Ttot[i][1], utot[i][1]) + (1 - 1 /
tau_T[v][i][1]) * (gf[v][i][2][k] - feq_g(k, Ttot[i][2], utot[i][2]));
            }
        }
    }
}

void macrop()
{
    int v, i, j, k, il, ir;

    for (j = 0; j < LY; j++)

```

```

for (i = 0; i < LX; i++)
{
    if (flag[i][j] == fluid)
    {
        for (v = 0; v < 2; v++)
        {
            rho[v][i][j] = 0.0;
            T[v][i][j] = 0.0;

            for (k = 0; k < Q; k++)
            {
                rho[v][i][j] += ff[v][i][j][k];
                T[v][i][j] += gf[v][i][j][k];
            }
        }

        cv[0][i][j] = (cvl * (rho[0][i][j] - rho_v) + cvv * (rho_l - rho[0][i][j]))
/ (rho_l - rho_v);
        lambda[0][i][j] = (lambda_l * (rho[0][i][j] - rho_v) + lambda_v * (rho_l -
rho[0][i][j])) / (rho_l - rho_v);
        nu[0][i][j] = (nu_l * (rho[0][i][j] - rho_v) + nu_v * (rho_l -
rho[0][i][j])) / (rho_l - rho_v);
        alpha[0][i][j] = (alpha_l * (rho[0][i][j] - rho_v) + alpha_v * (rho_l -
rho[0][i][j])) / (rho_l - rho_v);

        cv[1][i][j] = cvg;
        lambda[1][i][j] = 0.028 * rho[1][i][j];
        nu[1][i][j] = nu_g;
        alpha[1][i][j] = alpha_g;

        for (v = 0; v < 2; v++)
        {
            tau[v][i][j] = 3.0 * nu[v][i][j] + 0.5;
            tau_T[v][i][j] = 3.0 * alpha[v][i][j] + 0.5;
        }

        Ttot[i][j] = (rho[0][i][j] * cv[0][i][j] * T[0][i][j] + rho[1][i][j] *
cv[1][i][j] * T[1][i][j]) / (rho[0][i][j] * cv[0][i][j] + rho[1][i][j] * cv[1][i][j]);
    }
}

for (i = 0; i < LX; i++)
{
    for (v = 0; v < 2; v++)
    {
        T[v][i][0] = T[v][i][1] = Tb;
        T[v][i][LY - 1] = T[v][i][LY - 2] = Ts;
    }

    Ttot[i][0] = Ttot[i][1] = Tb;
    Ttot[i][LY - 1] = Ttot[i][LY - 2] = Ts;
}

for (i = 0; i < LX; i++)
{
    il = i - 1;
    ir = i + 1;
    if (ir > LX - 1)
        ir = 0;
    if (il < 0)
        il = LX - 1;

    for (j = 0; j < LY; j++)
    {
        if (flag[i][j] == fluid)
        {

```

```

        for (v = 0; v < 2; v++)
        {
            sita[v][i][j] = T[v][i][j] * (1 - R / (cv[v][i][j] * (1 - b *
rho[v][i][j]))) * (ureal[v][ir][j][0] - ureal[v][il][j][0] + ureal[v][i][j + 1][1] -
ureal[v][i][j - 1][1]) / 2.0;
            //+(T[v][ir][j] - T[v][i][j]) * (lambda[v][ir][j] * (1 / (rho[v][i][j]
* cv[v][i][j]) - 1 / (rho[v][ir][j] * cp[v][ir][j]))) + lambda[v][i][j] * (1 / (rho[v][i][j]
* cv[v][i][j]) - 1 / (rho[v][i][j] * cp[v][i][j])))) / 2.0 + (T[v][il][j] - T[v][i][j]) *
(lambda[v][il][j] * (1 / (rho[v][i][j] * cv[v][i][j]) - 1 / (rho[v][il][j] * cp[v][il][j]))
+ lambda[v][i][j] * (1 / (rho[v][i][j] * cv[v][i][j]) - 1 / (rho[v][i][j] * cp[v][i][j]))))
/ 2.0 + (T[v][i][j + 1] - T[v][i][j]) * (lambda[v][i][j + 1] * (1 / (rho[v][i][j] *
cv[v][i][j]) - 1 / (rho[v][i][j + 1] * cp[v][i][j + 1])) + lambda[v][i][j] * (1 /
(rho[v][i][j] * cv[v][i][j]) - 1 / (rho[v][i][j] * cp[v][i][j])))) / 2.0 + (T[v][i][j - 1] -
T[v][i][j]) * (lambda[v][i][j - 1] * (1 / (rho[v][i][j] * cv[v][i][j]) - 1 / (rho[v][i][j -
1] * cp[v][i][j - 1])) + lambda[v][i][j] * (1 / (rho[v][i][j] * cv[v][i][j]) - 1 /
(rho[v][i][j] * cp[v][i][j])))) / 2.0;
        }
    }
}

for (j = 0; j < LY; j++)
    for (i = 0; i < LX; i++)
    {
        if (flag[i][j] == fluid)
        {
            phi[i][j] = pow((1.0 + (0.37464 + 1.54226 * ome - 0.26992 * ome * ome) * (1
- sqrt(Ttot[i][j] / Tc))), 2.0);
            p[0][i][j] = karmap * (rho[0][i][j] * R * Ttot[i][j] / (1 - b *
rho[0][i][j]) - a * phi[i][j] * (rho[0][i][j] * rho[0][i][j]) / (1 + 2 * b * rho[0][i][j] -
(b * b) * (rho[0][i][j] * rho[0][i][j])));
            p[1][i][j] = rho[1][i][j] * R * Ttot[i][j];
            pressure[i][j] = ptotal[i][j];
            ptotal[i][j] = p[0][i][j] + p[1][i][j];
        }
    }
}

void forces()
{
    int v, i, j, k;
    for (j = 0; j < LY; j++)
        for (i = 0; i < LX; i++)
        {
            if (flag[i][j] == fluid)
            {
                psx[0][i][j] = sqrt(2.0 * (p[0][i][j] - rho[0][i][j] * c_squ) / G00 /
c_squ);
                psx[1][i][j] = sqrt(2.0 * (p[1][i][j] - rho[1][i][j] * c_squ) / (-1.0) /
c_squ);

                psi[0][i][j] = rho[0][i][j];
                psi[1][i][j] = rho[1][i][j];
            }
            else if (j == 0)
            {
                psx[0][i][j] = psx[0][i][1];
                psx[1][i][j] = psx[1][i][1];

                psi[0][i][j] = psi[0][i][1];
                psi[1][i][j] = psi[1][i][1];
            }
            else if (j == LY - 1)
            {
                psx[0][i][j] = psx[0][i][LY - 2];
                psx[1][i][j] = psx[1][i][LY - 2];
            }
        }
}

```

```

        psi[0][i][j] = psi[0][i][LY - 2];
        psi[1][i][j] = psi[1][i][LY - 2];
    }
}

int id, jd;
double fx0, fy0, fx1, fy1;
for (j = 0; j < LY - 1; j++)
    for (i = 0; i < LX; i++)
    {
        if (flag[i][j] == fluid)
        {
            fx0 = 0.0;
            fy0 = 0.0;
            fx1 = 0.0;
            fy1 = 0.0;

            for (k = 1; k < Q; k++)
            {
                id = i + int(e[k][0]);
                jd = j + int(e[k][1]);
                if (id > LX - 1)
                    id = 0;
                if (id < 0)
                    id = LX - 1;

                fx0 += (-beta0) * psx[0][i][j] * psx[0][id][jd] * w[k] * G00 * e[k][0]
- ((1 - beta0) / 2.0) * psx[0][id][jd] * psx[0][id][jd] * w[k] * G00 * e[k][0] -
psi[0][i][j] * psi[1][id][jd] * w[k] * G01 * e[k][0];
                fy0 += (-beta0) * psx[0][i][j] * psx[0][id][jd] * w[k] * G00 * e[k][1]
- ((1 - beta0) / 2.0) * psx[0][id][jd] * psx[0][id][jd] * w[k] * G00 * e[k][1] -
psi[0][i][j] * psi[1][id][jd] * w[k] * G01 * e[k][1];
                fx1 += (-beta1) * psx[1][i][j] * psx[1][id][jd] * w[k] * G11 * e[k][0]
- ((1 - beta1) / 2.0) * psx[1][id][jd] * psx[1][id][jd] * w[k] * G11 * e[k][0] -
psi[1][i][j] * psi[0][id][jd] * w[k] * G01 * e[k][0];
                fy1 += (-beta1) * psx[1][i][j] * psx[1][id][jd] * w[k] * G11 * e[k][1]
- ((1 - beta1) / 2.0) * psx[1][id][jd] * psx[1][id][jd] * w[k] * G11 * e[k][1] -
psi[1][i][j] * psi[0][id][jd] * w[k] * G01 * e[k][1];
            }

            Fm[0][i][j][0] = fx0;
            Fm[0][i][j][1] = fy0;
            Fm[1][i][j][0] = fx1;
            Fm[1][i][j][1] = fy1;
        }
        else
        {
            Fm[0][i][j][0] = 0.0;
            Fm[0][i][j][1] = 0.0;
            Fm[1][i][j][0] = 0.0;
            Fm[1][i][j][1] = 0.0;
        }
    }

for (j = 0; j < LY; j++)
    for (i = 0; i < LX; i++)
    {
        if (flag[i][j] == fluid)
        {
            fx0 = 0.0;
            fy0 = 0.0;
            fx1 = 0.0;
            fy1 = 0.0;

            for (k = 1; k < Q; k++)

```

```

    {
        id = i + int(e[k][0]);
        jd = j + int(e[k][1]);
        if (id > LX - 1)
            id = 0;
        if (id < 0)
            id = LX - 1;

        fx0 += (-psx[0][i][j]) * psx[0][i][j] * s[id][jd] * w[k] * GW0 *
e[k][0];
        fy0 += (-psx[0][i][j]) * psx[0][i][j] * s[id][jd] * w[k] * GW0 *
e[k][1];
        fx1 += (-psx[1][i][j]) * psx[1][i][j] * s[id][jd] * w[k] * GW1 *
e[k][0];
        fy1 += (-psx[1][i][j]) * psx[1][i][j] * s[id][jd] * w[k] * GW1 *
e[k][1];
    }

    Fw[0][i][j][0] = fx0;
    Fw[0][i][j][1] = fy0;
    Fw[1][i][j][0] = fx1;
    Fw[1][i][j][1] = fy1;
}
else
{
    Fw[0][i][j][0] = 0.0;
    Fw[0][i][j][1] = 0.0;
    Fw[1][i][j][0] = 0.0;
    Fw[1][i][j][1] = 0.0;
}
}

double rho_sum0 = 0.0, rho_sum1 = 0.0, flow_field = 0.0, rho_mean0 = 0.0, rho_mean1 =
0.0;
for (j = 0; j < LY; j++)
    for (i = 0; i < LX; i++)
    {
        if (flag[i][j] == fluid)
        {
            rho_sum0 += rho[0][i][j];
            rho_sum1 += rho[1][i][j];

            flow_field += 1;
        }
    }
rho_mean0 = rho_sum0 / flow_field;
rho_mean1 = rho_sum1 / flow_field;

for (j = 0; j < LY; j++)
    for (i = 0; i < LX; i++)
    {
        if (flag[i][j] == fluid)
        {
            Fb[0][i][j][0] = 0.0;
            Fb[0][i][j][1] = (rho[0][i][j] - rho_mean0) * (-gravity);
            Fb[1][i][j][0] = 0.0;
            Fb[1][i][j][1] = (rho[1][i][j] - rho_mean1) * (-gravity);
        }
        else
        {
            Fb[0][i][j][0] = 0.0;
            Fb[0][i][j][1] = 0.0;
            Fb[1][i][j][0] = 0.0;
            Fb[1][i][j][1] = 0.0;
        }
    }
}

```

```

for (j = 0; j < LY; j++)
  for (i = 0; i < LX; i++)
  {
    if (flag[i][j] == fluid)
    {
      F[0][i][j][0] = Fm[0][i][j][0] + Fw[0][i][j][0] + Fb[0][i][j][0];
      F[0][i][j][1] = Fm[0][i][j][1] + Fw[0][i][j][1] + Fb[0][i][j][1];
      F[1][i][j][0] = Fm[1][i][j][0] + Fw[1][i][j][0] + Fb[1][i][j][0];
      F[1][i][j][1] = Fm[1][i][j][1] + Fw[1][i][j][1] + Fb[1][i][j][1];
    }
  }

double momex[2], momey[2];
for (j = 0; j < LY; j++)
  for (i = 0; i < LX; i++)
  {
    if (flag[i][j] == fluid)
    {
      for (v = 0; v < 2; v++)
      {
        momex[v] = 0.0;
        momey[v] = 0.0;

        for (k = 0; k < Q; k++)
        {
          momex[v] += (ff[v][i][j][k] * e[k][0]);
          momey[v] += (ff[v][i][j][k] * e[k][1]);
        }

        ureal[v][i][j][0] = (momex[v] + 0.5 * F[v][i][j][0]) / rho[v][i][j];
        ureal[v][i][j][1] = (momey[v] + 0.5 * F[v][i][j][1]) / rho[v][i][j];
      }
      u[0][i][j][0] = (momex[0] / tau[0][i][j] + momex[1] / tau[1][i][j] +
F[0][i][j][0]) / (rho[0][i][j] / tau[0][i][j] + rho[1][i][j] / tau[1][i][j]);
      u[0][i][j][1] = (momey[0] / tau[0][i][j] + momey[1] / tau[1][i][j] +
F[0][i][j][1]) / (rho[0][i][j] / tau[0][i][j] + rho[1][i][j] / tau[1][i][j]);

      u[1][i][j][0] = (momex[0] / tau[0][i][j] + momex[1] / tau[1][i][j] +
F[1][i][j][0]) / (rho[0][i][j] / tau[0][i][j] + rho[1][i][j] / tau[1][i][j]);
      u[1][i][j][1] = (momey[0] / tau[0][i][j] + momey[1] / tau[1][i][j] +
F[1][i][j][1]) / (rho[0][i][j] / tau[0][i][j] + rho[1][i][j] / tau[1][i][j]);

      utot[i][j][0] = (rho[0][i][j] * ureal[0][i][j][0] + rho[1][i][j] *
ureal[1][i][j][0]) / (rho[0][i][j] + rho[1][i][j]);
      utot[i][j][1] = (rho[0][i][j] * ureal[0][i][j][1] + rho[1][i][j] *
ureal[1][i][j][1]) / (rho[0][i][j] + rho[1][i][j]);

      ab_u[i][j] = sqrt(utot[i][j][0] * utot[i][j][0] + utot[i][j][1] *
utot[i][j][1]);
    }
    else
    {
      for (v = 0; v < 2; v++)
      {
        ureal[v][i][j][0] = ureal[v][i][j][1] = 0.0;
        u[v][i][j][0] = u[v][i][j][1] = 0.0;
      }
      utot[i][j][0] = utot[i][j][1] = 0.0;
      ab_u[i][j] = 0.0;
    }
  }
}

void collision()
{

```

```

int v, i, j, k;
for (j = 0; j < LY; j++)
  for (i = 0; i < LX; i++)
  {
    for (v = 0; v < 2; v++)
    {
      for (k = 0; k < Q; k++)
      {
        fe[v][i][j][k] = ff[v][i][j][k] - (ff[v][i][j][k] - feq(k,
rho[v][i][j], u[v][i][j])) / tau[v][i][j];

        ge[v][i][j][k] = gf[v][i][j][k] - (gf[v][i][j][k] - feq_g(k,
Ttot[i][j], utot[i][j])) / tau_T[v][i][j] + w[k] * sita[v][i][j];
      }
    }
  }
}

void evolve()
{
  stream();
  boundary();
  macrop();
  forces();
  collision();
}

double err(double p[LX][LY])
{
  int i, j;

  double diff;
  diff = 0.0;

  for (i = 0; i < LX; i++)
  {
    for (j = 0; j < LY; j++)
    {
      diff = max(diff, fabs(pressure[i][j] - ptotal[i][j]));
    }
  }
  return (diff);
}

void write(int W)
{
  FILE *fp;
  int i, j;
  char name[50];
  for (i = 0; i < 50; i++)
    name[i] = '\0';
  sprintf(name, "./result/Step%05d%s", W, ".tec");
  if ((fp = fopen(name, "w")) == NULL)
  {
    printf("File open error\n");
    system("pause");
    exit(1);
  }

  fprintf(fp, "VARIABLES = X, Y, Rho0, Rho1, u, v, abu, p0, p1, p, Ttot\n");
  fprintf(fp, "ZONE I=%d", LX);
  fprintf(fp, ", J=%d\n", LY);
  fprintf(fp, "F=POINT\n");
  for (j = 0; j < LY; j++)
    for (i = 0; i < LX; i++)
    {

```

```

        fprintf(fp, "%i\t%i\t%f\t%f\t%f\t%f\t%f\t%f\t%f\t%f\t%f\n", i, j, rho[0][i][j],
rho[1][i][j], utot[i][j][0], utot[i][j][1], ab_u[i][j], p[0][i][j], p[1][i][j],
ptotal[i][j], Ttot[i][j]);
    }

    fclose(fp);
}

void contact_angle(int T, double err, int N)
{
    int i, j;
    double b0, b1, b2, a0, R_fin, angle;

    for (i = 0; i < LX - 1; i++)
    {
        if (rho[0][i][Y0] < rho_a && rho[0][i + 1][Y0] >= rho_a)
            b1 = double(i) + (rho_a - rho[0][i][Y0]) / (rho[0][i + 1][Y0] - rho[0][i][Y0]);

        if (rho[0][i][Y0] > rho_a && rho[0][i + 1][Y0] <= rho_a)
            b2 = double(i) + (rho_a - rho[0][i][Y0]) / (rho[0][i + 1][Y0] - rho[0][i][Y0]);
    }
    b0 = b2 - b1;

    for (j = 1; j < LY - 1; j++)
    {
        if (rho[0][X0][j] > rho_a && rho[0][X0][j + 1] <= rho_a)
            a0 = double(j) + (rho_a - rho[0][X0][j]) / (rho[0][X0][j + 1] - rho[0][X0][j]);
    }
    a0 = a0 - Y0;

    R_fin = a0 / 2.0 + b0 * b0 / (8.0 * a0);

    angle = atan(b0 / (2.0 * R_fin - 2.0 * a0));

    if (angle < 0)
        angle = PI + angle;

    angle = angle / PI * 180;

    printf("R_fin=%f\t\tangle=%f\t\t", R_fin, angle);

    double p_in, p_out, delta_p, st, size;

    int size_liq, size_vg;

    p_in = p_out = 0.0;
    size_liq = size_vg = 0;

    for (j = 1; j < LY; j++)
        for (i = 0; i < LX; i++)
        {
            if (rho[0][i][j] > rho_a)
            {
                size_liq++;
                p_in += pressure[i][j];
            }
            if (rho[0][i][j] <= rho_a)
            {
                size_vg++;
                p_out += pressure[i][j];
            }
        }

    size = double(size_liq);
}

```

```

p_in = p_in / double(size_liq);
p_out = p_out / double(size_vg);

delta_p = p_in - p_out;

st = delta_p * R_fin;

printf("size=%g\tdelta_p=%g\tst=%g\n\n", size, delta_p, st);

FILE *fpresult;
char name[50];
for (i = 0; i < 50; i++)
    name[i] = '\0';

sprintf(name, "./result/contact_angle.txt");
fpresult = fopen(name, "a+");
if (fpresult == NULL)
{
    printf("file contact_angle open error!\n\n");
    system("pause");
    exit(1);
}
fprintf(fpresult, "IT=%d\t error=%e\n\n", T, err);
fprintf(fpresult, "b1=%g,b2=%g\tb0=%g,a0=%g\n\nradius is %g\n\ncontact angle
is %g\n\n", b1, b2, b0, a0, R_fin, angle);
fprintf(fpresult,
"IN=%d,OUT=%d\t p_in=%g,p_out=%g\n\ndelta_p=%g\n\nR_fin=%g\n\nst=%g\n\n", size_liq, size_vg,
p_in, p_out, delta_p, R_fin, st);

fclose(fpresult);
}

int main()
{
    gravity = 0.0;
    Tb = Ts;

    int m = 0, i, N = 0, Z1 = 0, Z2 = 0, Z3 = 0, Z4 = 0, Z5 = 0, Z6 = 0, CHECK = 100;
    double error = 1.0;

    if (_mkdir("./result") == 0)
    {
        printf("Directory './result' was successfully created\n\n");
    }
    else
    {
        printf("Problem creating directory './result'\n");

        DWORD errorMessageID = ::GetLastError();
        if (errorMessageID == EEXIST)
        {
            ;
            {
                printf("Directory './result' already exist - ALERT REWRITING\n\n");
            }
        }
    }

    FILE *fpinfo;
    char name[50];
    for (i = 0; i < 50; i++)
        name[i] = '\0';
    sprintf(name, "./result/info.txt");
    fpinfo = fopen(name, "w+");
    if (fpinfo == NULL)
    {
        printf("file info open error .info\n\n");
        system("pause");
    }
}

```

```

        exit(1);
    }

    fprintf(fpinfo, "LX=%d,LY=%d,R=%g\n\nCentre: X0=%d,Y0=%d\n\n", LX, LY, R, X0, Y0);
    fprintf(fpinfo, "G00=%g\n\nG11=%g\n\nG01=%g\n\nGW0=%g\n\nGR=%g\n\n", G00, G11, G01,
    GW0, GR);
    fprintf(fpinfo, "ERR=%e\tIT=%d\n\n", ERR, IT);
    fclose(fpinfo);

    ini_geo();
    initial();
    write(0);
    printf("Start calculation, wait...\n");

    while ((error > ERR) && (m < IT))
    {
        evolve();
        m++;

        if (m % CHECK == 0)
        {
            error = err(ptotal);
            printf("Step=%d,\t Error=%e\n", m, error);
            contact_angle(m, error, N);
            write(m);

            if (m > 499 && Z1 == 0)
            {
                printf("Stablizing\n");
                Z1 = 1;
                CHECK = 5000;
            }

            if (m > 9999 && Z2 == 0)
            {
                printf("Add gravity%f\n", GR);
                // system("pause");
                gravity = GR;
                Z2 = 1;
                CHECK = 10000;
            }

            if (m > 24999 && Z3 == 0)
            {
                printf("Start heating\n");
                // system("pause");
                Tb = Ts + dT;
                Z3 = 1;
                CHECK = 10000;
            }
        }
    }

    printf("error=%e\tIT=%d\n", error, m);

    // write(1);

    system("pause");
}

```